공학박사학위논문

# Study on FC-CVD-Synthesized CNT Assemblies for Energy Storage and Conversion

## 부유촉매 화학기상증착 공정 기반 탄소나노튜브 집합체의 에너지 저장 및 변환 소재로의 응용에 관한 연구

2023 년 8 월

서울대학교 대학원
재료공학부
전 종 한

# 부유촉매 화학기상증착 공정 기반 탄소나노튜브 집합체의 에너지 저장 및 변환 소재로의 응용에 관한 연구

# STUDY ON FC-CVD-SYNTHESIZED CNT ASSEMBLIES FOR ENERGY STORAGE AND CONVERSION

지도교수: 최 인 석

이 논문을 공학박사 학위논문으로 제출함

2023 년 8 월

서울대학교 대학원
재료공학부
전 종 한

전 종 한의 박사학위 논문을 인준함

2023 년 8 월

| | | |
|---|---|---|
| 위 원 장 | 강 기 석 | (인) |
| 부위원장 | 최 인 석 | (인) |
| 위 원 | 박 종 래 | (인) |
| 위 원 | 정 영 진 | (인) |
| 위 원 | 이 지 훈 | (인) |

# ABSTRACT

## Study on FC-CVD-Synthesized CNT Assemblies for Energy Storage and Conversion

Jong Han Jun

Department of Materials Science and Engineering
The Graduate School
Seoul National University

This thesis systematically explores the potential of carbon nanotube (CNT) assemblies synthesized by floating catalytic chemical vapor deposition (FC-CVD) to demonstrate their viability as an alternative for energy storage and conversion. With this objective, a methodology for implementing FC-CVD-synthesized CNT assemblies in battery, supercapacitor, and water electrolysis applications is proposed through a comprehensive approach in terms of materials, structures, and processes.

First, the potential of FC-CVD-synthesized CNT assemblies to replace traditional current collectors in energy storage applications, including batteries and supercapacitors, is investigated. The assemblies inherently offer corrosion resistance, mechanical robustness, and a reduction in volume and weight, contributing to

addressing the limitations of metallic current collectors, including their vulnerability to oxidation, degradation of mechanical performance with repeated charge/discharge, and reduced specific energy/power due to high density. In addition, the hierarchical structure and porosity of assemblies maximize the electrode-material interface, contributing to improved durability. This represents a significant advancement in the performance-related aspects of energy storage systems and a new prospect for improving energy efficiency.

Second, the hierarchical porous structure of FC-CVD-synthesized CNT assemblies is utilized to design a material-substrate integrated electrode. This is effectively applied in the hydrogen evolution reaction (HER), where robust anchoring of the catalyst is essential for improved catalytic performance and long-term durability. In particular, the rich porosity of CNT assemblies facilitates high loading of non-precious metal HER catalysts, thereby enhancing their inherently low catalytic activity. The simultaneous improvement of the activity and durability of non-precious metal-based catalysts by the integrated structure of the catalyst and CNT assemblies can also be realized in commercial-scale cells, providing the basis for efficient and sustainable green hydrogen production.

Finally, the study focuses on the synthesis of CNT assemblies with different surface defect distributions by controlling FC-CVD process variables in order to understand the triggers of carbon oxidation reaction (COR). This understanding is essential for a comprehensive analysis of the correlation between defects and COR in CNT assemblies, particularly for their use as highly durable carbon-based substrates for oxygen evolution reaction (OER) catalysts. FC-CVD process facilitates the creation of CNTs with different defect types and distributions by tuning the variables. This investigation highlights a definitive relationship between specific defects in the CNTs and the onset of COR and demonstrates the possibility of producing highly durable OER catalyst supports by minimizing these specific

defects. The ability to manipulate these defects can significantly enhance the durability of carbon-based catalyst supports, heralding a major advancement in carbon-based electrochemical systems.

In summary, this thesis demonstrates the ability of FC-CVD-synthesized CNT assemblies to effectively address the traditional material, structural, and process challenges in energy storage and conversion applications. Importantly, these results contribute significantly to the design and optimization of next-generation electrochemical devices by providing a blueprint for overcoming the limitations of current materials and processes. In addition, this thesis provides valuable insights with potential positive impacts in scientific, engineering, societal, and environmental contexts, driving progress in various fields.

---

**Keywords:** Floating catalyst chemical vapor deposition, Carbon nanotube, Energy storage, Battery, Electrochemical capacitor, Energy conversion, Water electrolysis, Hydrogen evolution reaction, Oxygen evolution reaction, Carbon oxidation reaction

***Student Number*:** 2018-35781

# Table of Contents

# List of Tables

# List of Figures

# CHAPTER 1
# Introduction

This chapter presents general information on carbon nanotubes (CNTs) for electrochemical energy storage and conversion applications relevant to the scope of this thesis. The first part of this chapter provides the background of the study, outlining the fundamental rationale and the importance of using CNTs in electrochemical energy storage and conversion applications. This section addresses the unique properties of CNTs that make them promising candidates for these applications and the challenges that limit their effectiveness. The second part offers an overview of CNT synthesis methods. Various techniques used to synthesize CNTs are explored, focusing on their ability to control the structure and properties of the resulting CNTs. The third part of the chapter thoroughly discusses the floating

catalyst chemical vapor deposition (FC-CVD) process, elucidating its distinctive features and adjustable parameters that influence the resulting CNT structures. The efficiency of this process in synthesizing CNT assemblies suitable for electrochemical applications is emphasized. The fourth part discusses the roles of FC-CVD-synthesized CNTs in electrochemical applications. This part covers the utilization of CNTs in various electrochemical energy storage and conversion applications, such as batteries, supercapacitors, and water electrolysis. The performance advantages of FC-CVD-synthesized CNTs in these applications will be highlighted. Finally, the last part of the chapter outlines the specific objectives of the thesis, highlighting the expected contributions to the field of electrochemical energy storage and conversion applications using CNTs. The planned methodology and expected results of the investigation are also outlined.

## 1.1. Study Background

In the field of energy storage and conversion, current collectors are fundamental components that significantly affect the overall performance and efficiency of devices. Often referred to as the backbone of the electrode, their primary role is to facilitate the efficient transport of electrons between the active materials, where the main electrochemical reactions take place, and the external circuit.[1, 2] The electron transport is a key process in devices such as batteries, fuel cells, and supercapacitors, and directly affects their efficiency and operating performance. Traditional materials, including copper, aluminum, and nickel foil/foam, have been favored for current collectors because of their high electrical conductivity, which allows for effective electron transport, as well as their availability and ease of processing.

However, these conventional metal collectors have significant limitations, most notably their susceptibility to corrosion under various operating conditions. Their corrosion or oxidation process leads to a decrease in electrical conductivity and degradation of device performance over time.[3-5] In addition, the relatively high weight and volume of metals negatively impact the energy density of the device, posing a significant challenge for applications that require lightweight and compact energy storage solutions. The rigidity and inflexibility of metallic current collectors are also incompatible with the emerging field of flexible and wearable energy storage devices. Furthermore, there is an inherent mismatch between the mechanical properties of these metal current collectors and the electrochemically active materials, which often leads to interfacial delamination during repeated charge-discharge cycles.[6] To mitigate these problems, a number of research have sought to identify alternative materials for current collectors that can provide high electronic conductivity while offering advantages such as corrosion resistance, mechanical flexibility, and light weight. While various strategies such as surface modifications,

protective coatings, and alternative materials have been explored to overcome these limitations, they often introduce new challenges, such as additional processing steps that increase overall production costs. [7-10]

Given the limitations of metallic current collectors and the drawbacks of previous solutions, carbon-based materials have attracted increased interest due to their potential advantages. Carbon materials offer not only high electrical conductivity comparable to metals, but also excellent corrosion resistance, superior mechanical flexibility, and much lower weight.[11-14] However, the widespread application of carbon-based current collectors has been hindered by several challenges. Certain carbon materials, such as activated carbon or carbon aerogels, have low volumetric electrical conductivity due to their high porosity, which can impede efficient electron transport and thus reduce the overall efficiency of an energy storage or conversion device.[15] In addition, the process of manufacturing carbon-based current collectors on a commercial scale is complex and costly due to the technical challenges of producing homogeneous, defect-free materials, the difficulty of integrating these materials into existing manufacturing processes, and their potential degradation under certain conditions.[16]

Carbon nanotubes (CNTs), along with other carbon nanostructures such as graphene, graphite, and fullerenes, possess intrinsic properties that are conducive to various electrochemical applications, including high electrical conductivity, porous structure, and cost-effectiveness. The properties of the allotropes depend on the bonding nature of the carbon atoms within the structure. For instance, a diamond with $sp^3$ hybridized carbon atoms has excellent mechanical properties and thermal conductivity,[17, 18] while graphite with $sp^2$ hybridized carbon atoms and delocalized $\pi$ electrons provides high electrical conductivity.[19, 20] CNTs, graphene, and fullerenes, which are closely related to graphite, exhibit unique physical and chemical properties.

Compared to traditional carbon materials, CNTs offer numerous advantages for electrochemical applications.[21, 22] First, the large surface area of CNTs increases the available reaction sites, which improves the capacitance and energy storage in supercapacitors.[23, 24] Second, the high electrical conductivity of CNTs ensures efficient charge transfer and improved performance in batteries, supercapacitors, and water electrolysis.[25-28] Third, the chemical stability and non-reactivity of CNTs with common electrolytes enhances their suitability for electrochemical applications, potentially leading to longer device lifetime and improved performances.[29] Finally, the remarkable mechanical strength of CNTs maintains the structural integrity of electrochemical devices over time, making them ideal for applications such as battery electrode CNTs.[30]

In summary, the unique structure and properties of CNTs open up a wealth of opportunities in the design and optimization of various devices, such as batteries, supercapacitors, and water electrolysis systems. By exploiting these properties, it is possible to create more efficient, durable, and powerful energy storage and conversion systems, representing a significant advancement in the field of sustainable energy solutions.

## 1.2. Overview of Synthesis Methods for CNTs

Various techniques exist for the production of CNTs, the most common being arc-discharge,[31, 32] laser ablation,[33, 34] and chemical vapor deposition (CVD).[35] These methods produce CNTs with different properties, such as quality, purity, and size distribution.

i) **Arc-discharge:** This method involves placing two graphite electrodes in a vacuum chamber and creating an electrical discharge between them. The high temperature and pressure generated by the discharge cause the graphite to vaporize and condense into nanotubes on the cooler electrode. The resulting CNTs are usually a mixture of different sizes and structures.

ii) **Laser ablation:** This method uses a pulsed laser to vaporize a graphite target in an inert atmosphere such as helium, hydrogen or nitrogen. The vaporized carbon atoms produced by the laser ablation then condense into CNTs. However, due to the high cost of the laser and limited control over the size and quality of the CNTs, this method is less commonly used for large-scale synthesis.

iii) **Chemical vapor deposition (CVD):** One of the most used methods for the synthesis of CNTs. It involves the use of a metal catalyst, typically iron, nickel, or cobalt, that is deposited on a substrate such as silicon, quartz, or sapphire. The substrate is then placed inside a reaction chamber and heated to a high temperature, typically between 800-1500°C. A hydrocarbon gas, such as methane, ethylene, or acetylene, is introduced into the chamber, and the metal catalyst acts as a catalyst to break down the hydrocarbon molecules. The released carbon atoms self-assemble into nanotubes on the surface of

the substrate.

Arc-discharge and laser ablation methods, some of the earliest techniques for CNT synthesis, have certain limitations when applied to electrochemical fields such as batteries, supercapacitors, and water electrolysis. A primary concern is the high potential for defects and impurities in the CNTs resulting from these techniques. These defects and impurities can reduce electrical conductivity and capacitance, negatively affecting the overall performance of the device.[21] In addition, these traditional methods often fail to consistently control the structural properties of the CNTs, resulting in variable lengths, diameters, and structural properties. This inconsistent production complicates the process of tailoring CNT properties for specific electrochemical applications.[36] In addition, the cost, energy requirements, and technical complexity of these traditional methods limit their scalability, hindering the mass production of high-quality CNTs for electrochemical applications. In contrast, the CVD method addresses some of these challenges by offering better control over CNT properties, improved purity, and enhanced scalability.[37] CNTs synthesized using CVD typically have uniform and well-defined structures, making them less susceptible to defects and impurities. The purity of these CNTs can be further improved by using pure precursor gases, resulting in higher quality CNTs with improved electrochemical properties. The scalability of the CVD process also favors commercial-scale production of high-quality CNTs, potentially reducing costs and broadening the availability of CNTs for electrochemical applications.

Despite these advantages, several challenges remain in incorporating CVD-synthesized CNTs into electrochemical energy storage and conversion systems. Although the CVD process can produce individual CNTs with high precision, fabricating sheet-like assemblies or films of CNTs for use in devices such as batteries or capacitors often requires additional manufacturing steps. These steps can

introduce variability in the structure and quality of the synthesized CNTs, potentially leading to defects.[38] Other issues include the potential toxicity of residual metal catalysts, a potential reduction in mechanical strength due to damage or defects during synthesis or assembly, and the need for more efficient integration methods with other materials. These challenges must be addressed to fully realize the potential of CVD-synthesized CNTs for electrochemical energy storage and conversion applications. **Table 1.1** summarizes the advantages and disadvantages of CNTs synthesized by different methods.

**Table 1.1.** Synthesis methods for CNTs

| | Arc-Discharge | Laser Ablation | Chemical Vapor Deposition (CVD) |
|---|---|---|---|
| **Methods** | 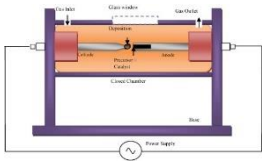 | 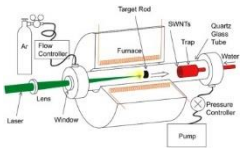 | 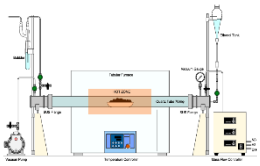 |
| **Condition** | Ar or Ni gas at 500 Torr | High temperatures (500-1000˚C) at high energy laser beam | Low pressure inert gas (Ar) |
| **Yield (%)** | 30 - 90 | - 70 | 20 - 100 |
| **Purity** | Medium | Low | Medium - High |
| **Advantage** | · Inexpensive<br>· Simple protocol | · Produces uniform CNTs<br>· Few structural defects<br>· High purity | · Scalable production of CNTs<br>· Produces long CNTs<br>· High purity<br>· Controllable diameter |
| **Disadvantage** | · Short CNTs<br>· Heterogenous reaction product requires purification<br>· Difficult to scale up | · Expensive<br>· Method limited to lab-scale<br>· Difficult to scale up | · Method limited to lab-scale<br>· Difficult to scale up |

## 1.3. The FC-CVD Method for Synthesizing CNT Assemblies

Considering these factors, the floating catalyst chemical vapor deposition (FC-CVD) method has emerged as a robust approach for synthesizing CNTs.[39] The process involves catalyst formation, high-temperature chemical decomposition of the feedstock, and CNT growth, culminating in the formation of an aerogel-like structure known as a "sock". Under certain conditions, CNT self-assembles in the reactor into this sock, which can be densified by stretching and condensation to form CNT assemblies. The sock plays a critical role in connecting nanoscale CNTs to macroscale products, allowing micromanipulation of a nanoscale entity. The FC-CVD synthesis mechanism involves the following five steps:[40, 41]

- **Catalyst formation:** A transition metal catalyst is heated to a high temperature in an inert gas, such as hydrogen, to form catalyst nanoparticles. These nanoparticles (typically 2-10 nm in size) serve as nucleation sites for CNT growth.

- **Carbon source activation:** A carbon source, such as acetone, ethanol, ethylene glycol, acetylene, or ethylene, is introduced into the reactor and activated by a thermal process. This step generates reactive carbon species that can attach to the catalyst nanoparticles.

- **Carbon species adsorption and diffusion:** The reactive carbon species attach to the surface of catalyst nanoparticles and diffuse into the bulk of the catalyst particles. The carbon species react with the catalyst to form a carbide phase, which is the precursor for CNT growth.

- **CNT nucleation and growth:** Carbon species diffuse through the carbide

phase and saturate the surface of the catalyst nanoparticles. This results in the formation of a CNT nucleus that grows in length and diameter as more carbon species are incorporated into the structure. The CNT grows vertically, perpendicular to the substrate surface.

- **CNT assembly formation:** As the CNTs grow, they can interact with other CNTs to form CNT assemblies. The interactions between the CNTs can be manipulated by adjusting growth conditions, such as the catalyst size and spacing, growth temperature, and carbon source concentration.

The FC-CVD method has similarities to conventional CVD, but there are distinct differences. First, FC-CVD utilizes a unique catalyst delivery system where the catalyst is introduced as a liquid precursor directly into the reaction chamber, unlike conventional CVD where the catalyst is typically pre-deposited on the substrate. This approach allows for more efficient and controlled catalyst deposition, potentially resulting in higher quality CNTs. Second, FC-CVD operates at lower temperatures than conventional CVD, minimizing the formation of amorphous carbon and other impurities that can degrade CNT quality. In addition, the lower temperatures allow for more controlled CNT growth, leading to better alignment and uniformity. The unique attributes of the FC-CVD method offer several advantages over other synthesis methods:

- **Scalability:** FC-CVD can be effectively scaled to produce large quantities of CNTs, making it a viable choice for commercial production.

- **High purity:** CNTs produced by FC-CVD are generally of high purity, with low levels of impurities such as amorphous carbon or metal catalyst residues.

- **Control over CNT diameter and length:** Parameters such as reactor temperature, gas flow rate, and catalyst concentration can be manipulated to precisely control the diameter and length of the CNTs.

- **Customizable properties:** The properties of the CNTs, including electrical conductivity, mechanical strength, and thermal conductivity, can be tailored to specific applications by adjusting the synthesis parameters.

- **Cost-effective:** The FC-CVD method is relatively inexpensive compared to other CNT synthesis methods, such as laser ablation or arc discharge.

Considering these advantages, FC-CVD synthesis could be considered as a promising alternative to conventional CVD methods for preparing CNTs for electrochemical applications. Nevertheless, further research is warranted to optimize the synthesis conditions and to better understand the electrochemical properties of CNTs prepared by FC-CVD.

## 1.4. The Roles of FC-CVD Synthesized CNTs in Electrochemistry Applications

CNTs, characterized by their unique properties such as high electrical conductivity, large surface area, and remarkable mechanical strength, have gained considerable importance in improving the efficiency and lifetime of various electrochemical devices for energy storage and conversion. These devices range from batteries, supercapacitors to fuel cells, electrochemical sensors, and electrolyzers. The following detail the profound impact of the distinct advantages of FC-CVD synthesized CNTs in improving electrochemical performance.

i) **Scalability:** Scalable production of CNTs enables their widespread integration into energy storage and conversion systems. The high surface area of CNTs provides numerous active sites for redox reactions in energy storage devices such as batteries and supercapacitors. In energy conversion devices such as fuel cells and electrolyzers, these active sites act as catalysts to facilitate reactions. As the production of CNTs is scaled up, the number of active sites increases, resulting in a larger electroactive surface area in energy storage devices. This increases the energy storage capacity of the device, resulting in higher energy and power densities. In energy conversion systems, an increased number of catalytic sites increases the efficiency of the conversion process.

ii) **High purity:** The FC-CVD process yield high purity CNTs, which have several advantages for electrochemical devices. First, enhanced electrical conductivity results from minimizing impurities and structural defects that could interrupt the path of charge carriers in these high-purity CNTs, thereby

ensuring efficient charge transfer and electron transport.[42] Other benefits include the mitigation of unwanted side reactions during charge/discharge cycles in devices such as batteries and supercapacitors. This improves efficient charge storage and release, thereby increasing coulombic efficiency. In addition, these high-purity CNTs contribute to the long-term stability and reliability of electrochemical devices by reducing potential sources of mechanical weakness or chemical degradation.

iii) **Control over the diameter and length of CNTs:** Tailoring the dimensions of CNTs provides several performance-enhancing benefits. Fine-tuning the diameter and length optimizes the surface-to-volume ratio, resulting in increased catalytic efficiency. In addition, tailoring these dimensions can improve electron transport pathways, resulting in faster charge transfer, improved electron transport, and more efficient device operation. Furthermore, controlling the dimensions of CNTs increases their mechanical strength and durability, ensuring operational integrity during device use.

iv) **Customizable properties:** The ability to tailor the physical and chemical properties of CNTs, such as functional groups, doping levels, or surface modifications, facilitates their optimization for specific applications within electrochemical devices, thereby improving their performance. Such tailoring affects reaction pathways, kinetics, and adsorption/desorption energies of intermediates, all of which critically determine the catalytic activity and selectivity of reactions. In addition, tailoring CNT properties can improve charge storage capacity and facilitate efficient mass transport, which is essential in energy storage devices such as batteries and supercapacitors.

v) **Cost-effectiveness:** The FC-CVD process can produce high-quality CNTs at a lower cost, significantly reducing the overall production cost of the device. This affordability supports the wider adoption and application of energy storage and conversion technologies in various fields, thereby promoting further advances in these fields.

In summary, the advantageous properties of FC-CVD synthesized CNTs - scalability, high purity, control over diameter and length, customizable properties, and cost-effectiveness - significantly enhance the performance, efficiency, and longevity of electrochemical devices in energy storage and conversion applications. **Table 1.2** provides a comprehensive summary of these advantages and their respective impact on the performance of electrochemical devices.

**Table 1.2.** The summary of the benefits of FC-CVD-synthesized CNTs for energy storage and conversion

| Key Benefits | Distinguishing Features | Impact on Energy and Conversion Applications |
|---|---|---|
| ***Scalability*** | · Abundant space for higher active material loading | · Improved energy and power densities of battery and supercapacitor<br>· Improved catalytic activity in water electrolysis |
| ***High purity*** | · Improved electrical conductivity<br>· Improved mechanical strength | · Increased coulombic efficiency<br>· Improved long-term stability and reliability |
| ***Control over diameter and length*** | · Optimized surface area<br>· Long CNT length | · Faster charge transfer and electron transport<br>· Enhanced mechanical strength and durability |
| ***Customizable properties*** | · Increased surface area<br>· Optimize pore size distribution<br>· Modifying surface chemistry | · Improved charge storage for battery<br>· Large surface area for ion adsorption of supercapacitor |
| ***Cost-effective*** | · Reduced total cost of mass production | · More affordable and accessible energy storage and conversion technologies |

## 1.5. Thesis Objectives

The main objective of this thesis is to address the limitations and challenges of carbon materials associated with conventional materials, structures, and processes used in energy storage (batteries and supercapacitors) and energy conversion (HER and OER in water electrolysis) applications. The approach of exploiting the distinct material, structural, and process-related advantages of these assemblies aims to improve the performance and efficiency of energy storage and conversion devices. To achieve this goal, this thesis is organized into the three main chapters, each with a specific focus:

- **<u>Chapter 2:</u> Experimental Investigation of the Applicability as an Alternative Current Collector**
  → This chapter aims to evaluate the potential of FC-CVD-synthesized CNT assemblies as an alternative to conventional current collectors in energy storage and conversion applications. The experimental investigation explores their performance and potential advantages over existing materials, laying the groundwork for the development of more efficient and cost-effective electrochemical devices.

- **<u>Chapter 3:</u> Design of Substrate-Integrated Electrodes for Durable Hydrogen Evolution Reaction (HER) and Verification of Industrial Applicability**
  → The focus of this chapter is on the design of substrate-integrated electrodes that incorporate FC-CVD synthesized CNT assemblies to enhance electrochemical performance. By exploring different design strategies and configurations, the goal is to produce electrodes that are not

only viable for industrial applications, but also offer significant performance improvements over existing technologies.

- **<u>Chapter 4:</u> Understanding and Mitigating Carbon Oxidation Reactions (COR) in CNTs during Oxygen Evolution Reaction (OER)**
  → This chapter examines the effect of defects in CNTs on the rate of COR during the OER phase of electrocatalytic water splitting. The goal is to reduce these defects by refining the FC-CVD synthesis process, thereby mitigating COR, improving the durability of carbon-based electrodes, and making progress toward efficient electrocatalytic water splitting.

Addressing these objectives in each chapter illustrates the potential of FC-CVD-synthesized CNT assemblies as a promising solution in the field of energy storage and conversion. These efforts aim to overcome the limitations of conventional materials and processes and set the stage for the development of next-generation electrochemical devices.

# CHAPTER 2

# Exploring the Feasibility of FC-CVD-Synthesized CNT Assemblies as Current Collectors for Energy Storage

This chapter presents an in-depth investigation of the potential of CNT current collectors, particularly those synthesized by the FC-CVD method, to enhance the performance of electrochemical energy storage devices. This study aimed to overcome some inherent limitations of active materials in current storage systems, which include slow lithium-ion ($Li^+$) diffusion kinetics and a limited range of pore distribution. The study was based on the hypothesis that CNT-based current collectors could significantly increase electrochemical performance metrics, such as volumetric energy and power densities, while promoting more stable cycling behavior.

In addition, this study developed a method for constructing large-area, lightweight, flexible composite electrodes by embedding ruthenium nanoparticles (Ru NPs) in freestanding layered CNT nanosheets. The resulting Ru NPs-CNT composite electrodes exhibited high mass loading and superior specific capacitances. Furthermore, these composite electrodes were effectively integrated with hydrogel electrolytes to fabricate deformable quasi-solid-state electrochemical capacitors, demonstrating the potential for applications in wearable devices.

The results highlight the potential of macroscale assemblies of CNTs as a simple yet highly effective alternative to conventional metallic current collectors for enhancing the performance of electrochemical energy storage devices. This study provides valuable scientific insights and practical implications for the development of more efficient and reliable power conversion systems for clean energy applications, and underscores the promising role of CNTs in this field.

## 2.1. Introduction

This study highlights the exceptional performance of FC-CVD-synthesized CNT current collectors specifically tailored for battery and capacitor electrodes. The goal is to overcome the inherent limitations of traditional metal-based current collectors and the challenges associated with the sheet formation of conventional CNTs by utilizing FC-CVD-synthesized CNTs. Traditional metal-based current collectors have disadvantages such as relatively high density, inflexibility, and limited surface area, all of which compromise their suitability for advanced, lightweight, and flexible energy storage systems.[43] They also suffer from poor adhesion to active materials, resulting in a decrease in electrochemical performance due to inefficient electron transport.[44, 45] In addition, the powder form of traditional CNTs used as current collectors is problematic because it impedes uniform dispersion, leading to agglomeration that can cause uneven current distribution and degrade the overall performance of the energy storage device.[46] In contrast, FC-CVD method facilitates the fabrication of freestanding CNT assemblies with minimal agglomeration due to its unique growth mechanism. Its high surface area effectively solves the adhesion problem between the active material and the current collector, and significantly improves the dispersion of the active material due to its layer-by-layer structural properties. This robust adhesion promotes electron transport, thereby improving the overall electrochemical performance.

To empirically demonstrate these advantages, the first part focuses on the potential of CNT-based current collectors as an alternative to the inherent limitations of active materials, such as slow $Li^+$ diffusion kinetics and narrow pore distribution, commonly encountered in battery and capacitor-type active materials. Unique advantages of CNT-based current collectors, including their highly porous structures,

large specific surface areas, and low densities, significantly reduce the overall volume of the electrodes. This allows active materials to be embedded within CNT sheets and shortens ion transport paths through channels in multiple directions. As a results, CNT-based current collectors improve electrochemical performance, particularly in terms of volumetric energy and power densities and cycling stability in complex power conversion systems.

The second part presents a simple for fabricating large-area, lightweight, and flexible composite electrodes based on ruthenium nanoparticle (Ru NP)-embedded layered CNT nanosheets. The high surface area layered CNT nanosheets play multifunctional roles, contributing to capacitive storage through the electric double layer (EDL) mechanism. They act as deformable, durable, and lightweight current collectors and provide an effective platform for additive-free electrodes (without conductive agents and binders). The resulting Ru NP-CNT composite electrodes exhibit high mass loading of Ru NPs (Ru:CNT weight ratio of 5:1) and impressive specific capacitance. Finally, by integrating Ru NP-decorated CNT nanosheets with hydrogel electrolytes, deformable solid-state electrochemical capacitors were fabricated. These satisfy several requirements for power sources used in portable devices, including high energy/power density, robust cyclability, and remarkable electrochemical stability under bending and stretching deformations.

The results of this study represent an important step toward making FC-CVD-synthesized CNTs a promising material for improving energy storage devices and developing current collectors for applications beyond the conventional roles of traditional current collectors.

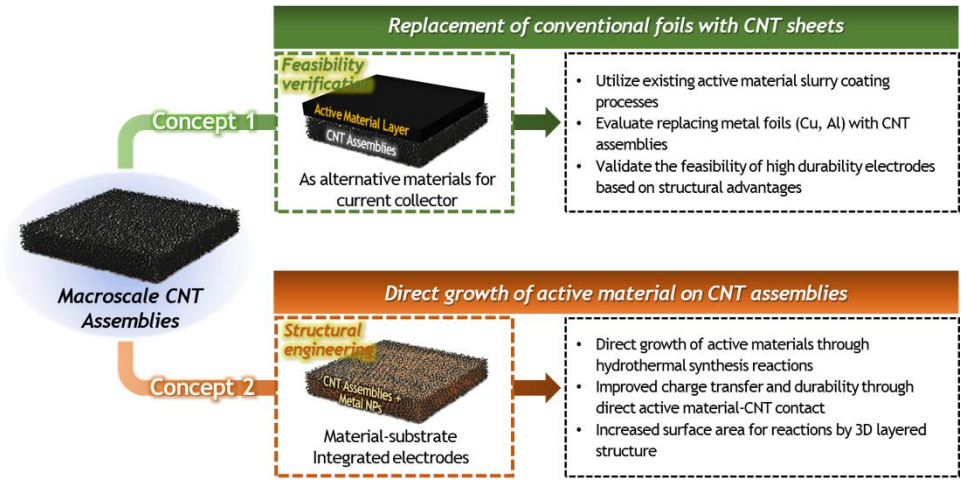


**Figure 2.1.** Conceptualization of two types of electrodes to validate the potential of CNT assemblies as novel current collectors for energy storage: 1) to verify their feasibility as an alternative material to metal collectors, and 2) to evaluate the performance impact of integrated electrodes in a three-dimensional hierarchical structure *via* direct growth of active material.

## 2.2. Experimental Methods

### 2.2.1. Preparation of AC–CNTs and Graphite–CNTs electrodes

The precursor solution of CNTs is prepared by mixing ethylene glycol (>98%, Samchun Chemical, Korea), ferrocene (>98%, Sigma–Aldrich, USA), thiophene (>99%, Sigma–Aldrich, USA), and polysorbate 20 (Sigma–Aldrich, USA) in weight fractions of 98.0, 0.2, 0.8, and 1.0 wt.%, respectively; then, the solution is inserted into a furnace heated to 1450 °C under 1800 sccm hydrogen gas flow. The capacitor-type electrode (activated carbon–CNTs (AC–CNTs)) and battery-type electrode (Graphite–CNTs) are prepared by mixing active materials (graphite and activated carbon purchased from MTI, USA) with carbon black (MTI, USA) and polyvinylidene fluoride (PVDF) (> 99.5%, MTI, USA) with a weight ratio of 8:1:1 in 1-methyl-2-pyrrolidone (NMP) (99.5%, Sigma–Aldrich, USA) as a solvent to form slurries. The resulting anode and cathode slurries are coated on the surface of synthesized CNT sheets, and the fabricated sheets are vacuum dried at 120 °C for 12 h. To compare the properties of these electrodes, conventional electrodes (AC-coated Al foil and graphite-coated Cu foil, both foils purchased from Welcos, Korea) are prepared. The compositions and the coating processes of the slurries are the same as above.

### 2.2.2. Preparation of Ru nanoparticles embedded in CNTs electrodes

Ru@a-CNTs were fabricated by the following procedures. The prepared freestanding CNT sheets were acid-treated by the mixture of $H_2SO_4$ (95.0%, Alfa-Aesar, USA) and $HNO_3$ (70.0%, Alfa-Aesar, USA) (v/v=3:1) at 60 °C for 2 h. The

solution to decorate Ru NPs on the acid-treated CNT sheets was prepared by dispersing ruthenium(III) chloride hydrate ($RuCl_3 \cdot xH_2O$) (Sigma-Aldrich, USA) as a Ru precursor, SDS ($C_{12}H_{25}NaO_4S$) (Sigma-Aldrich, USA) as an anionic surfactant, and TSC ($C_6H_5Na_3O_7$) (Alfa-Aesar, USA) as a stabilizing agent in distilled water. The acid-treated CNT sheets were dipped in the Ru precursor solution while the solution was kept stirring for 24 h. Then, 0.5 M $NaBH_4$ (99.0%, Thermo Fisher Scientific, USA) solution was added to the solution for reduction to metallic Ru while the mixture was kept stirring for another 3 h. Finally, Ru@a-CNTs were obtained after freeze-drying for 24 h to eliminate the residual moisture and subsequent annealing at 250 °C for 3 h to improve the crystallinity of Ru NPs.

### 2.2.3. Material characterization

To compare the mechanical, electrical, and microstructural properties of CNT sheets with those of commercially available carbon-based substrates, carbon cloth (W1S1009, CeTech, Taiwan) and carbon paper (MGL190, AvCarb Material Solutions, USA) are prepared. The uniaxial tensile test is conducted according to the ASTM D3039 (CNT sheets and carbon-based substrates) and ASTM E345 (metallic foils) standards by using a universal mechanical testing machine (Instron 5942, Instron, USA). The electrical conductivity of current collector materials is measured by 4-point probe equipment (Model-2400, Keithley, USA). Specific Brunauer–Emmett–Teller (BET) surface areas and density functional theory pore size distributions are determined by nitrogen adsorption and desorption isotherms measured at 77 K (Autosorb® iQ-MP, Quantachrome Instruments, USA). The specific surface areas and pore volumes of the samples are calculated based on the

nitrogen adsorption and desorption isotherm results. The surface and cross-sectional morphologies of the fabricated CNT sheets-based electrodes are characterized by field emission-scanning electron microscopy (FE–SEM; MERLIN Compact, ZEISS, Germany) at an acceleration voltage of 2 kV. The elemental composition of nanocomposites was measured by EDS (Thermo Fisher Scientific, USA) coupled with FE-SEM. The cross-sectional morphologies of all CNT-based electrodes were analyzed after milling using a focused ion beam (FIB, Helios 650, FEI, USA). The specific surface area, total pore area, and pore size distribution of p-CNTs and a-CNTs were measured by BET (Micromeritics ASAP 2020, USA) analysis of the nitrogen adsorption isotherms at 77 K. The XPS analysis was performed on sputter-cleaned surfaces using a K-Alpha+ instrument (Thermo Fisher Scientific, USA) equipped with a monochromatic Al Kα X-ray source (1486.6 eV). The XRD analysis was performed on a D8 Advance (Bruker, USA) with a Cu Kα radiation wavelength of 1.542 Å. The surface wettability of nanocomposites was measured using the contact angle analyzer (Phoenix 300 Touch, Surface Electro Optics, Korea).

### 2.2.4. Electrochemical measurements

AC–CNTs and Graphite–CNTs are assembled in coin-type (CR 2032) half-cells with lithium metal and polypropylene film (Celgard® 2325) as the counter electrode and separator, respectively. The electrolyte is 1 M lithium hexafluorophosphate ($LiPF_6$) dissolved in a mixture of ethylene carbonate/diethyl carbonate (EC/DEC) (1:1 v/v, Welcos, Korea). The electrochemical performances of Ru@a-CNTs were evaluated using a three-electrode system with 0.5 M $H_2SO_4$ aqueous electrolyte solution (95.0%, Alfa-Aesar, USA). The three-electrode cell consisted of a working

electrode (prepared electrodes in this work), reference electrode (Ag/AgCl), and counter electrode (platinum foil). The CV measurements were carried out in a potential range of 0-0.8 V (vs. Ag/AgCl) with scan rates ranging from 10 to 1000 mV $s^{-1}$ The cyclability of electrodes was determined by the CV measurements at a scan rate of 10 mV $s^{-1}$ for 2000 cycles. The EIS measurements were recorded in the frequency range of 100 kHz-0.01 Hz by using an AC voltage of 10 mV. The electrochemical performance of symmetric full-cell capacitors was examined by the GCD technique. GCD measurements were carried out at the current densities from 0.5 to10.0 A $g^{-1}$ in a voltage range between 0 and 1 V. All these electrochemical measurements were performed using a potentiostat (SP-300, BioLogic Science Instruments, France) and a multichannel battery cycler (Q3100, McScience, Korea).

## 2.3. Investigation of FC-CVD-Synthesized CNT Assemblies as Current Collector Alternatives

### 2.3.1. Microstructural characterization of CNT sheet-based electrodes

As depicted in **Figure 2.2**, the fabrication processes for AC–CNTs and Graphite–CNTs sheets involve the synthesis of freestanding CNT sheets using FC–CVD in a vertical tube-type furnace, followed by coating with AC or graphite-based slurries. Freestanding CNT sheets for coating AC and graphite are observed to have a random network structure of CNT bundles and a thickness of 5 μm, as shown in **Figure 2.3**.

**Figure 2.4**A-D show the cross-sectional morphologies of the CNT-based electrodes (AC–CNTs and Graphite–CNTs) and conventional electrodes (AC–Al and Graphite–Cu), respectively. Although the CNT sheets and conventional electrodes (**Figure 2.5**) show similar surface morphologies regardless of the current collector, there are significant differences in their cross-sectional microstructures. For AC-based electrodes, the total thickness of AC–CNTs (~65 μm) is about 23% thinner than that of Al foil-based electrode (~85 μm) under the same areal mass loading of 6.0 mg $cm^{-2}$ (**Figure 2.4**A and C). In a similar manner, when graphite of 1.0 mg $cm^{-2}$ was coated, Graphite-CNTs (~13 μm) demonstrate a thickness that is about 57% thinner thickness than that of Cu foil-based electrode (~30 μm) (**Figure 2.4**B and D).

This reduction in thickness is due to the efficient volume structures of CNT-based electrodes, which effectively embed active materials. These CNT-based current collectors maximize both mass loading and weight fraction of active materials due to their high porosity, large surface area, and lightweight.

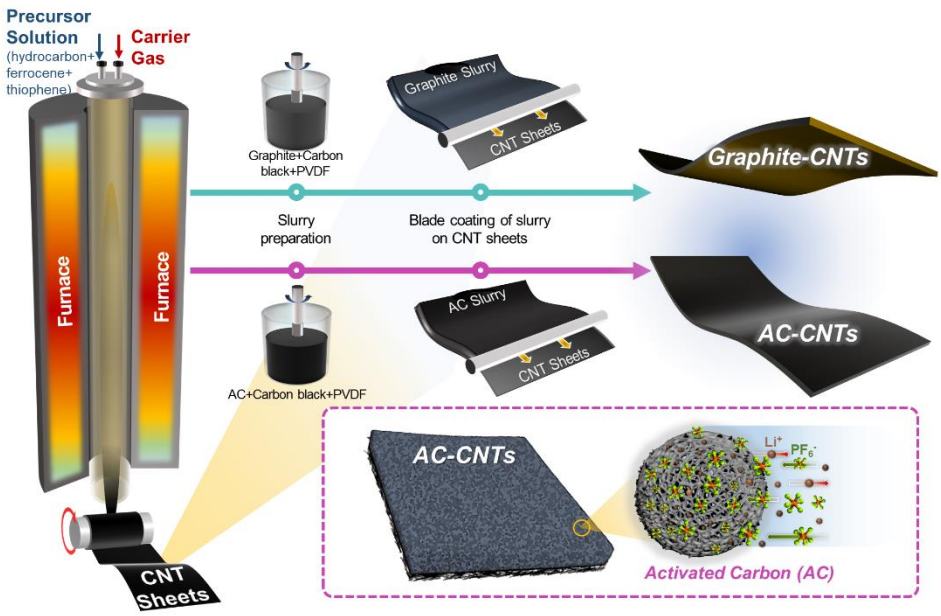


**Figure 2.2.** The fabrication process of CNT sheets-based electrodes (Graphite-CNTs and AC-CNTs).

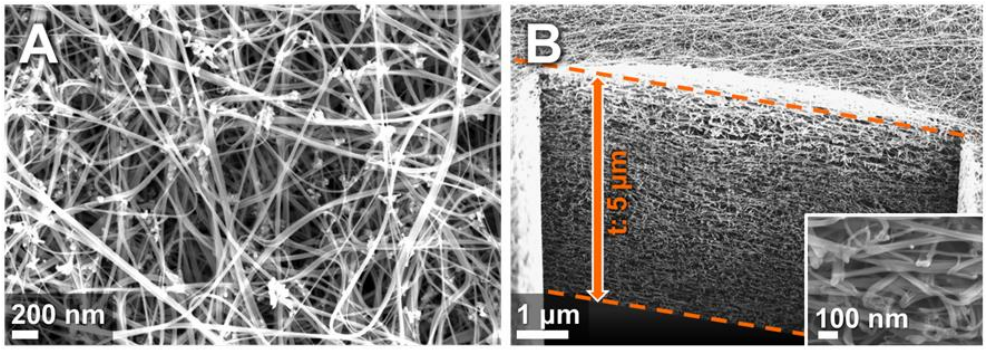


**Figure 2.3.** The FE-SEM images of pristine CNT sheets: (A) surface and (B) cross-sectional morphology.

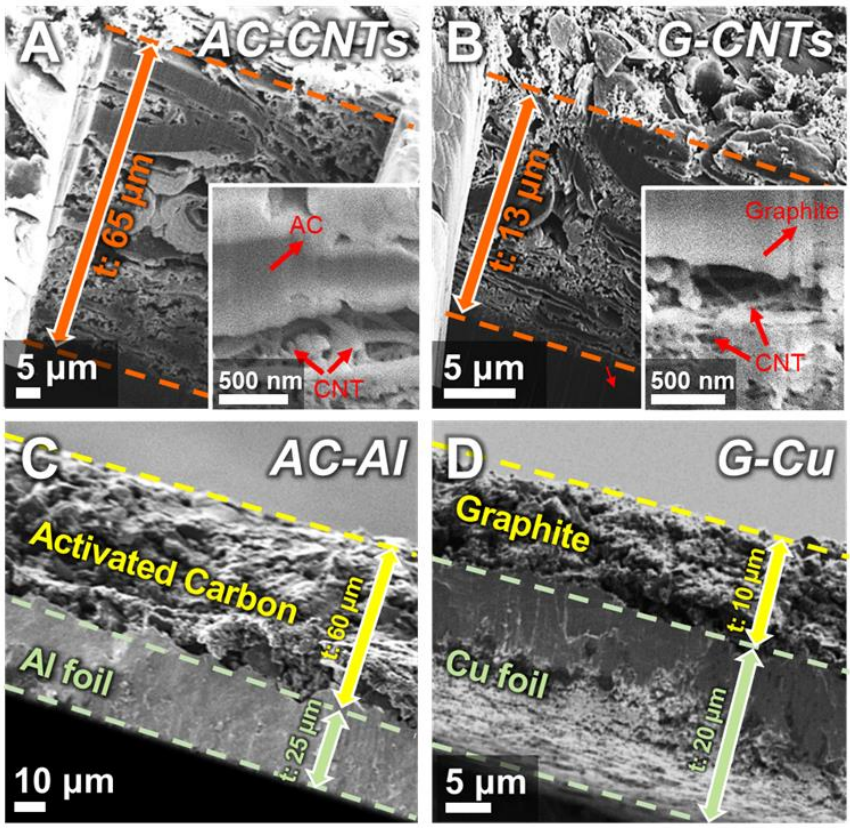


**Figure 2.4.** The cross-sectional FE-SEM images of electrodes: (A) AC-CNTs, (B) Graphite–CNTs, (C) AC–Al, and (D) Graphite-Cu.

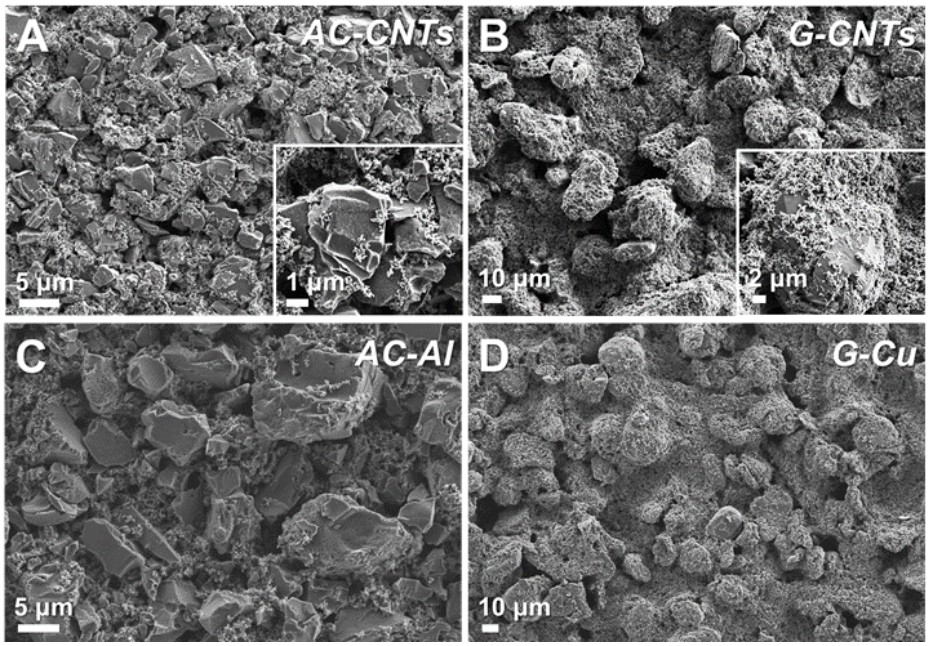


**Figure 2.5.** The surface FE-SEM images of electrodes: (A) AC-CNTs, (B) Graphite-CNTs, (C) AC-Al, and (D) Graphite-Cu.

### 2.3.2. Electrochemical characterization of capacitor-type AC–CNTs

The electrochemical characteristics of AC–CNT-based capacitor-type electrode are evaluated by using a half-cell configuration. **Figure 2.6**A and B depict cyclic voltammograms (CVs) measured at various scan rates and galvanostatic charging and discharging (GCD) profiles, respectively. The rectangular CVs and linearly changing potential profiles indicate that typical ion adsorption and desorption processes occur at the surfaces of AC–CNTs, i.e., electric double-layer (EDL) capacitive behavior.[47] The capacitive contribution from AC-CNTs may be more dominant due to its high surface area and rapid charge/discharge behavior, which can overshadow the slower faradaic reaction in Li metal.[48] The volumetric capacities of AC–CNTs and conventional electrodes as functions of the charging and discharging current densities are presented in **Figure 2.6**C. Remarkably, the areal mass loadings of the ACs in each electrode are identical. These results confirm that both the volumetric capacity and rate capability are significantly improved by adopting CNT-based current collectors. In detail, at the lowest charging and discharging current densities of 200 mA $cm^{-3}$, the delivered capacities of AC–CNTs (77 mAh $cm^{-3}$ and 37 mAh $g^{-1}$) are about 38% higher than that of conventional electrodes (56 mAh $cm^{-3}$ and 26 mAh $g^{-1}$). Furthermore, when the current density reaches its highest value of 5,000 mA $cm^{-3}$, the AC–CNTs still retain 82% of the maximum capacity, whereas the capacity of conventional electrodes drops sharply with the charging and discharging rates, leaving only 44% of the capacity available. By considering the long-term cycling stability shown in **Figure 2.6**D, the AC–CNTs preserve 86% of the initial capacity after 2,000 cycles (decay rate of 0.007% per cycle), showing superior performance relative to that of conventional electrodes (77% of the initial capacity).

The improved rate capability and cycling stability of the AC–CNTs most probably result from their abundant pore volumes (1.2 $cm^3$ $g^{-1}$), hierarchical porous structures composed of microporous AC and meso- and macroporous CNT sheets, as depicted in mixed $N_2$ physisorption isotherm of types I and IV (**Figure 2.7**A and B), and high specific surface areas (1425.5 $m^2$ $g^{-1}$).[49, 50] In addition, the intrinsic surface functional groups of C–O, C=O, and O–C=O– on CNT sheets provide extra adsorption sites for capacitive ion storage (The XPS C 1s spectrum to identify the surface oxygen functional groups of the CNT sheets is shown in **Figure 2.7**C).[51] This structure is highly advantageous for enhancing EDL capacitance and fast mass transport at fast charge and discharge rates relative to conventional electrodes.[52]

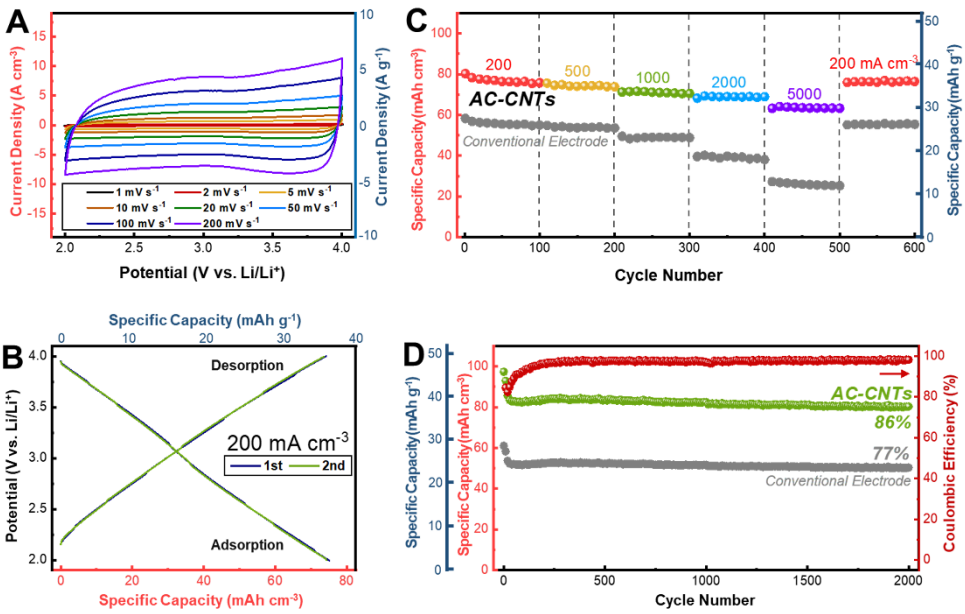


**Figure 2.6.** Electrochemical characterization of AC–CNT half-cells: (A) CV curves at different scan rates of 1, 2, 5, 10, 20, 50, 100, and 200 mV $s^{-1}$ and (B) potential profiles measured at a specific current of 200 mA $cm^{-3}$ for the initial 2 cycles. Comparison of the electrochemical properties with the conventional electrode (the AC electrode coated on Al foil): (C) specific capacities and rate capabilities and (D) long-term cyclabilities for 2000 cycles. The current density and specific capacity are calculated based on the entire volume or weight of each electrode.

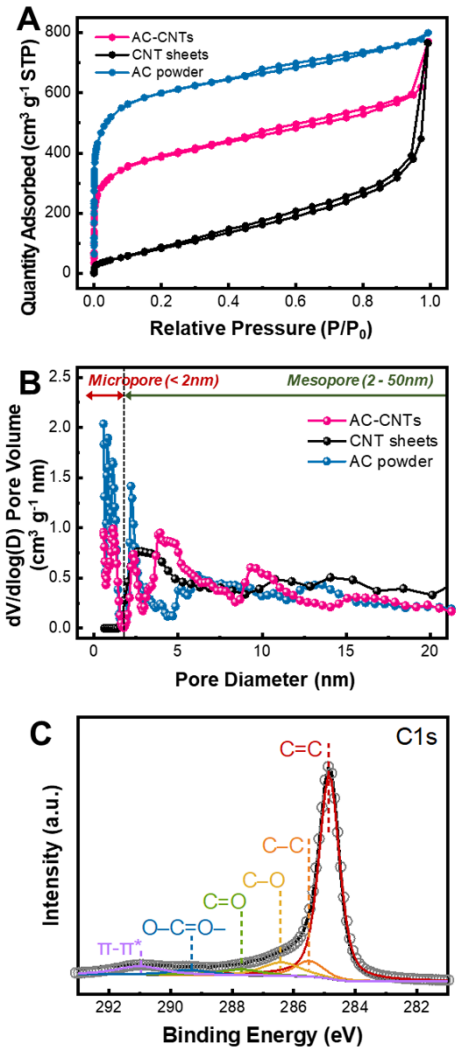


**Figure 2.7.** (A) Nitrogen adsorption-desorption isotherms and (B) distribution of cumulative pore volume as a function of the pore diameter of AC powder, CNT sheets, and AC-CNTs. (C) XPS C 1s sub-peaks fitted spectrum of CNT sheets.

### 2.3.3. Electrochemical characterization of battery-type Graphite–CNTs

**Figure 2.8**A shows CV curves Graphite–CNTs measured within the potential range of 0–2 V (vs. $Li/Li^+$) for the initial 2 cycles. It has been widely reported that an irreversible cathodic peak related to the formation of a solid-state electrolyte interphase (SEI) is observed at a potential less than 0.5 V (vs. $Li/Li^+$).[53, 54] **Figure 2.8**B depicts the potential profiles of Graphite–CNTs for the initial two cycles. Similar to the cases of AC–CNT electrodes, all electrochemical characteristics of volumetric/gravimetric capacity, long-term cycling stability, and rate capability are greatly improved in Graphite–CNT electrodes, as shown in **Figure 2.8**C and D. With respect to the long-term cycling stability, Graphite–CNTs maintain 90% of the initial volumetric capacity (515 mAh $cm^{-3}$ and 330 mAh $g^{-1}$) after 1,000 cycles (decay rate of 0.01% per cycle); however, 21% is diminished for the cases of conventional electrodes. The performance enhancement obtained by adopting CNT current collectors is also observed in the rate capability test, as shown in **Figure 2.8**D. At the fastest charging and discharging rate of 2,000 mA $cm^{-3}$, the discharge capacities of Graphite–CNTs still retain 126 mAh $cm^{-3}$ and 81 mAh $g^{-1}$ (24.5% of maximum capacity); those of conventional electrodes show a negligible capacity of 15 mAh $cm^{-3}$ and 9 mAh $g^{-1}$ (8.9% of maximum capacity).

To identify the mechanisms for improving the power performance by introducing CNT-based current collectors, electrochemical impedance spectroscopy (EIS) measurements are conducted (**Figure 2.9**A). The Li-ion diffusion coefficient (*D*), which directly affects the transport kinetics of $Li^+$ ions, is calculated from the inclined lines in the low-frequency region by using the following equation (2.1):[55-57]

$$D = R^2 T^2 / 2A^2 n^4 F^4 C^2 \sigma^2 \qquad (2.1)$$

where $R$, $T$, $A$, $n$, $F$, $C$, and $\sigma$ are the ideal gas constant, absolute temperature, cumulative electrode area, number of electrons, Faraday constant, $Li^+$ ion concentration, and Warburg factor, respectively. Because all the variables except for $\sigma$ are identical for both CNT-based and conventional electrodes, the diffusivity is solely dependent on the Warburg factor. The value of $\sigma$ is simply estimated from the linear fitting of the $Z'$ vs. $1/\omega^{0.5}$ plot, where $Z'$ and $\omega$ are the real impedance and angular frequency, respectively. As shown in **Figure 2.9**B, the $\sigma$ values of LIG–CNTs are determined to be 21.7 $\Omega$ $cm^{-0.5}$; this value is 8.5 times lower than that of the conventional electrode (183.7 $\Omega$ $cm^{-0.5}$). Therefore, the $D$ value of the Graphite–CNTs is over 2 orders of magnitude larger than that of the conventional electrode.

The enhanced electrochemical performance of CNT current collector-based electrodes is attributed to the following reasons. First, the improved volumetric capacity and rate capability result from i) the reduced total volumes of the electrodes at a given mass loading and ii) the shorter and multidirectional electron pathways along with the 3-dimensional CNT networks whereby electrons supplied to the top surfaces of the conventional electrodes are transported long distances from the planar-shaped current collectors.[58] Second, the large interfacial areas between the active materials and CNT-based current collectors improve cycling stability. In conventional electrodes, only the active materials near the bottoms of electrodes are in direct contact with current collectors, and the degree of electrode integrity in terms of adhesion is dependent solely on the dispersibility of binders in the bulk regions of the electrodes. Thus, conventional electrodes inevitably show weak adhesion and poor mechanical stability.[59] However, each active material particle in CNT-based electrodes might be in direct contact with and surrounded by highly conductive

intertwined CNT networks. As a result, compared to conventional metallic current collectors, the CNT sheets effectively alleviate the detachment of active materials from the current collector caused by repeated cycling, leading to highly stable long-term cycling performance.[60]

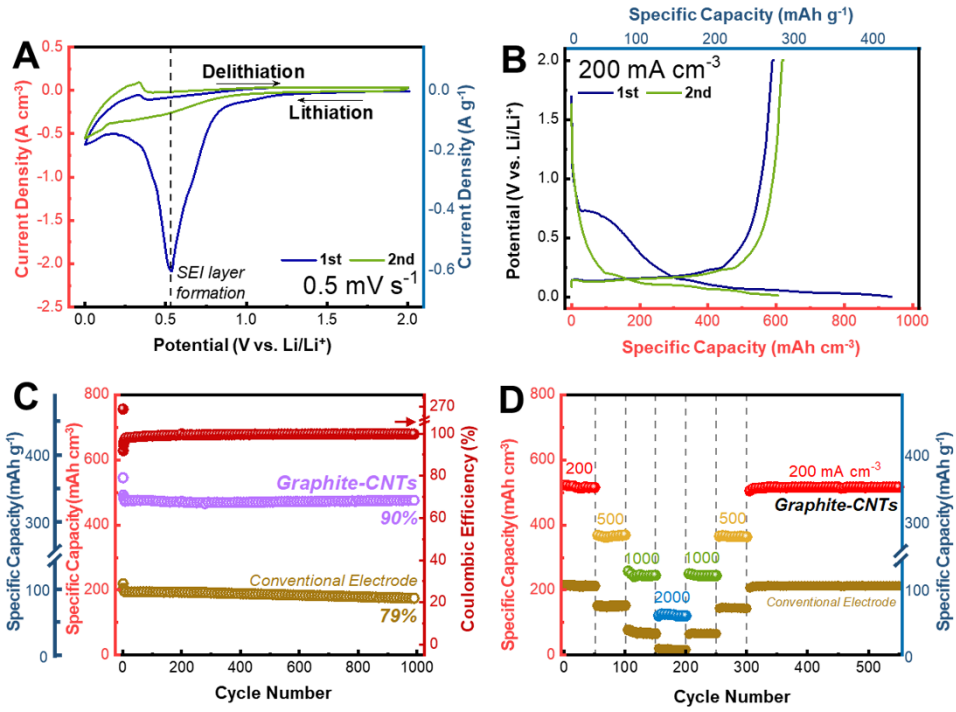


**Figure 2.8.** Electrochemical characterization of Graphite–CNT half-cells: (A) CV curves at a scan rate of 0.5 mV $s^{-1}$ and (B) potential profiles at a current density of 200 mA $cm^{-3}$. Comparison of electrochemical properties with a conventional electrode (the graphite electrode coated on Cu foil): (C) long-term cyclability for 1000 cycles and (D) specific capacities and rate capabilities. The current density and specific capacity are calculated based on the entire volume or weight of each electrode.

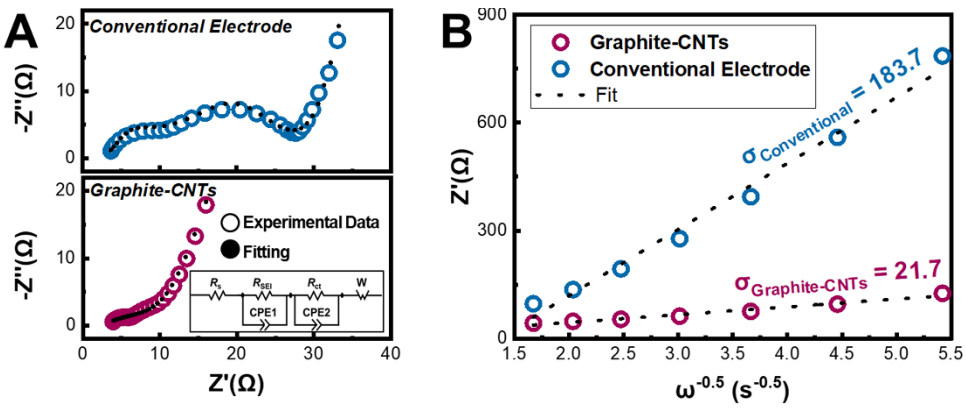


**Figure 2.9.** (A) Nyquist plots of Graphite–CNTs and the conventional electrodes in the frequency range of 100 kHz to 0.01 Hz and (B) Warburg factor ($\sigma$) obtained from the slope between $Z'$ vs. $1/\omega^{0.5}$ in the low-frequency region.

## 2.4. Design of Material-Substrate Integrated Electrodes Using Hierarchical Structures of FC-CVD-Synthesized CNT Assemblies

### 2.4.1. The fabrication process of integrated electrode

The fabrication process of Ru NP-decorated acid-treated CNT sheets (Ru@a-CNTs) is shown in **Figure 2.10**A. CNT sheets were first treated with a mixture of sulfuric acid ($H_2SO4$) and nitric acid ($HNO_3$) to increase their hydrophilicity and reactivity for the subsequent Ru decoration. Ru NPs were then deposited on the CNT surface by immersing the acid-treated CNTs (a-CNTs) in an aqueous solution containing $RuCl_3$, sodium dodecyl sulfate (SDS), and trisodium citrate (TSC), which act as Ru precursor, anionic surfactant, and a stabilizer, respectively. Then, sodium borohydride ($NaBH_4$) was added to this mixture as a reducing agent. During this process, Ru ions are initially adsorbed onto the sulfonic group of the SDS-formed supramolecular self-assembly on the CNTs surface, followed by densification of the deposited Ru NPs. SDS-modified CNTs can uniformly decorate Ru NPs while maintaining the intrinsic physical and electrical properties of CNTs due to the non-covalent functionalization.[61] The resulting Ru@a-CNTs are freestanding and conductive, acting as an integrated electrode structure capable of decorating Ru particles up to five times the weight of the CNT sheets. Detailed optimization information for loading Ru NPs onto CNT sheets is described in sections 2.4.2 and 2.4.3.

**Figure 2.10**B shows photographs to demonstrate the structural advantages of the CNT sheets, including design flexibility, lightweight, high mechanical strength, and versatile scalability (in from the upper left image). The freestanding Ru@a-CNTs-

based nanosheets can be deformed and folded to any kind of form (a flower shape is demonstrated here) while maintaining high electrical conductivity. These nanosheets are exceptionally light, capable of sustaining high mechanical load, and conveniently scalable for large-scale electrode fabrication, thereby supporting their mass production viability.

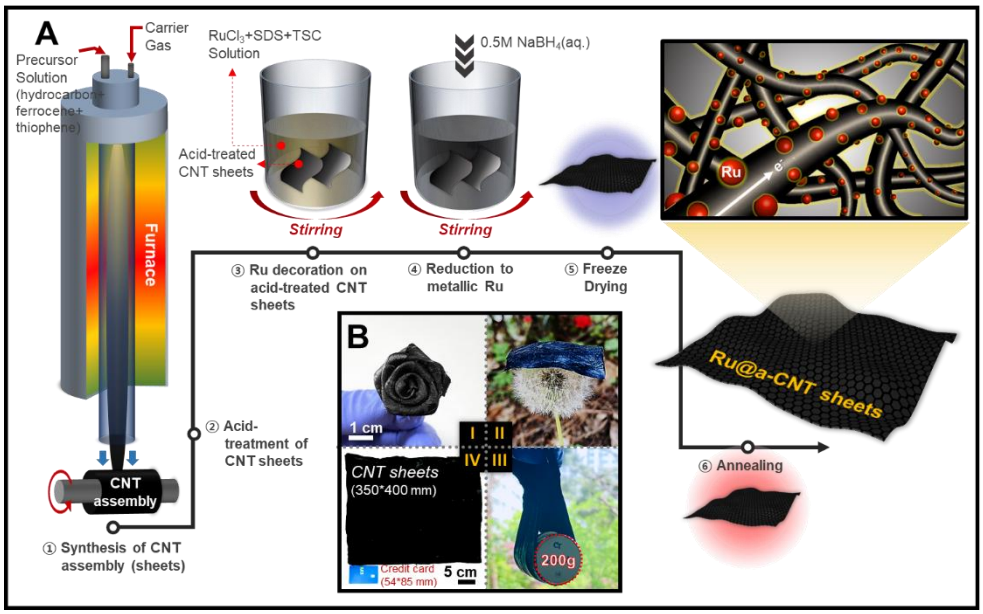


**Figure 2.10.** (A) Schematic of the fabrication procedures of Ru@a-CNTs. CNT sheets were synthesized by using a vertical-type CVD furnace. Ru@a-CNTs were prepared through the following processes: 1) synthesis of CNT sheets, 2) acid-treatment of CNT sheets, 3) Ru decoration on acid-treated CNT sheets, 4) reduction to metallic Ru NPs, 5) freeze-drying, and 6) annealing. (B) Photographs of the CNT sheets showing various properties (clockwise from top left): i) flexibility, ii) lightweight, iii) high mechanical strength, and iv) large scalability.

### 2.4.2. Investigation of the effect of acid-treatment time on CNT sheets

This section focuses on optimizing the duration of acid treatment time for CNT sheets to facilitate the best possible decoration with Ru NPs. The ideal acid treatment duration should create the highest possible number of hydrophilic oxygen-containing groups without compromising the structural integrity of CNTs. XPS analysis (**Figure 2.11**A) shows that the relative proportions of hydrophilic oxygen-containing groups gradually increase with the duration of acid treatment (**Table 2.1**). **Figure 2.11**B shows a significant decrease in the water contact angle with increasing treatment time, suggesting a transition from a hydrophobic to a hydrophilic CNT surface due to the progressive formation of hydrophilic functional groups. The increasing hydrophilicity of the CNT sheets promotes the effective infiltration of the Ru precursor solution. However, at the same time, the CNTs structure collapses with increasing acid treatment time, as observed in the XRD result (**Figure 2.11**C); the (002) peak intensity for graphitic carbon gradually decreases with increasing treatment time. Therefore, an optimal acid treatment time of 2 hours was selected to achieve high wettability with a well-preserved CNT structure.

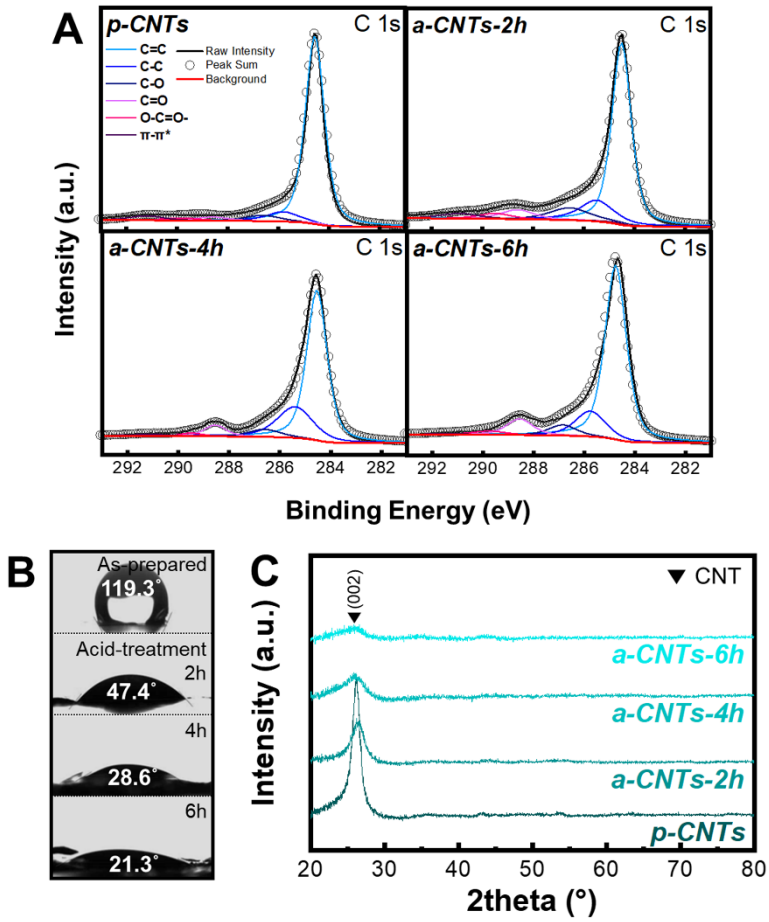


**Figure 2.11.** Investigate the effect of acid treatment duration on CNT structure and surface: (A) XPS C 1s spectra with five deconvoluted subpeaks, (B) the water contact angles, and (C) XRD patterns of CNT sheets treated for different acid-treatment times (2, 4, and 6 h).

**Table 2.1.** Relative percentage of the chemical bonds based on subpeaks extracted from the deconvoluted C 1s core-level spectra of the CNT sheets treated for different acid-treatment times (2, 4, and 6 h).

| Material | Relative percentage [%] | | | | | |
|---|---|---|---|---|---|---|
| | C=C (284.5 eV) | C–C (285.5 eV) | C–O (286.6 eV) | C=O (288.3 eV) | O–C=O– (289.5 eV) | π–π* Transition (291.1 eV) |
| **p-CNTs** | 35.35 | 14.00 | 13.06 | 12.50 | 12.34 | 12.76 |
| **a-CNTs-2 h** | 29.95 | 15.90 | 14.50 | 13.62 | 12.97 | 13.05 |
| **a-CNTs-4 h** | 25.46 | 18.52 | 14.72 | 15.43 | 12.97 | 12.91 |
| **a-CNTs-6 h** | 24.78 | 17.15 | 16.06 | 16.52 | 13.01 | 12.49 |

### 2.4.3. Optimization of Ru NPs loading on Ru@a-CNTs

Ru@a-CNTs loaded with different amounts of Ru NPs were prepared to identify the optimal Ru NPs loading level that exhibits the best electrochemical property. **Figure 2.12**A shows FE-SEM images of Ru@a-CNTs prepared with Ru-CNT ratios of 1:1, 3:1, 5:1, and 7:1. As the Ru-CNTs ratio increased from 1:1 to 5:1, the amount of Ru NPs gradually increased and was uniformly distributed along the CNT structures. However, a clear aggregation of nanoparticles was observed at 7:1 Ru-CNTs ratio, probably due to the oversaturation of Ru ion adsorption on the surface of CNT sheets.

The electrochemical performances were evaluated based on these morphological differences and Ru NPs loading. The CV curves (**Figure 2.12**B) show an area increase with increasing Ru NPs loading. The specific capacitances (**Figure 2.12**C) increase continuously with increasing Ru NPs loading, with the highest specific capacitance of 260 F $g^{-1}$ achieved at a scan rate of 10 mV $s^{-1}$ for a 7:1 Ru-CNTs ratio. However, the rate capabilities of the 7:1 ratio Ru@a-CNTs decrease as the CV scan rate increases from 20 to 1000 mV $s^{-1}$, probably due to the large Ru NPs formation by aggregation at high Ru loading, which may hinder the efficient diffusion of electrolyte ions into the composite electrode. Consequently, it was found that a 5:1 Ru-CNTs ratio could provide the most favorable capacitive performance and rate capabilities among different Ru NPs loading levels.

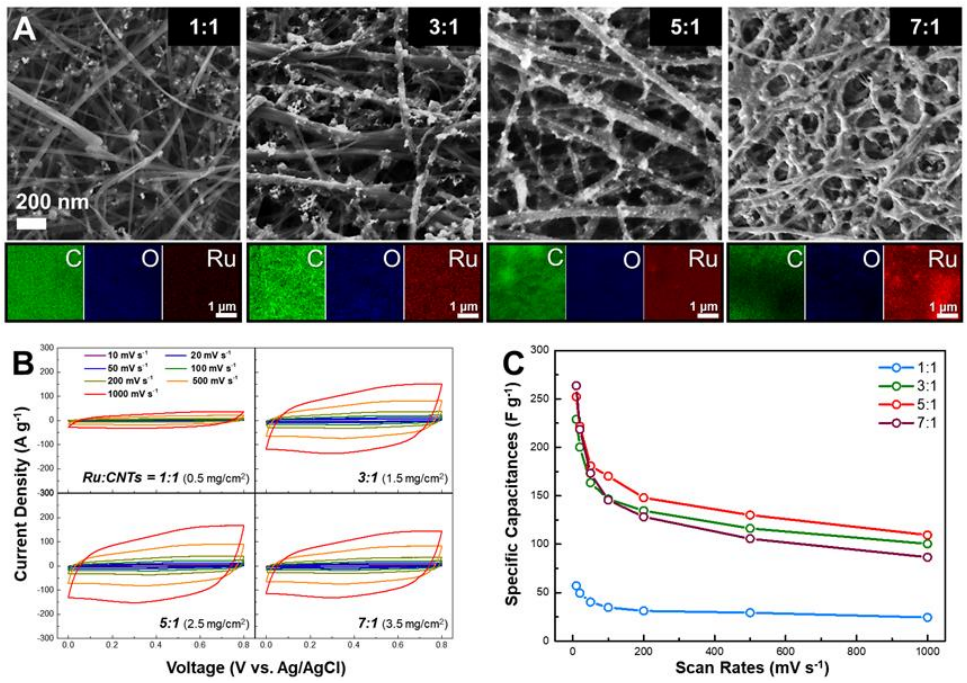


**Figure 2.12.** (A) FE-SEM and EDS mapping images, (B) CV curves as a function of scan rate, and (C) specific capacitances of Ru@a-CNTs with different mass loading (Ru:CNTs=1:1, 3:1, 5:1, and 7:1)

### 2.4.4. Microstructural characterization of Ru@a-CNTs

In the aforementioned sections, the major variables (acid-treatment time of CNTs and Ru NP precursor concentration) to optimize the microstructural features, chemical structure, and electrochemical performance of Ru@a-CNTs were systematically controlled. **Figure 2.13**A–D shows SEM images of pristine CNTs (p-CNTs), a-CNTs, Ru@p-CNTs, and Ru@a-CNTs. The surface morphologies of p-CNTs (**Figure 2.13**A) and a-CNTs (**Figure 2.13**B) show similar structures of assembled CNT bundles, indicating that the densely formed network of CNTs was well maintained after the acid treatment. From the comparison of the FE-SEM images of Ru@p-CNTs (**Figure 2.13**C) and Ru@a-CNTs (**Figure 2.13**D), it was confirmed that the areal coverage and uniformity of Ru NPs on the surface of CNTs increased in the case of acid treatment. In addition, EDS mapping images of the surface (**Figure 2.13**E) and cross-section (**Figure 2.13**F) of Ru@a-CNTs reveal that the Ru NPs are uniformly formed not only on the surface but also in the entire thickness direction (~ 4.2 μm) of the layered CNT sheets. This improved uniformity and surface coverage can be attributed to two factors: i) the large surface area of the CNT sheets, which provides abundant sites for Ru decoration, and ii) the increased hydrophilicity due to the surface modification by acid treatment. The optimized acid treatment time of 2 h significantly affects not only the uniformity and areal coverage of the deposited Ru NPs, but also the aqueous electrolyte wettability, a critical factor for improving the energy and power performance of aqueous electrolyte-based electrochemical capacitors.

The fabricated composite sheets were characterized using XRD and XPS analyses to investigate their composition and chemical bonding. **Figure 2.14**A shows XRD patterns of p-CNTs, a-CNTs, Ru@p-CNTs, and Ru@a-CNTs, with all cases

revealing a 26.2° diffraction peak corresponding to the (002) plane of graphitic carbon in CNTs. In the cases of Ru@p-CNTs and Ru@a-CNTs, several sharp peaks at 38.3, 42.2, 44.0, 58.3, 69.4, and 78.4° related to the (100), (002), (101), (102), (110), and (103) diffraction planes, respectively, of metallic hexagonal close-packed Ru are detected.[62] XPS analysis (**Figure 2.14**B) supports the predominance of metallic Ru ($Ru^0$) in the Ru NPs deposited on the CNT networks. To characterize the chemical bonding structure, the C 1s core level spectra were deconvoluted into six subpeaks with binding energies centered at 284.5, 285.5, 286.6, 288.3, 289.5, and 291.1 eV corresponding to the C=C, C–C, C–O, C=O, O–C=O–, and π-π* transitions, respectively.[63] After acid treatment, the relative fraction of oxygen-containing functional groups of C–O, C=O and O–C=O– increase. Because the treatment forms defect sites in the graphitic resonance bonding of CNTs and introduces oxygen-containing chemical bonds,[64-66] the surface of CNTs is changed to become hydrophilic. Additional peaks located in the low binding energy region observed in Ru@p-CNTs and Ru@a-CNTs correspond to the overlapping Ru 3d core level spectra. The Ru 3d core-level spectra of Ru@p-CNTs and Ru@a-CNTs were deconvoluted into three pairs of spin–orbit doublets at 280.1, 281.2, and 282.4 eV (Ru $3d^{5/2}$) and 284.3, 285.4, and 286.6 eV (Ru $3d^{3/2}$), corresponding to Ru, $RuO_2$, and $Ru(OH)_3$, respectively.[67-69] As shown in the figure, along with the chemical state of metallic Ru, the oxidized states of Ru are also observed. This oxidized Ru form likely originates from the Ru ions anchored on oxygen functional groups or native Ru oxides formed on the surface of deposited Ru metal NPs, as no noticeable diffraction peaks of ruthenium oxides are observed in the XRD patterns.[70]

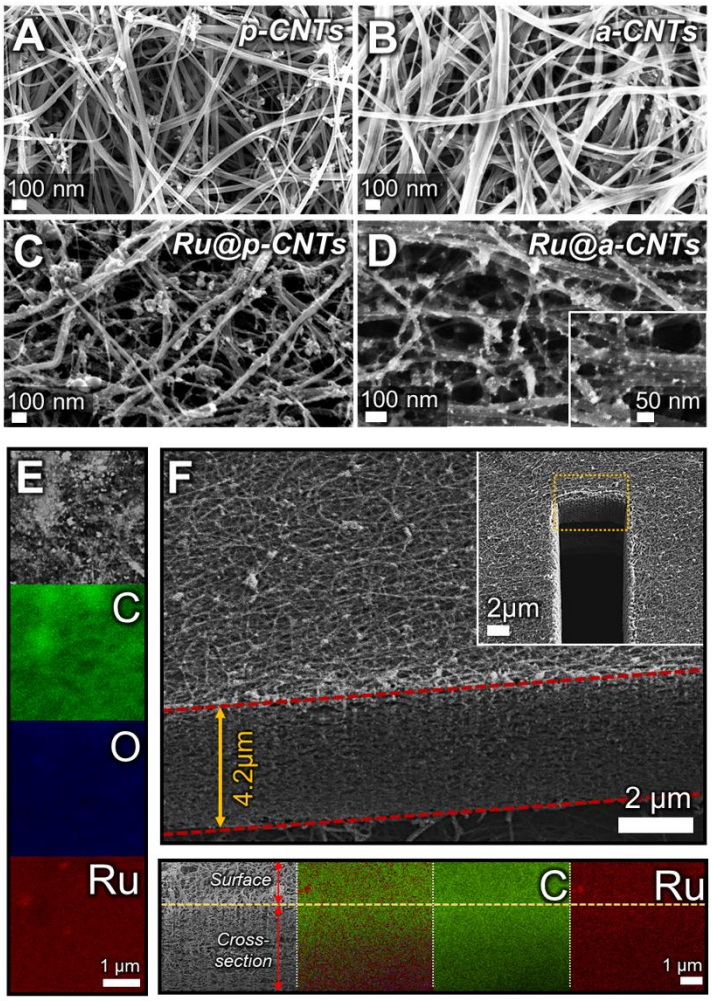


**Figure 2.13.** FE-SEM images of (A) p-CNTs, (B) a-CNTs, (C) Ru@p-CNTs, and (D) Ru@a-CNTs. EDS mapping images of the surface (E) and cross-section (F) of Ru@a-CNTs.

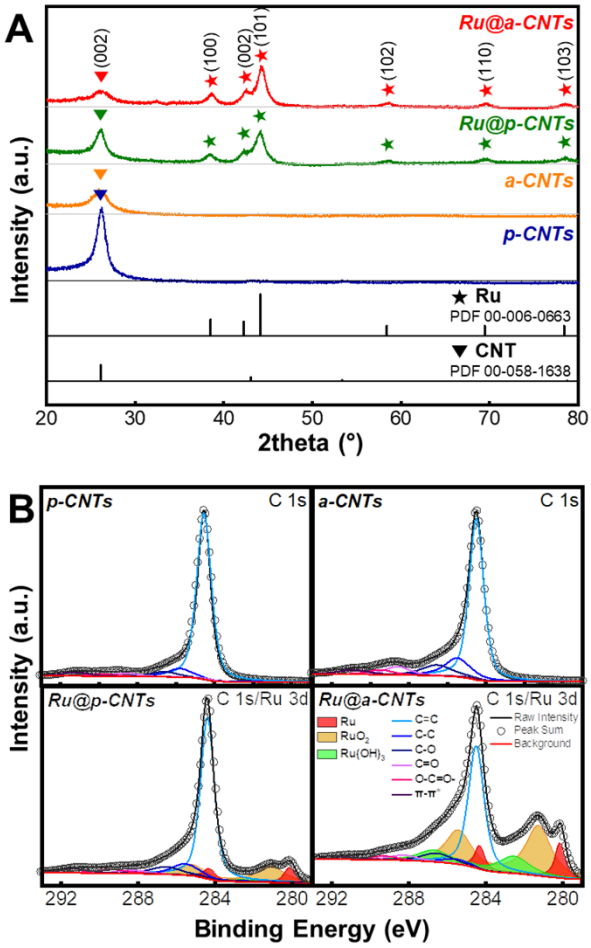


**Figure 2.14.** (A) XRD patterns of p-CNTs, a-CNTs, Ru@p-CNTs, and Ru@a-CNTs. (B) The XPS C 1s spectra for p-CNTs and a-CNTs and C 1s/Ru 3d spectra for Ru@p-CNTs and Ru@a-CNTs with deconvoluted subpeaks. Both of the Ru@p-CNTs and Ru@a-CNTs show three additional deconvoluted subpeaks, indicating Ru, $RuO_2$, and $Ru(OH)_3$.

### 2.4.5. Electrochemical properties of Ru@a-CNTs

The electrochemical performance, including the specific capacitance, rate capability, and cycling stability, was evaluated based on a three-electrode cell configuration, as shown in **Figure 2.16**A–D. The cyclic voltammetry (CV) curves for p-CNTs, a-CNTs, Ru@p-CNTs, and Ru@a-CNTs, within a potential range of 0-0.8 V and at scan rates from 10 to 1000 mV $s^{-1}$, are shown in **Figure 2.15**A. It is noteworthy that the specific capacitance of a-CNTs is approximately twice that of p-CNTs. The increase in capacitance after acid treatment could be attributed to i) improved wettability for electrolytes, which facilitates the accessibility of mobile ions to the outer and inner surfaces of the CNT nanosheets, and ii) the incorporation of pseudocapacitive faradic reactions occurring at the oxygen-containing functional groups.[71, 72] In addition, the integration of Ru NPs into CNT nanosheets further increases the specific capacitance due to the pseudocapacitive energy storage provided by Ru NPs (indicated by the single pair of redox peaks in **Figure 2.15**A).

Electrochemical impedance spectroscopy (EIS) was used to further characterize the enhanced electrochemical performance of Ru@a CNTs. **Figure 2.15**B shows Nyquist plots for p-CNTs, a-CNTs, Ru@p-CNTs and Ru@a-CNTs. In order to separate each resistivity contribution to the overall polarization, an equivalent circuit model (shown in the inset of **Figure 2.15**B) was constructed, with the fit results shown as black solid lines. The $R_s$ values for p-CNTs, a-CNTs, Ru@p-CNTs and Ru@a-CNTs are nearly identical due to the consistent electrolyte composition and cell configuration in all cases. The charge transfer resistance ($R_{ct}$) associated with the semicircle observed in the mid-frequency region decreased in the following order: p-CNTs (0.80 Ω) > a-CNTs (0.60 Ω) > Ru@p-CNTs (0.29 Ω) > Ru@a-CNTs (0.20 Ω). The lowest $R_{ct}$ observed for Ru@a-CNTs could be attributed to i) an increase in

the interfacial surface area as a result of acid treatment, and ii) facilitation of electron transfer due to pseudocapacitive redox reactions of Ru NPs.[73] All curves in the low frequency range are linear lines with high slopes, typical of the capacitive behavior of porous carbon electrodes without diffusion limitation.[74, 75]

**Figure 2.15**C shows the changes in specific capacitance as a function of scan rate by repeating the capacitance measurement of CNT nanosheet-based electrodes ten times at each scan rate. At a scan rate of 10 mV $s^{-1}$, the average specific capacitances for p-CNTs, a-CNTs, Ru@p-CNTs, and Ru@a-CNTs are 12.5, 21.5, 162.5, and 253.3 F $g^{-1}$, respectively. In all cases, the specific capacitance remains exceptionally stable at each scan rate because the CNTs potentially facilitate not only fast electron transfer but also efficient interfacial charge transfer. Remarkably, Ru@a-CNTs exhibit a capacitance about 20 times higher than that of p-CNTs, a result of the reversible pseudo-capacitive reaction of Ru NPs and the enhanced affinity to electrolytes induced by acid treatment. From the remarkable electrochemical performance of Ru@a-CNTs, it is clear that CNT-based nanocomposite sheets offer advantages for practical applications. The use of Ru@CNTs as additive-free and lightweight electrodes can improve the gravimetric and volumetric specific capacitances and increase the intrinsic capacitance through EDL formation in porous CNT sheets. Moreover, Ru@a-CNTs demonstrate remarkable cyclability, displaying no noticeable performance and structural degradation over 2000 cycles, as shown in **Figure 2.15**D.

Finally, *ex situ* XPS analysis as a function of applied electrode potential (**Figure 2.16**) was performed to determine the change in Ru chemical structure and the reversibility of the reaction during the charge/discharge process. The Ru 3p core-level spectra were selected for study, and these spectra were deconvoluted into three sub-peaks at 461.9, 462.7, and 464.1 eV, corresponding to Ru, $RuO_2$, and Ru(OH)3,

respectively.[76] The overall energy storage behavior of Ru@a CNTs is governed by the following electrochemical reaction:

$$Ru + \delta H_2O \leftrightarrow Ru(OH)_\delta + \delta H^+ + \delta e^- \ (0 \leq \delta \leq 3) \qquad (2.2)$$

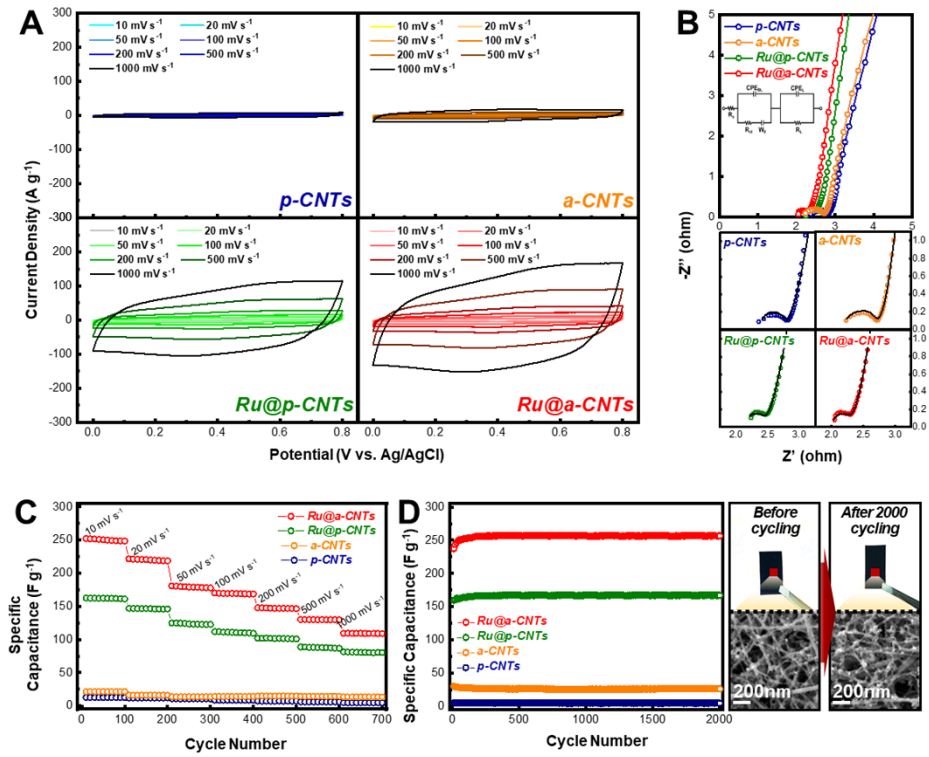


**Figure 2.15.** The electrochemical performances of p-CNTs, a-CNTs, Ru@p-CNTs, and Ru@a-CNTs: (A) CV curves at different scan rates of 10-1000 mV $s^{-1}$, (B) Nyquist plots at open circuit potential in the frequency range of 100 kHz-0.01 Hz, (C) specific capacitances and rate capabilities, and (D) long-term cyclability at a scan rate of 10 mV $s^{-1}$ (Photographs and FE-SEM images of Ru@a-CNTs before (left) and after (right) 2000 charge-discharge cycles). The current density and specific capacitance were calculated based on the entire weight of each electrode.

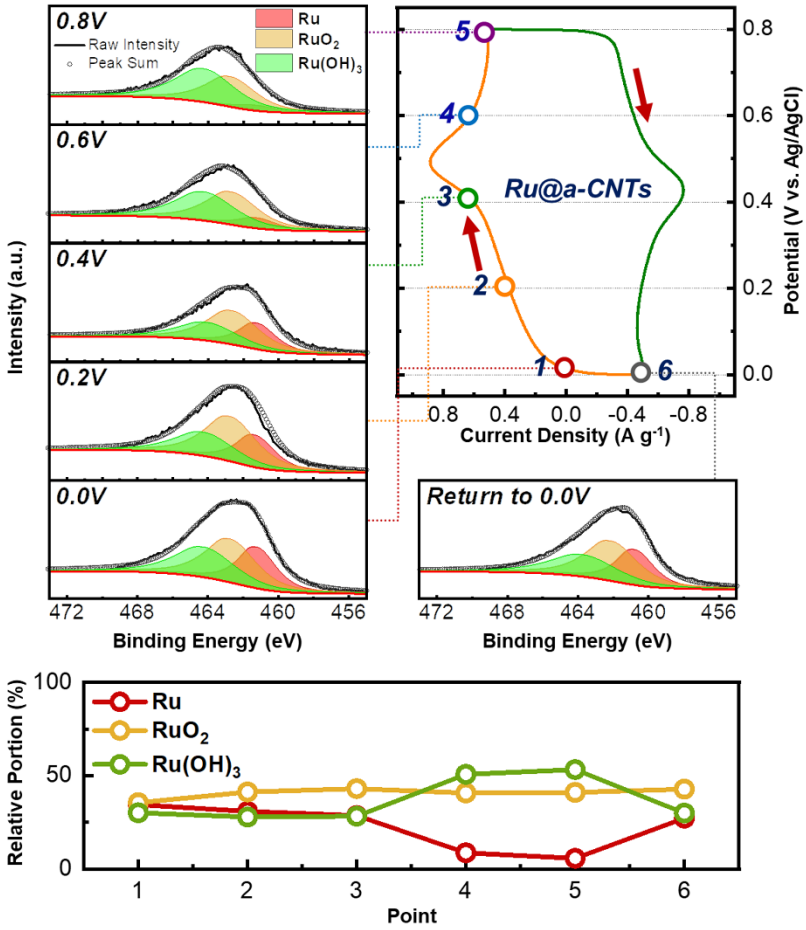


**Figure 2.16.** XPS Ru 3p core-level spectra for Ru@a-CNTs at 6 points in the given CV curve. The spectra were deconvoluted into three subpeaks indicating Ru, $RuO_2$, and $Ru(OH)_3$.

### 2.4.6. Application and commercial viability of Ru@a-CNTs-based deformable capacitors

The superior mechanical properties of CNT sheets are critical in maintaining electrochemical performance and structure under deformation. To demonstrate their utility as a deformable electrode, quasi-solid-state electrochemical capacitors were assembled using Ru@a-CNTs and a poly(vinyl alcohol)-phosphoric acid (PVA-$H_3PO_4$) hydrogel electrolyte (**Figure 2.17**A). The hydrogel electrolyte permeates the entire electrode due to the hierarchical porous structure of the Ru@a-CNTs, forming robust interfaces between the nanosheets and the hydrogel. The capacitors achieve excellent cycling stability, retaining approximately 92% of the initial capacitance even after 20,000 repeated cycles, as shown in Figure 2.18B. The performance of the capacitors was evaluated under extreme mechanical deformations of bending (**Figure 2.17**C) and stretching (**Figure 2.17**D), typical motions encountered in portable devices. The mechanical robustness of the Ru@a-CNT-based capacitors is due to the inherent flexibility of the CNT nanosheets and the highly stable electrode-electrolyte interface.

The practical applicability of Ru@a-CNTs-based deformable capacitors was demonstrated by connecting the capacitors to a commercial device. Multiple cells in series are tested to provide sufficient power for a wearable electronic device, as depicted in **Figure 2.18**A. **Figure 2.18**B shows the voltage profiles according to the number of cells (single, 2, 3, and 6-series) at a specific current of 1 A $g^{-1}$, and the voltage window is extended from 1.0 V to 6.0 V. All voltage profiles exhibit the typical triangular-shaped GCD curves of electrochemical capacitors. The linearity between the number of cells and voltage drops indicates that there is no additional resistance by being connected in series (right of **Figure 2.18**B). Hence, it is possible

to easily construct a power source with a high operating voltage for practical applications. Finally, the six capacitors connected in series successfully charge a smartwatch, and a reflective display showing the charging state is presented (**Figure 2.18**C).

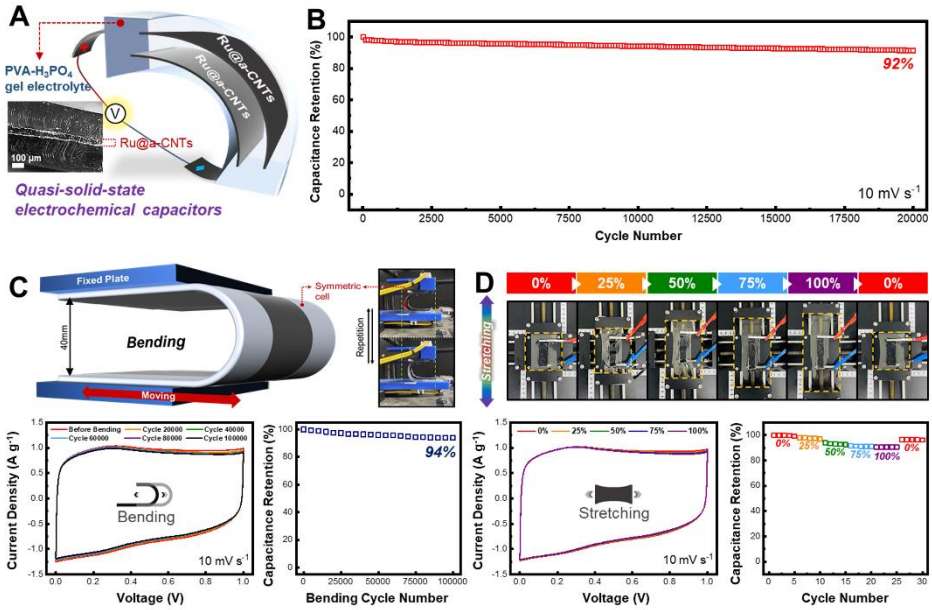


**Figure 2.17.** (A) Schematic of quasi-solid-state electrochemical capacitors composed of Ru@a-CNTs and a PVA-$H_3PO_4$ gel electrolyte. (B) Cyclability of quasi-solid-state electrochemical capacitors at a scan rate of 10 mV $s^{-1}$ for 20000 cycles. (C) and (D) CV curves at a scan rate of 10 mV $s^{-1}$ and corresponding capacitance retention subject to bending and stretching. The bending test was performed up to 100000 cycles and the elongation of stretching was 100%. Note that all electrochemical properties were calculated based on the total weight of the electrodes.

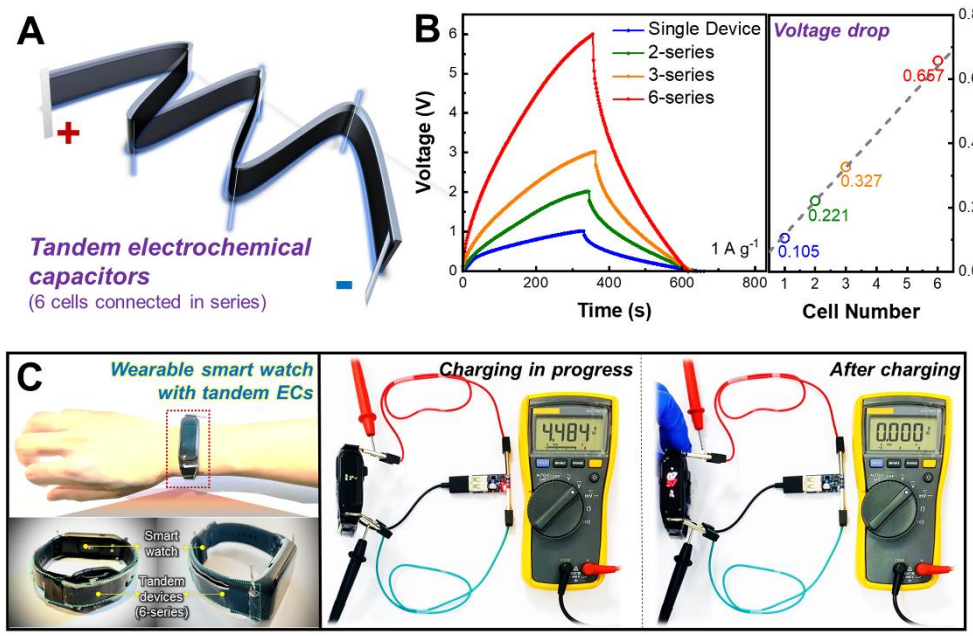


**Figure 2.18.** (A) Schematic illustration of six Ru@a-CNTs-based quasi-solid-state electrochemical capacitors connected in series. (B) Voltage profiles with the number of cells in series as measured at a specific current of 1 A $g^{-1}$. (C) Charging a commercial smartwatch by six capacitors.

## 2.5. Summary

In summary, this study illustrates the exceptional performance of FC-CVD-synthesized CNT current collectors, demonstrating unique compatibility with battery and capacitor-type electrodes. These current collectors effectively circumvent the inherent drawbacks of conventional metal-based counterparts, as well as the challenges associated with the sheet formation of traditional CNTs. The high specific surface area and reduced agglomeration characteristics of FC-CVD-synthesized CNTs directly address the adhesion and dispersion problems often associated with conventional methods. This study, which consists of two main sections, highlights the versatile potential of CNT-based current collectors.

The first part of the study demonstrates the potential of CNT-based current collectors to effectively mitigate inherent limitations commonly associated with active materials in battery and capacitor. The unique properties of these current collectors, such as highly porous structures, large specific surface areas, and low densities, improve the electrochemical performance of energy storage systems. The second part of the study presents a novel process for fabricating lightweight, flexible composite electrodes using ruthenium nanoparticle (Ru NP)-embedded layered CNT nanosheets. CNT nanosheets perform multifunctional roles, contributing to capacitive storage, serving as an effective platform for additive-free electrodes, and functioning as deformable and durable current collectors. The integration of Ru NP-decorated CNT nanosheets with hydrogel electrolytes facilitated the fabrication of deformable quasi-solid-state electrochemical capacitors, which meet a variety of requirements for portable device power sources.

In essence, this study confirms the considerable potential of FC-CVD-synthesized CNTs in advancing energy storage devices and introducing novel

applications for current collectors. It represents a significant step toward overcoming the traditional roles and limitations of conventional current collectors, and heralds a new era in the development and improvement of energy storage systems.

# CHAPTER 3

# Transition Metal@CNT Sheets as Durable HER Catalysts-Integrated Electrodes for Water Electrolysis

The purpose of this chapter is to demonstrate how the distinctive material and structural advantages of FC-CVD-synthesized CNT assemblies discussed in the previous chapter can be effectively applied to energy conversion applications. As mentioned earlier, CNT assemblies have a highly interconnected three-dimensional network that provides a large surface area for electrochemical reactions. Harnessing these structural advantages leads to significant improvements in catalyst particle distribution, facilitating more effective contact with reactants and resulting in increased catalytic activity and reaction efficiency. In addition, the FC-CVD process produces high-purity CNTs with fewer defects, which promotes improved electron transport pathways and enhances overall electrocatalytic performance.

The approach involved the design of an integrated catalyst-support electrode for

the hydrogen evolution reaction (HER), which is intended for direct application in industrial-scale electrolysis systems, particularly anion exchange membrane water electrolysis (AEMWEs). Three-dimensional (3D) CNT sheets were synthesized by FC-CVD method and subsequently decorated with nickel iron sulfide (NFS) catalysts by a hydrothermal process. The hierarchical structure and inherent porosity of the CNT sheets facilitated uniform catalyst deposition in both lateral and thickness directions, efficient transport of electrolyte ions, and extended catalyst-electrolyte interface. In addition, the CNT-based electrode design offers a distinct advantage over conventional nickel foam-based electrodes, as it allows for additional performance improvements without increasing the thickness or volume by simply stacking the electrode layers. In particular, the developed electrode demonstrated compatibility with actual electrolysis cells used in industrial-scale systems and long-term durability. When used in AEMWE systems, the integrated electrode design offered significant benefits such as reduced ohmic losses, increased mass transport efficiency, enhanced catalytic activity, and improved overall energy efficiency. These advantages effectively address some of the key challenges associated with conventional AEMWE systems.

The results presented herein not only underscore the potential of this novel integrated electrode design for practical applications in HER and related processes, but also provide valuable insights into the design of high performance electrocatalysts and electrode materials for a wide range of electrochemical energy conversion systems, including AEMWEs.

## 3.1. Introduction

Electrocatalytic water splitting systems powered by renewable energy sources for green hydrogen production are expected to be one of the most sustainable energy conversion technologies to replace fossil fuels in the near future. Among various water electrolysis methods, anion exchange membrane water electrolysis (AEMWEs) has been developed to mitigate the drawbacks of proton exchange membrane water electrolysis (PEMWE) and alkaline water electrolysis (AWE) for the following reasons: i) the efficient hydrogen and oxygen evolution reaction (HER and OER) catalyzed by low cost and earth-abundant non-precious transition metals [77] and ii) the zero gap cell configurations that allow the production of high-purity hydrogen due to reduced gas crossover.[78] Despite advancements in non-precious metal-based catalysts for AEMWEs, achieving performance comparable to Pt-based HER catalysts is challenging due to their lower intrinsic catalytic activity and reduced stability in alkaline conditions.[79, 80]

Designing durable catalyst electrodes for AEMWEs is particularly challenging for several reasons. First, HER catalysts in AEMWEs are typically made of non-precious metals, which have inherently lower catalytic activity compared to precious metals. Achieving comparable efficiencies requires higher loading of these catalysts, which increases the risk of detachment or dissolution under operating conditions, resulting in a gradual loss of active catalytic sites. Second, conventional electrode structures for AEMWEs often rely on binders. The adhesion between the catalysts and the substrate in these structures can be inherently weak, increasing the likelihood of catalyst delamination over extended operating periods. This phenomenon further reduces the active catalyst surface area, and consequently, the overall HER performance. Finally, repeated cycles of hydrogen production and associated

changes in local conditions place significant stress on the catalysts and electrode materials. The continuous expansion and contraction, as well as the constant evolution of gas, can cause strain on the electrode structure, potentially leading to structural degradation and failure over time. Hence, various methods have been developed to mitigate the durability degradation, including i) the direct growth of catalysts on substrates,[81, 82] ii) the formation of protective layers on catalyst surfaces,[83, 84] and iii) the incorporation of robust support materials into the electrode structure.[ref] However, most of the proposed strategies are limited to fully satisfy the durable electrocatalysts of AEMWEs at an industrial scale due to the following challenges: i) potential corrosion of metallic substrates,[85] ii) insufficient adhesion between catalysts and substrates,[86] and iii) the difficulty in precisely controlling the protective layer.[87]

In this study, the HER electrocatalyst-integrated electrode composed of ultrafine nickel-iron sulfide particles supported on FC-CVD-synthesized CNT sheets (NFS@CNTs) was rationally designed to address these issues. The combination of NFS catalysts with modulated electronic configurations and alkaline stable CNTs improves both HER activity and durability. The synergistic effect between nickel and iron atoms in the lattice optimizes the hydrogen binding energy, while the incorporation of sulfur modulates the electronic structure to enhance catalytic performance.[88] In addition, the large surface area of CNTs ensures homogenous catalyst distribution, leading to improved catalytic activity and hydrogen production efficiency. The extensive porosity of CNTs enhances mass transport through better diffusion of reactants to the catalyst surface and more efficient product removal.

The unique structural features of the FC-CVD-synthesized CNT sheets further enhance the HER electrocatalytic performance. Compared to other CNTs and conventional carbon-based PTLs such as carbon paper and cloth, the longer CNTs

enhance electron pathways and mechanical strength, ensuring consistent performance and durability.[89] In addition, the uniformity in the three-dimensional direction allows numerous catalysts to be homogeneously decorated, maximizing the HER active surface area. Furthermore, the high surface-to-volume ratio allows for performance tuning by simply stacking the electrodes. This feature is critical because by adjusting the number of stacked layers, the electrocatalytic performance can be fine-tuned to meet specific application requirements, providing a customizable and efficient approach to hydrogen production. As a result, NFS@CNTs was successfully applied as an HER electrode in the practical AEMWE cell, achieving a sustained cell voltage of 1.88 V with a degradation rate of 0.02 mV $h^{-1}$ at a current density of 0.5 A $cm^{-2}$ for 1000 h. The exceptional properties of FC-CVD-synthesized CNT sheets-based catalyst-integrated electrodes provide new perspectives for boosting HER electrocatalytic performance, inspiring breakthroughs in sustainable hydrogen production and advancing the development of clean energy technologies.

## 3.2. Experimental Methods

### 3.2.1. Synthesis of NFS@CNTs composite electrodes

The precursor solution to decorate NFS particles on CNT sheets was prepared by dispersing nickel(II) chloride hexahydrate ($NiCl_2 \cdot 6H_2O$) (Sigma-Aldrich, USA), iron(II) chloride hexahydrate ($FeCl_2 \cdot 6H_2O$) (Sigma-Aldrich, USA), sodium thiosulfate ($Na_2S_2O_3$) (Sigma-Aldrich, USA), and urea ($CO(NH_2)_2$) (Sigma-Aldrich, USA) as nickel, iron, sulfur precursor, and hydrolysis controlling agent, respectively, in distilled water. The CNT sheets were dipped in the precursor solution, then transferred to a 60 mL Teflon-lined stainless-steel autoclave for hydrothermal reaction. The reactor was treated at 120°C for 12 h and then cool down to the ambient atmosphere. The pre-reacted CNT sheets were transferred to NaOH solution to proceed with the second hydrothermal reaction to obtain the final products by complete sulfidation.[90] Finally, the obtained NFS@CNTs were freeze-dried for 24 h to completely eliminate the residual moisture. To verify the Fe alloying and sulfur addition effects of NFS@CNTs, Ni@CNTs, NiFe@CNTs, and NiS@CNTs were also prepared with different precursor solution compositions.

### 3.2.2. Material characterization

The surface morphologies of composites were characterized by field emission scanning electron microscopy (FE-SEM, JSM-7900F, JEOL, Japan) at an acceleration voltage of 2 kV. The elemental composition of nanocomposites was measured by energy dispersive X-ray spectroscopy (EDS, Oxford Instruments, United Kingdom) coupled with FE-SEM. The cross-sectional morphology of

NFS@CNTs was analyzed after milling using a focused ion beam (FIB, Helios 650, FEI, USA). The specific surface area, total pore area, and pore size distribution of CNT sheets were measured by BET (Autosorb® iQ-MP, Quantachrome Instruments, USA) analysis of the nitrogen adsorption isotherms at 77 K. The XPS analysis was performed on sputter-cleaned surfaces using a K-Alpha+ instrument (Thermo Fisher Scientific, USA) equipped with a monochromatic Al Kα X-ray source (1486.6 eV). Raman spectra were acquired using a Raman microscope (DXR2xi, Thermo Scientific, USA) with an excitation wavelength of 532 nm laser. The XRD analysis was performed on an Empyrean (Malvern PANalytical, Netherland) with a Cu Kα radiation wavelength of 1.542 Å.

### 3.2.3. Electrochemical investigation

The electrochemical performances were evaluated using a three-electrode cell with 1 M KOH alkaline electrolyte solution (Samchun chemical, Korea). The three-electrode half-cell consisted of a working electrode (prepared electrodes in this work), reference electrode (Hg/HgO), and counter electrode (graphite rod). For the HER measurements, the linear sweep voltammetry (LSV) was conducted in a potential range from −0.57 to 0.05 V (vs. RHE) with a scan rate of 5 mV $s^{-1}$. The durability of electrodes was determined by the chronopotentiometry measurements at current densities of 10, 20, 30, 40, and 50 mA $cm^{-2}$. The EIS measurements were recorded in the frequency range of 100 kHz-0.01 Hz by using an AC voltage of 10 mV. All these electrochemical measurements were performed using a multichannel potentiostat (VMP3, BioLogic Science Instruments, France).

### 3.2.4. Configuration of mini-scale AEMWE single-cell

For the mini-scale AEMWE single-cell test, cathode, anode, AEM, and porous transport layer (PTL) were prepared as follows. Since the active area of the designed AEMWE cell is 4.9 $cm^2$, NFS@CNTs were prepared by cutting them into 25 mm in diameter as the cathode of an AEMWE cell. For the anode, $Co_3O_4$ pastes were coated on Ni foam (pore size 450 μm, Alantum, Korea). A commercial AEM (PiperION-A15R, 15 μm thickness, Versogen, USA) was used as the separator (AEM was soaked in 1.0 M KOH for at least 2 h prior to cell assembly). The PTL for the cathode and anode were manufactured by pressing 10-layers (2.7 mm) and 14-layers (3.5 mm) of Ni foam, respectively. After tightening the cell to a pressure of 25 N $m^{-1}$, the electrochemical performances were evaluated by circulating an electrolyte of 1.0 M KOH at a rate of 100 mL $min^{-1}$ under an operating temperature of 60 °C.

## 3.3. Results & Discussions

### 3.3.1. Morphological and microstructural investigation of NFS@CNTs

The decoration of catalyst particles (Ni, NiFe, NiS, and NFS) on FC-CVD-synthesized CNT sheets was achieved by a two-step hydrothermal reaction as shown in **Figure 3.1**. The as-synthesized CNT sheets were immersed into an aqueous precursor solution containing Ni, Fe, and S. Subsequently, the partially reacted CNT sheets underwent a second hydrothermal reaction in a NaOH solution for extensive oxide or sulfate reduction. Consequently, the resulting NFS@CNT composite sheets serve as freestanding, conductive, and integrated electrode structures with uniformly grown catalyst particles suitable for HER.

Extensive investigations were carried out to elucidate the morphological and microstructural characteristics of the synthesized catalysts on the CNT sheets. FE-SEM was used to observe the morphologies of Ni@CNTs, NiFe@CNTs, NiS@CNTs, and NFS@CNTs. The FE-SEM images (**Figure 3.2**A-D) confirmed the uniform decoration of each catalyst type on the CNT sheet surfaces. This structure provides abundant sites for catalyst particle attachment due to its large surface area. In addition, the layered structure allows catalyst support not only on the sheet surface but also throughout its thickness, thereby increasing the number of catalytic reaction sites per unit area/volume. The cross-sectional morphology and EDS mapping image of the NFS@CNTs (**Figure 3.2**E) show the three-dimensional uniformity, highlighting the unique structural advantages of CNT sheets.

The individual NFS catalyst particle synthesized on CNT sheets was analyzed by transmission electron microscopy (TEM) as shown in **Figure 3.3**. The selected area electron diffraction (SAED) pattern shows distinct diffraction rings, indicating

the polycrystalline nature of NFS@CNTs. The high-resolution TEM (HR-TEM) image and inversed fast Fourier transform (IFFT) image (in the area marked by red square) of NFS@CNTs demonstrate that distinct lattice fringes correspond to (211), (102), and (101) planes of $Ni_3S_2$ phase, respectively. In addition, the EDS mapping images present a uniform distribution of Ni (green), Fe (blue), and S (orange) elements in the NFS@CNTs, indicative the successful formation of nickel iron sulfide particles on CNT sheets.

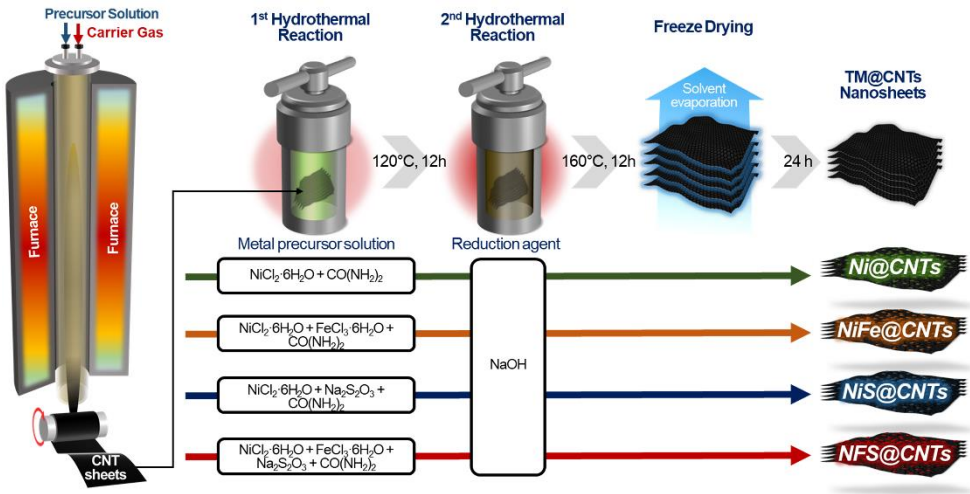


**Figure 3.1.** The fabrication procedures of Ni@CNTs, NiFe@CNTs, NiS@CNTs, and NFS@CNTs

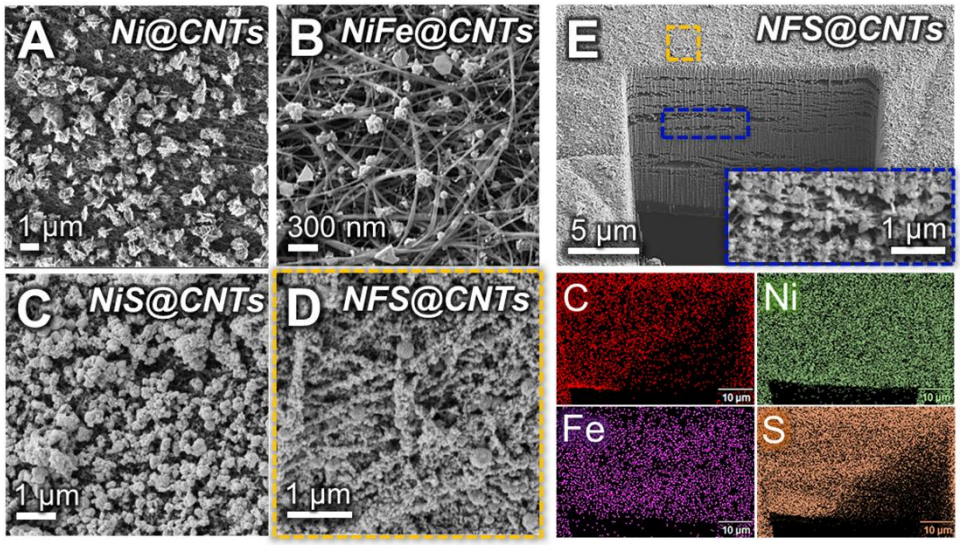


**Figure 3.2.** The surface FE-SEM images of (A) Ni@CNTs, (B) NiFe@CNTs, (C) NiS@CNTs, and (D) NFS@CNTs. (E) The cross-section morphology and EDS mapping image of NFS@CNTs.

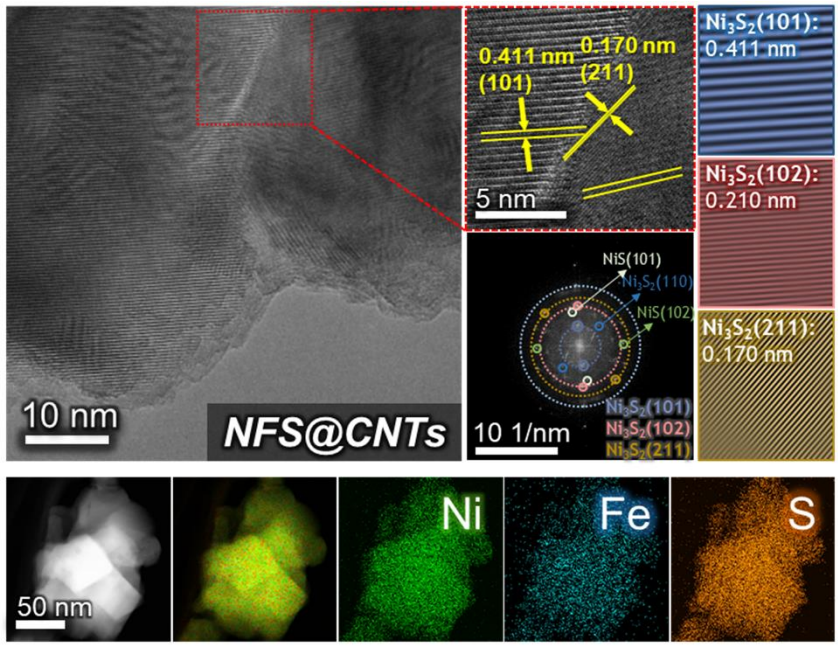


**Figure 3.3.** HR-TEM image, SAED pattern, and TEM/EDS images of the NFS catalyst particle in NFS@CNTs.

### 3.3.2. Structural and compositional characterization of NFS@CNTs

The X-ray diffraction (XRD) analysis was performed to identify the crystal structure of Ni@CNTs, NF@CNTs, NiS@CNTs, and NFS@CNTs as shown in **Figure 3.4**. All catalyst samples show a diffraction peak centered at 26°, mainly due to the (002) planes of the CNTs. Ni@CNTs and NF@CNTs exhibit diffraction peaks at 44.5, 51.9, and 76.4°, indexed to the (111), (200) and (220) planes of metallic Ni (JCPDS No. 04-0850). For sulfide-based catalysts (NiS@CNTs and NFS@CNTs), the distinct peaks centered at 21.8, 31.1, 37.9, 44.6, 50.1, and 55.2° were observed, which correspond well to the (101), (110), (003), (202), (113), and (122) facets of $Ni_3S_2$ (JCPDS No. 04-1418), respectively. Notably, NF@CNTs and NFS@CNTs show negative peak shifts of 0.49 and 0.60° (the right side of **Figure 3.4**) respectively, due to the increased d-spacing since the greater atomic radius of Fe compared to that of Ni, implying the existence of alloying between Ni and Fe.[91]

X-ray photoelectron spectroscopy (XPS) was analyzed to investigate the chemical composition and elemental valence states in the near-surface region of catalysts. The XPS survey spectra (**Figure 3.5**A) demonstrate the main peaks attributable to C 1s, S 2p, Fe 2p, Ni 2p, and O 1s orbitals, mainly indicating the containing of these elements in the composite. **Figure 3.5**B shows the high-resolution Ni 2p XPS spectra of Ni@CNTs, NF@CNTs, NiS@CNTs, and NFS@CNTs, in which the $2p^{3/2}$ and $2p^{1/2}$ signals appear with an area ratio of 2:1, respectively. Upon Fe incorporation (NF@CNTs and NFS@CNTs), a positive peak shift of 0.4 eV is observed, which is attributed to a significant change in the electronic environment around Ni atoms. As shown in **Figure 3.6**C, a positive peak shift of 0.46 eV between NiS@CNTs and NFS@CNTs was also observed in the S 2p spectra. Overall, the positive peak shift in the Ni 2p and S 2p spectra upon Fe

incorporation can be explained by the electronegativity differences among Ni (1.91), Fe (1.83), and S (2.58) atoms.[92] When Fe is incorporated into the structure, the lower electronegativity of Fe compared to Ni leads to a redistribution of electron density in the metal-sulfur bonds, pulling the electron density slightly more toward the sulfur atoms due to its highjjer electronegativity. This shift suggests an altered local chemical environment and bonding characteristics, which significantly impact the material's electronic structure and properties. These changes in electronic structure can profoundly affect catalytic properties, hydrogen adsorption/desorption behavior, and overall performance in HER and related processes.

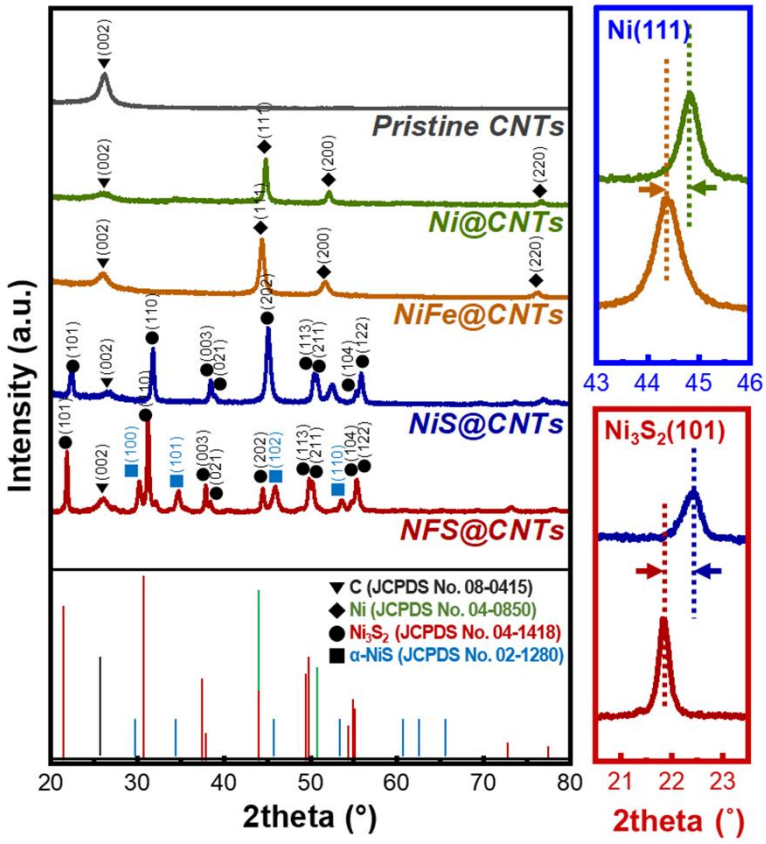


**Figure 3.4.** XRD patterns of CNT-based electrodes: pristine CNTs, Ni@CNTs, NiFe@CNTs, NiS@CNTs, and NFS@CNTs.

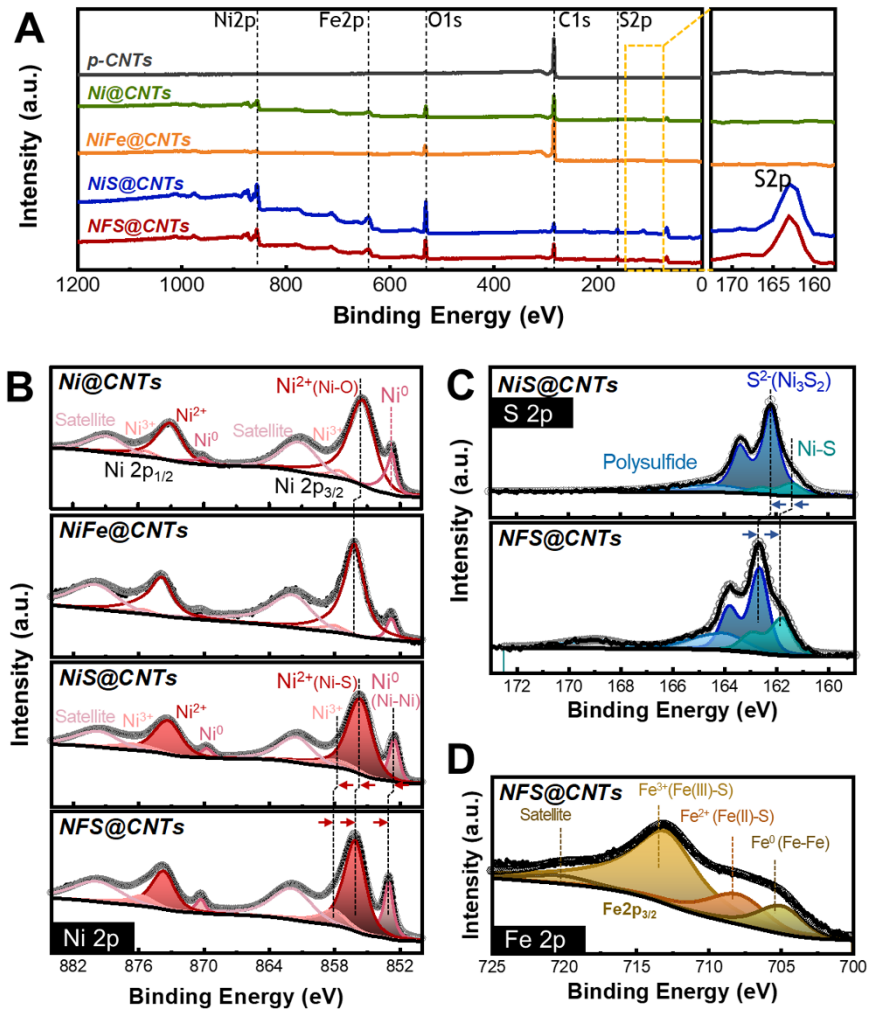


**Figure 3.5.** Sub-peak fitted XPS spectra: (A) survey spectra, (B) Ni 2p, (C) S 2p, and (D) Fe 2p.

### 3.3.3. Electrochemical analysis: HER catalytic performances of NFS@CNTs

The HER activity of these electrocatalysts was evaluated in a three-electrode cell in 1.0 M KOH. **Figure 3.6**A demonstrated the LSV curves of prepared electrodes measured at a scan rate of 5 mV $s^{-1}$ with 85% iR-correction. NFS@CNTs exhibited a low overpotential of 109 mV at a current density of 10 mA $cm^{-2}$, which was superior to those of Ni@CNTs (327 mV), NF@CNTs (230 mV), and NiS@CNTs (159 mV). The Tafel slope was examined to elucidate the underlying mechanism of HER activity, as shown in **Figure 3.6**B. This kinetic parameter provides insight into reaction kinetics and helps to identify the rate-determining step (RDS) of the HER process. According to the classic theory, the HER mechanism in alkaline solution involves several basic steps: i) Volmer reaction ($H_2O + e^- \rightarrow H^* + OH^-$) is the initial step including electrochemical dissociation of $H_2O$ and hydrogen adsorption; this step is considered the RDS when the Tafel slope is about 120 mV $dec^{-1}$, ii) Heyrovsky reaction ($H_2O + H^* + e^- \rightarrow OH^- + H_2$) or Tafel reaction ($H^* + H^* \rightarrow H_2$) are the subsequent hydrogen desorption; each step is considered the RDS when the Tafel slope is about 40 or 30 mV $dec^{-1}$, respectively.[93] All Tafel slopes in Figure 3B are above 40 mV $dec^{-1}$, suggesting that a combined Volmer-Heyrovsky mechanism governs the HER process. The lowest Tafel slope of NFS@CNTs (64.2 mV $dec^{-1}$) indicates that the kinetics of the water dissociation step (Volmer reaction) are effectively facilitated compared to the other electrodes.[94]

**Figure 3.7**A shows cyclic voltammetry (CV) curves at different scan rates of pristine CNTs, Ni@CNTs, NF@CNTs, NiS@CNTs, and NFS@CNTs to calculate the electrochemical active surface area (ECSA). NFS@CNTs had the highest ECSA, with a $C_{dl}$ of 12.8 mF $cm^{-2}$, superior to that of Ni@CNTs (3.1 mF $cm^{-2}$), NF@CNTs (3.1 mF $cm^{-2}$), and NS@CNTs (10.2 mF $cm^{-2}$). The large $C_{dl}$ of NFS@CNTs was

closely associated with superior HER catalytic performances , providing more active sites than the other samples tested in this study. The smaller charge transfer resistance ($R_{ct}$) of NFS@CNTs also directly reflect their increased catalytic activity. According to Nyquist plots in **Figure 3.7**C, NFS@CNTs exhibited a significantly reduced $R_{ct}$ value (8.0 Ω) compared to those of Ni@CNTs, NF@CNTs, and NiS@CNTs, indicating an improved electron transfer rate and faster catalytic kinetics. These differences could be attributed to the geometric properties of the catalyst, such as particle size, shape, and surface roughness. Surface SEM images shown in **Figure 3.2** suggest that smaller particles of NFS@CNTs result in a larger exposed surface area for electrochemical reactions, providing more active sites for adsorption and desorption of reaction intermediates. Consequently, the catalytic reaction becomes more efficient due to the enhanced opportunities for the reaction to proceed at a faster rate.

Durability is another key criterion in the evaluation of electrocatalysts. As shown in **Figure 3.8**A, the durability of NFS@CNTs was evaluated in comparison to NFS grown identically on commercial substrates (Ni foam (NF) and carbon cloth (CC)). This evaluation was performed using a multi-step chronopotentiometry test by increasing the current density from -10 to -50 mA $cm^{-2}$. Unlike NFS@NF and NFS@CC, a stable current density is observed during each step measurement. This stable performance is likely due to the superior mass transport and conductivity over the other substrates.[95] **Figure 3.8**B shows the polarization curves of NFS@CNTs at the first and 500th cycles derived from continuous CV scanning between -0.57 and 0.05 V vs. RHE at a scan rate of 5 mV $s^{-1}$ in 1.0 M KOH. Impressively, NFS@CNTs maintained efficient performance after 500 cycles with only negligible cathodic shift in the polarization curve. After HER electrolysis, no significant changes were observed in $R_{ct}$, SEM images, and Raman spectra, indicating the stability of

NFS@CNTs structure and unhindered electron transfer rate (**Figure 3.8**C-E).

The superior HER catalytic activity, lower overpotential, and improved durability of NFS@CNTs could be attributed to several factors. The shift of the *d*-band center in the series from Ni@CNTs to NiFe@CNTs and finally to NFS@CNTs plays a crucial role in determining their hydrogen adsorption and desorption behavior and HER catalytic performance.[96, 97] As the *d*-band center transitions from the higher energy level of Ni to the intermediate level of NiFe alloy and then to the lower energy level of nickel iron sulfide (NFS), the hydrogen binding strength becomes more balanced. This balanced binding strength promotes the hydrogen adsorption and desorption processes, resulting in improved HER catalytic performance and related processes for NFS@CNTs compared to Ni@CNTs and NiFe@CNTs. Furthermore, the high surface-to-volume ratio of CNT sheets compared to metallic foam substrates is advantageous as it provides a larger number of catalytic active sites per unit volume. In addition, the strong interaction resulting from the increased contact area between NFS catalyst particles and CNT sheets can effectively alleviate catalyst detachment and agglomeration during the HER process.

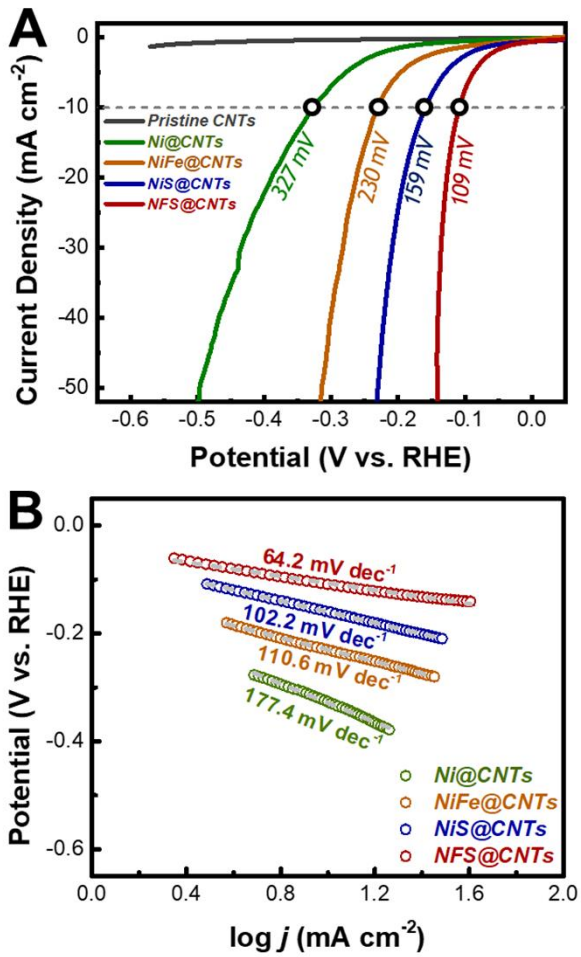


**Figure 3.6.** Electrochemical characterizations of Ni@CNTs, NiFe@CNTs, NiS@CNTs, NFS@CNTs: (A) the polarization curves of HER and (B) corresponding Tafel plots.

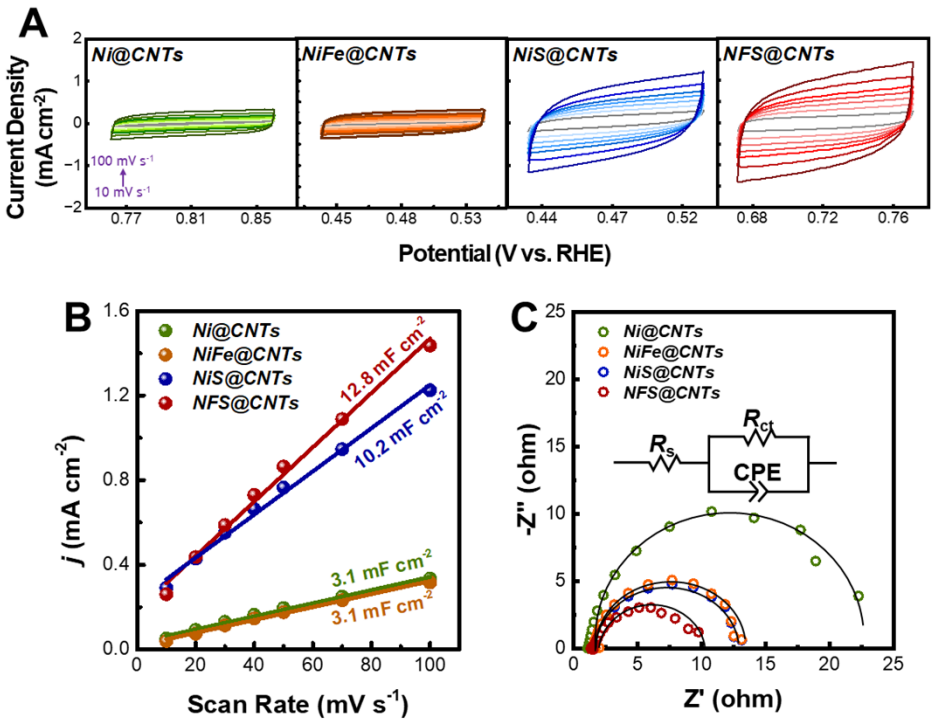


**Figure 3.7.** Electrochemical characterizations of Ni@CNTs, NiFe@CNTs, NiS@CNTs, NFS@CNTs: (A) CV curves within the potential range of ± 0.05 V vs. OCP and (B) variation of the double-layer charge currents. (C) Nyquist plots collected at the overpotential of 200 mV (the inset is the equivalent circuit).

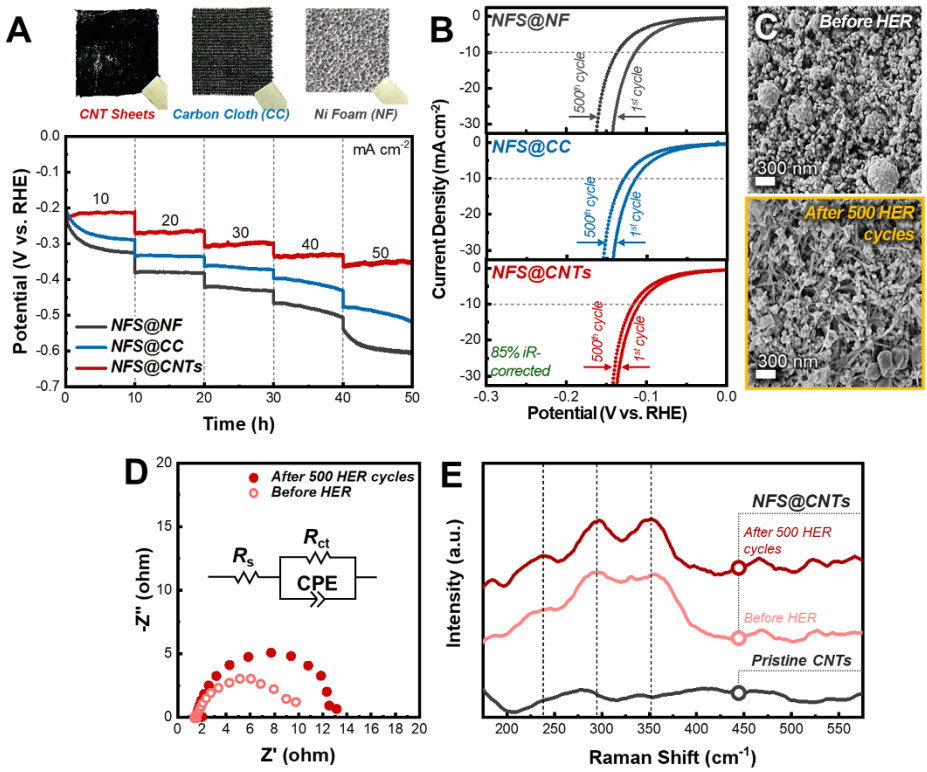


**Figure 3.8.** Demonstration of the superior durability of NFS@CNTs: (A) The multistep chronopotentiometry measurement of NFS@CNTs, NFS@CC, and NFS@NF with current densities of 10-50 mA cm$^{-2}$. (B) Polarization curves of three different electrodes at first and 500$^{th}$ HER cycles, (C) The surface FE-SEM images, (D) $R_{ct}$, and (E) Raman spectra of NFS@CNTs according to 500 HER cycles.

### 3.3.4. Optimizing layered NFS@CNTs for performance enhancement

A key advantage of FC-CVD-synthesized CNT sheets over conventional nickel foam-based catalyst electrodes is their ability to support high catalyst loading without significant increases in volume or weight, even when multiple electrode layers are applied. This unique feature is particularly important in the context of AEMWEs, where non-precious metal catalysts often require higher loading to achieve efficiencies comparable to their noble metal counterparts. Thus, achieving high catalyst loading while maintaining a thin and lightweight electrode structure is an essential requirement for efficient and practical AEMWE systems.

Given this requirement, the effect of modifying the electrode densities on the electrochemical performance of the FC-CVD-synthesized CNT sheets was investigated. **Figure 3.9**A and B illustrate the correlation between the electrode densities and the HER performance. As shown in **Figure 3.9**A, the HER polarization curves show an interesting trend over different electrode densities. Electrodes of 3.33, 6.67, 10.00, 13.33, and 16.67 g $cm^{-3}$ were evaluated, with the electrode of 10.00 g $cm^{-3}$ showing the best performance. The Tafel plot in **Figure 3.9**B provides additional insight into the HER kinetics of the different electrodes. This result is further corroborated by the volcano plot (**Figure 3.9**C), which shows the relationship between the electrode densities and the HER overpotential and Tafel slope. The HER performance peaks at the electrode of 10.00 g $cm^{-3}$ and decreases for both lower and higher densities. This trend can be understood by considering the balance between the catalyst loading and efficient mass transport within the electrode structure. While increasing the electrode densities allows for greater catalyst loading, there are physical limits to how much catalyst material can be loaded onto an electrode without negatively affecting other important processes, such as charge and mass

transport. Increasing the electrode density beyond the optimal point (~ 10.00 mg $cm^{-3}$) results in a denser CNT bundle network. This density can impede efficient ion transport and hinder access to the active sites, resulting in a decrease in overall performance.[98] Hence, the superior performance of the optimal electrode density of 10.00 g $cm^{-3}$ suggests that the optimized structure facilitates more efficient electrochemical reactions, thereby enabling lower overpotentials and higher reaction rates.

Taking these results together, it is clear that the unique properties of FC-CVD-synthesized CNT sheets, such as their thinness, high porosity, and ability to be stacked without a significant increase in thickness, not only allow for increased catalyst loading but also contribute to enhanced electrochemical performance. Therefore, this study demonstrates the potential of CNT sheets as novel electrode materials, surpassing the capabilities of traditional nickel foam electrodes in terms of catalyst loading, electrochemical performance, and mechanical stability.

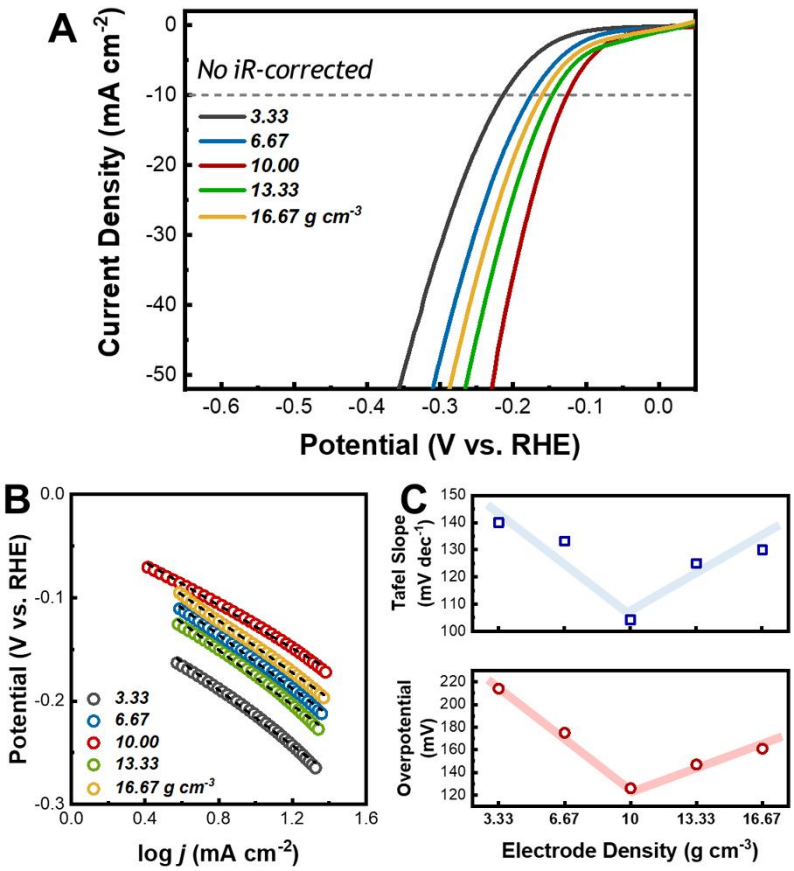


**Figure 3.9.** HER catalytic activity change according to the number of NFS@CNTs electrode layers: (A) polarization curves, (B) Tafel plot, and (C) overpotential and Tafel slope charge patterns by the electrode density (3.33 – 16.67 g $cm^{-3}$).

## 3.4. AEMWEs Single-Cell Configuration

Based on the findings of the electrode layer study, the optimally structured multilayer FC-CVD-synthesized CNT electrode was applied to a practical water electrolysis system to further substantiate the potential of this novel electrode material for real-world applications. The aim was to shed light on the capabilities of these uniquely structured electrodes in improving the efficiency and durability of an actual electrolysis device, thus bridging the gap between laboratory-based studies and practical industrial applicability.

In order to validate the applicability of the NFS@CNTs electrodes for a practical water splitting system, a prototype mini-scale AEMWE single-cell was configured with cobalt oxide ($Co_3O_4$). The single-cell was composed of a cathode for HER (NFS@CNTs), an anode for OER ($Co_3O_4$), an AEM, and a porous transport layer (PTL), as depicted in **Figure 3.10**A. The electrochemical properties of the cell were evaluated in a 1.0 M KOH alkaline electrolyte heated to 60 °C. As the operating temperature of the cell increases, performance can be improved by increasing ionic conductivity and mass transport, but thermal degradation of the AEM can also occur.[99] **Figure 3.10**B shows the polarization curve with different electrode densities (3.33, 10.00, and 16.67 g $cm^{-3}$) after cell activation of NFS@CNTs. The best performance was observed with 3-layers of NFS@CNTs, indicating the optimal electrode density for maximizing the electrochemical activity. This result is consistent with the trend observed at the half-cell level, confirming that the layer-stacking effect is also operative at the actual cell level.

Commercial AEM water electrolyzers typically operate within a constant current density range of about 400–500 mA $cm^{-2}$ to produce constant hydrogen.[100] Therefore, a long-term durability test at 500 mA $cm^{-2}$ was conducted to evaluate the

practical applicability. **Figure 3.10**C shows that NFS@CNTs stably maintained the cell voltage for 1000 hours, with a degradation rate of only 0.02 mV $h^{-1}$. The amount of hydrogen produced from the AEMWE cell was measured in real-time, and the energy efficiency of the cell was calculated using the following equation (3.1).:

$$\eta = \frac{E_{output}}{E_{input}} = \frac{V_{H_2} \times H_0}{W_h} \times 100 \qquad (3.1)$$

Where $V_{H2}$ is the volume of hydrogen gas ($m^3$), $H_0$ is the calorific value of hydrogen ($10.8 \times 10^6$ J $m^{-3}$, the lower heating value (LHV)), and $W_h$ is the electric power to produce hydrogen for an hour (P = V × I). In the AEMWEs cell, hydrogen was continuously produced at a rate of 19.42 mL $min^{-1}$ during the long-term durability test at a constant current density of 500 mA $cm^{-2}$. An increase in voltage due to cell degradation resulted in a decrease in hydrogen generation efficiency, but the system maintained a high hydrogen generation efficiency of approximately 75% for 1000 hours.

These results highlight the significant potential and applicability of the FC-CVD-synthesized CNT electrodes in practical water electrolysis systems. As demonstrated by the optimal electrode, the results show robust performance sustained over time and efficiency improvements. The consistently high hydrogen generation efficiency maintained throughout the 1000 hour test further reinforces the suitability of this electrode design for long-term use.

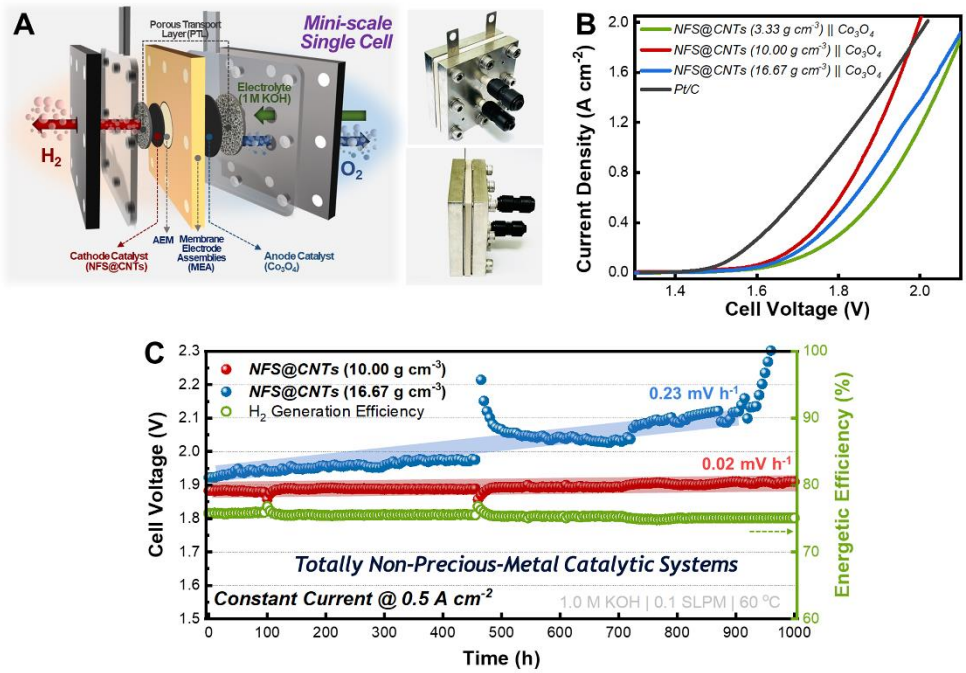


**Figure 3.10.** (A) The schematic of mini-scale AEMWE single-cell composed of NFS@CNTs (cathode for HER) and $Co_3O_4$ (anode for OER). (B) Polarization curves of the AEMWE cell in 1.0 M KOH at 60 ˚C. (C) Chronopotentiometry test for investigation of long-term durability of AEMWE cell at a current density of 0.5 A $cm^{-2}$ for 1000 h.

## 3.5. Summary

This study presents the design and synthesis of an electrocatalyst-integrated electrode for the HER, consisting of ultrafine nickel-iron sulfide particles supported on FC-CVD-synthesized CNT sheets (NFS@CNTs). This novel structure holds promise for efficient and sustainable hydrogen production in AEMWEs.

The FC-CVD method of deriving CNT sheets yields high surface-to-volume ratios, providing extensive active sites that facilitate electrochemical reactions. Their uniformity in the three-dimensional direction ensures consistent performance across the entire electrode, which is critical for industrial-scale applications. The CNT sheets also have interconnected electron pathways, promoting electron transport and improving the overall conductivity of electrode. Their large porosity supports easy access of reactant molecules to the active sites, enhancing mass transport during the catalytic process. Importantly, the FC-CVD method ensures the production of high-purity CNTs that support the NFS particles without introducing impurities that could lead to unwanted side reactions or degrade catalyst performance. The high purity and structural integrity of the FC-CVD-synthesized CNTs also enhance the durability of electrode, ensuring stable long-term operation even under harsh electrochemical conditions.

In conclusion, the integration of NFS particles with CNT sheets into the electrode structure addresses the challenges related to the low catalytic activity and durability of non-precious metal-based electrocatalysts. Furthermore, it opens new avenues for the design and fabrication of advanced electrode materials for clean energy technologies. This study provides a solid foundation for research to develop high-performance, durable electrocatalysts for the advancement of sustainable hydrogen production as well as other emerging clean energy applications.

# CHAPTER 4

# Understanding the Effect of Defects in CNT Assemblies for Applications as COR-Resistive Substrate in OER Environments

This study provides important insights into the electrochemical degradation of carbon-based electrodes during the oxygen evolution reaction (OER) - a critical aspect of electrocatalytic water splitting. The OER is hindered by high overpotentials and highly oxidizing conditions, which often induce carbon oxidation reactions (COR) and significantly affect the durability of carbon-based electrodes.

Therefore, the focus of this chapter has been to uncover the primary factors that contribute to COR during OER, thus addressing a significant gap in current understanding. One of the critical aspects of the investigation is to correlate the occurrence of COR with the type and amount of defects present in the CNTs. These defect characteristics could lead to accelerated COR, ultimately affecting the overall

durability of the electrode. The study proceeded by systematically observing the trends in COR and modulating the defects that critically influence it. Furthermore, the durability was improved by inhibiting these defects and subsequently incorporating actual OER catalysts to prove the effectiveness of the approach.

While the susceptibility of carbon to electrochemical oxidation under OER conditions has traditionally limited its application, it remains an economically competitive material for electrocatalyst support with demonstrated effectiveness in a water electrolyzer. Therefore, this study to improve the durability of the carbon anode during OER makes a significant contribution to the field of electrocatalytic water splitting. A comprehensive set of characterization techniques, including electron microscopy, Raman spectroscopy, and linear sweep voltammetry (LSV) was employed in this pursuit. This multifaceted approach paved the way for a deeper understanding of COR under OER conditions and serves as the foundation for future research aimed at mitigating the challenges associated with carbon-based electrodes in water electrolysis.

## 4.1. Introduction

The oxygen evolution reaction (OER) is a critical step in electrocatalytic water splitting due to its inherent high overpotential and highly oxidizing environment. The effective OER requires not only a catalyst with high activity, but also a support with robust stability. In this regard, carbon materials have emerged as an area of significant interest as potential catalyst supports due to their high electrical conductivity, large surface area, and wide range of structural and chemical properties. These unique properties offer the potential for more efficient dispersion and stabilization of the active phase of catalysts, which is crucial for OER efficacy. However, their use as electrocatalyst supports in an aqueous electrolyte presents challenges, primarily owing to the electrochemical oxidation of carbon. Thermodynamically, carbon can be oxidized to carbon dioxide (equation (4.1)) and carbon monoxide (equation (4.2)). (**Figure 4.1**):[101-103]

$$C + 2H_2O \rightarrow CO_2 + 4H^+ + 4e^-,\ E^0 = 0.207\ \text{V vs. SHE} \qquad (4.1)$$

$$C + H_2O \rightarrow CO + 2H^+ + 2e^-,\ E^0 = 0.518\ \text{V vs. SHE} \qquad (4.2)$$

While the kinetics of carbon oxidation is quite slow, allowing carbon to be used without serious problems,[104] this situation changes when the anodic potential reaches a threshold high enough for oxygen evolution above 1.23 V (vs. SHE). At this point, carbon oxidation can occur rapidly, a problem that is exacerbated in high surface area carbon, which is more susceptible to corrosion.[105] To address this issue, it is critical to identify the defects or specific sites on the CNTs where COR occurs.

Once these defects are identified, tailored strategies can be implemented to minimize or even eliminate them, thereby significantly reducing the incidence of COR and improving the durability of carbon-supported OER catalysts. However, the precise control and understanding of defects, especially in terms of their properties and distribution in the carbon material, is a challenging task.[106]

Unlike other existing CNT synthesis methods, the floating catalyst chemical vapor deposition (FC-CVD) process offers the unique advantage that the amount and distribution of defects in the resulting CNTs can be finely controlled by tuning the synthesis parameters.[107, 108] By controlling the key process variables that affect the formation and distribution of defects, it becomes possible to produce CNTs under different conditions, each characterized by different defect properties. This suggests that it is a promising way to achieve the goal of characterizing defects in carbon to provide a way to understand and address the phenomenon.

The purpose of this study is to investigate the relationship between the defect properties of CNTs synthesized by the FC-CVD process and their susceptibility to COR. A deeper understanding of this relationship could lead to strategies for minimizing defect-induced COR, thereby revealing the potential of carbon materials as durable supports for OER catalysts. The results of this study are expected to provide a strong foundation for the rational design and optimization of carbon-based catalyst supports, bringing us a step closer to efficient electrocatalytic water splitting.

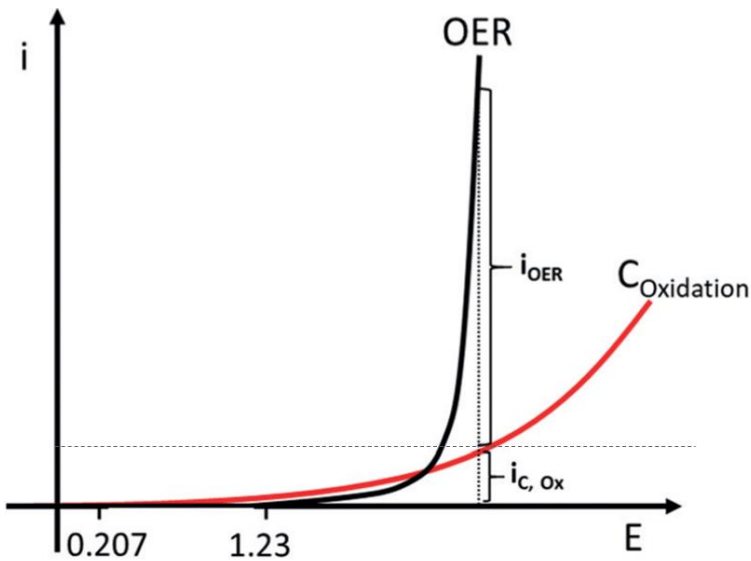


**Figure 4.1.** Carbon oxidation reaction and relevant current evaluation ($i_{C,Ox}$) along with the OER ($i_{OER}$) of carbon-supported catalyst.[102]

## 4.2. Experimental Methods

### 4.2.1. Sample preparation

In order to control the defect of CNT assemblies, the input amount of carrier gas ($H_2$) and precursor solution were adjusted, which are variables in the CVD process that affect the shape and content of the defect.[109-112] The CNT assemblies obtained for each synthesis condition were conducted for structural analysis to confirm the surface morphology, defect type and distribution and electrochemical analysis to evaluate the carbon oxidation behavior (additional post-processing for analysis was not performed). The synthesis temperature and precursor solution, which are other process variables, were kept constant to investigate the correlation of defect and carbon oxidation according to the injected amount of carrier gas and precursor.

### 4.2.2. Material characterization

The surface morphologies of the fabricated CNT assemblies are observed under a field emission-scanning electron microscopy (FE–SEM; MERLIN Compact, ZEISS, Germany) at an acceleration voltage of 2 kV. The XPS analysis was performed on sputter-cleaned surfaces using a K-Alpha+ instrument (Thermo Fisher Scientific, USA) equipped with a monochromatic Al Kα X-ray source (1486.6 eV). The XRD analysis was performed on a D8 Advance (Bruker, USA) with a Cu Kα radiation wavelength of 1.542 Å. To investigate the defect-types and their amounts on synthesized CNT assemblies, the Raman analysis was carried out using a DXR2xi Raman microscope (Thermo Fisher Scientific, USA) with a laser wavelength of 532 nm.

### 4.2.3. Electrochemical characterization

All electrochemical performances were evaluated with a multichannel potentiostat (VMP3, BioLogic Science Instruments, France) at room temperature. A three-electrode cell was consisted of a working electrode (prepared electrodes in this work), reference electrode (Hg/HgO), and counter electrode (graphite rod). The working electrode was prepared by cutting it into a circle with a diameter of 13 mm and mounting it on a holder for observing corrosion. To characterized electrochemical performances, cyclic voltammetry was carried out in 1.0 M KOH electrolyte solution and their electrochemical oxidation stability was determined from the oxidation behavior at a high anodic potential. To validate the effect on durability as an OER catalyst electrode, defect-controlled CNT assemblies substrates and commercial substrates (Ni foam, carbon paper, and carbon cloth) were prepared in the same manner as the nickel-iron sulfide (NFS) synthesis in Chapter 3. The effect of cycling the OER reaction was evaluated by 50 repetitions of cyclic voltammetry in the range of 1.15 - 1.85 V vs. RHE. A comparison of the durability of the substrates was performed by applying a constant current of 100 mA $cm^{-2}$ for 100 hours.

## 4.3. Preliminary Investigations and Motivation

### 4.3.1. Investigation of the effect of carbon crystallinity on COR

The phenomenon of COR under OER environments has attracted considerable scientific interest and prompted rigorous investigations.[113-116] As a fundamental challenge in the field, this study embarked on in-depth analysis to understand the underlying mechanisms and factors influencing this phenomenon. The primary motivation stems from previous studies suggesting the potential of carbon crystallinity to mitigate COR.[117-119] An investigation was conducted on four types of carbon-based conductive additives, namely commercially available carbon blacks (Denka black, Vulcan black, and Ketjen black) and graphite, which is known for its exceptional crystallinity.

To ensure accurate and representative results, electrodes were constructed using only carbon. This approach effectively isolated the role of carbon in the system and provided an undiluted perspective on its intrinsic reactivity under OER conditions. Durability tests included the application of a constant current until degradation was initiated, providing a clear reference for comparison. The results showed that while Vulcan and Ketjen blacks degraded rapidly within 10 hours, Denka Black and graphite showed significantly longer life (**Figure 4.2**). These differences in COR resistance between identical carbon materials prompted further investigation. A reasonable hypothesis was that these differences could be related to variations in the crystallinity of the carbon materials. Raman spectroscopy, a powerful analytical tool for determining the crystallinity of carbon materials by evaluating the G:D intensity ratio, was used to evaluate this hypothesis. As shown in **Figure 4.3**A, the G:D ratios of the carbon blacks, excluding graphite, were relatively consistent, ranging from 0.8

to 1.0 (these values were based on multiple measurements of ten times for each sample to ensure the reliability of the results and minimize potential errors). According to previous research, the nature and distribution of defects in carbon materials can be identified by fractionating their Raman spectra into different sub-peaks.[120, 121] **Figure 4.3**B shows the results of fitting the recorded Raman spectra into five sub-peaks, defined as $D^*$, D, $D^{**}$, G, and D'. A notable observation was that Vulcan black and Ketjen black, which exhibit relatively lower stability under constant current in **Figure 4.2**, have a higher proportion of $D^*$ and $D^{**}$ peaks compared to Denka black and graphite. This suggests that specific defects may act as critical factors in the induction of COR, implying that elucidating the importance of uncovering the correlation between defects in carbon and COR to expand the potential utility of carbon-based conductive additives and substrate materials in an OER environment.

In summary, the key finding from these results is that a high G:D ratio does not necessarily mean that a carbon material is resistant to COR. Durability tests revealed significant differences in the degradation tendencies of carbon-based conductive additives, even those with similar G:D ratios. This indicates that using the G:D ratio as the sole descriptor for predicting the corrosion resistance in carbon materials, particularly where crystalline and amorphous phases coexist, may be an oversimplification. Therefore, this study highlights the need for a more comprehensive approach to evaluating the corrosion resistance of carbon materials rather than relying solely on the G:D ratio. Such a comprehensive method is expected to contribute significantly to the understanding of COR and pave the way for the development of more reliable predictors of the durability of carbon-based conductive additives.

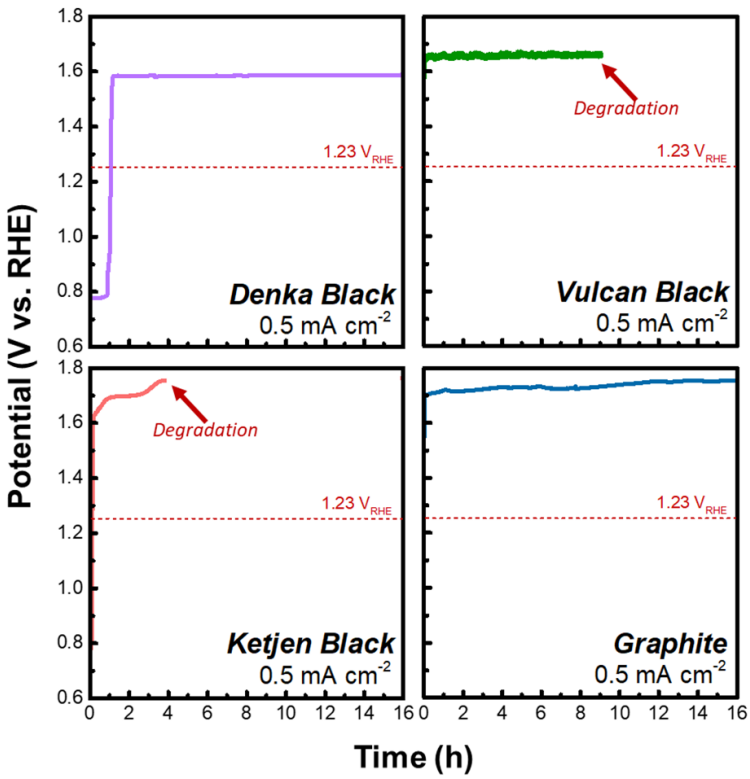


**Figure 4.2.** The analysis of the COR behavior in an OER environment of four commercial carbon materials (Denka black, Vulcan black, Ketjen black, and graphite). The evaluation was performed by applying a constant current density of 0.5 mA $cm^{-2}$.

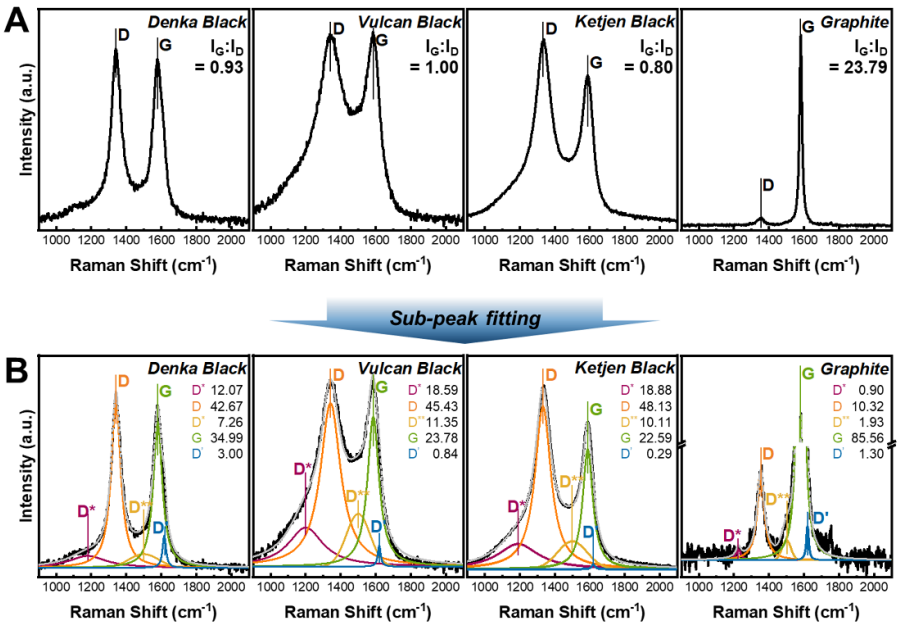


**Figure 4.3.** Raman spectra of four commercial carbon materials (Denka black, Vulcan black, Ketjen black, and graphite): (A) the measured spectra and (B) the sub-peak fitted spectra.

### 4.3.2. Understanding the role of synthesis parameters in controlling defects in CNT assemblies

In the context of characterizing the effects of defects, the FC-CVD method is presented as one of the promising synthesis techniques that can precisely tune the defect density and distribution of CNT assemblies. From the resulting products with different defect densities and distributions, the carbon oxidation resistance can be investigated and ultimately the defects that mainly contribute to the COR can be identified. In the FC-CVD process, several parameters can affect the properties of the resulting CNTs, including the composition and injection rate of the CNT precursor, the flow rate of the injected gas, and the synthesis temperature. Since the primary objective of this study is to identify specific defects, the focus is on changing the precursor injection rate and the carrier gas flow rate, while maintaining the precursor composition and temperature conditions based on experimentally validated synthesis conditions. A detailed consideration of the hydrogen gas flow rate, often used as a carrier gas in the FC-CVD process, is particularly intriguing in this context. The hydrogen gas provides a reducing atmosphere, which is vital for preventing catalyst oxidation, thereby preserving its activity over extended periods. In addition, the flow rate of this hydrogen gas can have a significant effect on the synthesized carbon. Specifically, a higher hydrogen flow rate can enhance the removal of amorphous carbon, a byproduct of CNT growth, resulting in CNTs with fewer defects and improved crystallinity.[122] However, too high a flow rate may disrupt the stability of the gas phase reactions and lead to a lower yield of CNTs. Conversely, a lower hydrogen flow rate may result in a higher concentration of amorphous carbon, leading to an increase in defects within the CNTs. Similarly, the injection rate of the carbon precursor also significantly controls the defect

characteristics of the CNTs. A slower injection speed promotes more complete precursor decomposition and more ordered CNT growth, resulting in fewer defects and higher crystallinity. On the other hand, a faster injection speed can lead to incomplete precursor decomposition, resulting in an increase in defects and a decrease in crystallinity.[123, 124]

To substantiate the above theoretical hypothesis, the gas flow rate was varied from 1200 to 2000 sccm under three different precursor injection conditions and all synthesized CNTs were analyzed by Raman spectroscopy (**Figure 4.4**). The observed trend showed that the G:D ratio typically increased (a), peaked (b), and then decreased (c) with increasing gas flow rate, with the specific response varying according to the precursor injection rate. This trend can be attributed to the dual role of hydrogen atoms during the synthesis of CNTs. On one hand, hydrogen atoms can etch the amorphous carbon on the CNT surface, leading to an enhancement in crystallinity. On the other hand, beyond a certain threshold, the etching effect of hydrogen can extend to the CNT surface itself, resulting in a decrease in crystallinity. This finding underscores the importance of fine-tuning the hydrogen gas flow rate during the FC-CVD process to optimize the crystallinity and, consequently, the carbon oxidation resistance of CNTs.

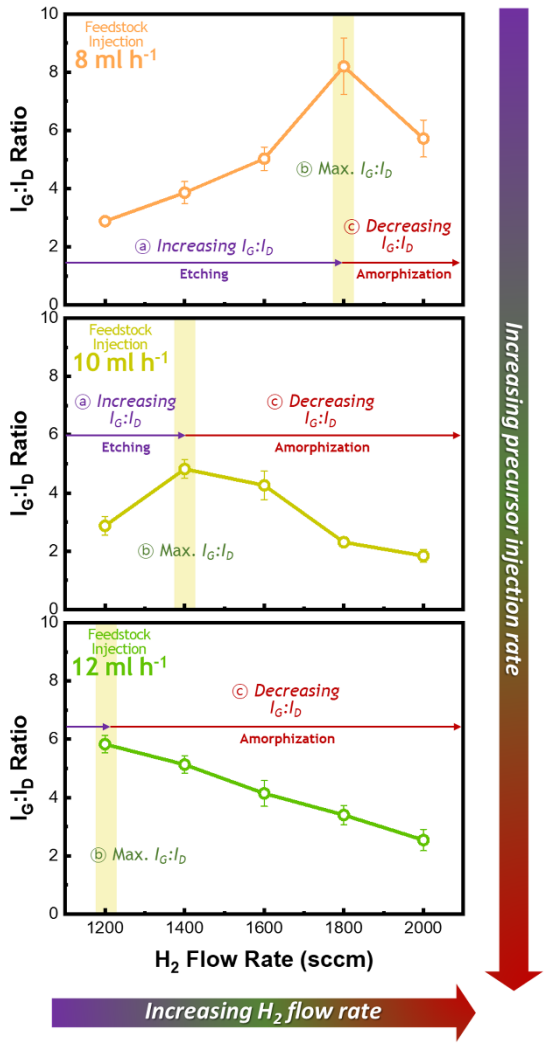


**Figure 4.4.** Evaluation of carbon crystallinity change trends according to $H_2$ flow rate and precursor injection rate control in the synthesis process.

## 4.4. Elucidation of the Relationship between Defects and COR in CNT Assemblies

### 4.4.1. Evaluation of COR by theoretical analysis

In order to observe and predict the COR behavior of CNTs synthesized under different conditions, cyclic voltammetry (CV) was performed using a three-electrode cell configuration with CNTs as the working electrode. Theoretically, the COR coincides with the OER in the potential range. Thus, the measured current above 1.23 V is a mixture of charges resulting from the COR, the OER, and the electric double-layer (EDL) capacitance induced by the electrostatic adsorption of ions on the electrode surface. Distinguishing the charges generated by each of these factors based solely on the evaluation results can be challenging. To address this challenge, theoretical equations are used to calculate the charges caused by the EDL ($Q_{EDL}$) and the OER ($Q_{OER}$).[125] The calculated charges were then subtracted from the total measured charge ($Q_{total}$) to predict the remaining charge resulting from COR. This approach allows one to infer the relationship between the defects and the observed COR behavior in the synthesized CNTs. The method of mathematical derivation of each charge was performed in the following order.

i) For the EDL capacitance ($Q_{EDL}$):

$$Q_{EDL} = F_{EDL} \times (V - \mathrm{OCP})$$

$$F_{EDL} = \int i_{EDL} dV / (2 \times v \times \Delta V)$$

ii) For the oxygen evolution reaction ($Q_{OER}$):

$$Q_{OER} = \int i_{OER}\, dV$$

$$\ln(i_{OER}) = \ln(i_0) + ((1 - \alpha)nF / 2.3\ RT)\ \eta_{OER}$$

iii) For the carbon oxidation reaction ($Q_{COR}$):

$$Q_{COR} = Q_{total} - Q_{EDL} - Q_{OER}$$

Where OCP is the open circuit potential (V), $v$ is the scan rate (mV $s^{-1}$), and $\Delta V$ is the potential window (V) during the CV measurement. When evaluating the $Q_{COR}$, it is calculated indirectly by subtracting the charges attributed to the electric double-layer capacitance ($Q_{EDL}$) and the oxygen evolution reaction ($Q_{OER}$) from the total measured charge ($Q_{total}$). This methodology allows for the separation of the effects of carbon oxidation on the current response and provides insight into the behavior of COR in CNTs under different conditions.

For the theoretical calculations, several parameters are used in the $Q_{OER}$ equation, which refers to the Butler-Volmer kinetics of OER: $i_0$ is the exchange current density (A $cm^{-2}$), $\alpha$ is the charge transfer coefficient, $n$ is the number of electrons involved in the rate-determining step, $F$ is the Faraday constant (C $mol^{-1}$), $R$ is the gas constant (J·(mol·K)$^{-1}$), $T$ is the absolute temperature (K), and $\eta_{OER}$ is the overpotential for OER (V).[126] Incorporation of these parameters allows effective modeling and interpretation of the current-potential behavior during OER, providing a comprehensive understanding of the electrochemical processes at play.

### 4.4.2. In-depth analysis of the correlation between COR and defect distribution

The optimal conditions for the stable synthesis of CNTs have been determined to involve a precursor injection rate of 6, 8, 10, 12, and 14ml $h^{-1}$, respectively. However, given that the application requires an OER catalyst support that is electrochemically stable and uniform conductivity, CNTs synthesized at 6 and 14 ml $h^{-1}$ were excluded from the evaluation. This exclusion was due to the excessive presence of unreacted catalyst impurities causing side reactions and loss of mechanical strength, as shown in the surface SEM images in **Figure 4.5**.

Therefore, in order to gain a deeper understanding of the correlation between COR and defect distribution in CNTs, this investigation focuses on CNTs synthesized at precursor injection rates of 8 and 10 ml $h^{-1}$ and carrier gas flow rates ranging from 1200 to 2000 sccm. The results of separating the measured polarization curve into each constituent charge, based on the theoretical formulas described in section 4.4.2, are shown in **Figure 4.6**A (8 ml $h^{-1}$) and **4.7**A (10 ml $h^{-1}$), respectively. First, the COR charge of five types of CNTs synthesized under different gas flow rates at a precursor injection volume of 8 ml $h^{-1}$ was measured, and noticeable differences in the charge separation distribution were observed (**Figure 4.6**A). The Raman sub-peak fitted spectra, which examined the defect distribution in CNTs, also showed significant differences among CNTs, suggesting that the gas flow rate can directly affect the crystallinity of CNTs (**Figure 4.6**B). Similarly, after deriving the polarization curves and calculating the COR charge for the five types of CNTs synthesized at a precursor injection rate of 10 ml $h^{-1}$ (**Figure 4.7**A), sub-peak fitting of Raman spectra was performed in the same way (**Figure 4.7**B). In the Raman spectra of carbon materials, the five-peak model fits the D, $D^*$, $D^{**}$, D' and G peaks by using Gaussian, Lorentzian, or pseudo-Voigt functions, which is yield the best $\chi^2$

values.[127, 128] In addition, the relative area ratio between sub-peaks serves as an indicator providing more specific insights into the structural properties and qualities of the carbon material. The areal ratio compares the areas under these peaks and takes into account both the height and width of the peak. Thus, the areal ratio is more sensitive to the actual amount of each vibrational mode present in the sample and provides a more comprehensive view of the carbon structure. It provides a more accurate representation of the degree of graphitization, disorder, and types of defects present.[129, 130]

Consequently, considering all of the above analytical results and comparing the patterns of change between COR and each parameter as shown in **Figure 4.8**, the following can be concluded and a correlation between COR and defect shape and distribution can be expected.

i) It is difficult to establish a precise correlation between $I_G$:$I_D$ ratio and COR incidence. There appears to be no specific correlation between the ratio of the intensities of the G-band to D-band (representing the crystallinity of carbon in the Raman spectrum) and COR incidence.

ii) The $D^*$ peak, signifying surface defects, also demonstrated an unrelated change pattern with the variation in COR charge.

iii) Though the $D^{**}$ peak, indicating amorphous carbon, was present in the smallest quantities among the sub-peaks, it displayed a changing pattern similar to the variation in COR incidence.

**iv)** The D' peak, representing edge or boundary defects, was also observed to follow a similar trend with increasing or decreasing COR charge as the

peak's content changed.

In order to statistically validate these hypotheses, the investigated correlation between the COR charge and defect type/quantity is plotted for several CNT samples, including commercial products. As shown in **Figure 4.9**A, there is no linear relationship between G:D ratio, a general measure of carbon crystallinity, and COR charge. This limitation highlights the inadequacy of the G:D ratio as a predictive factor for the amount of COR. On the other hand, a clear linear correlation is observed between the COR charge and specific defect types ($D^{**}$ and $D^{'}$), as shown in **Figure 4.9**B-E. This observation implies that the identification and minimization of these specific defects could make the materials suitable for durable carbon-based OER catalysts and substrates. Such findings support the argument made in section 4.3, and underscore the importance of understanding the nature of defects in carbon materials when they are used as conductive substrates or supports for OER catalyst electrodes. Thus, these results reinforce the need for a detailed study of defects in carbon materials and suggest that a comprehensive approach could significantly improve the performance and lifetime of carbon-based electrochemical devices.

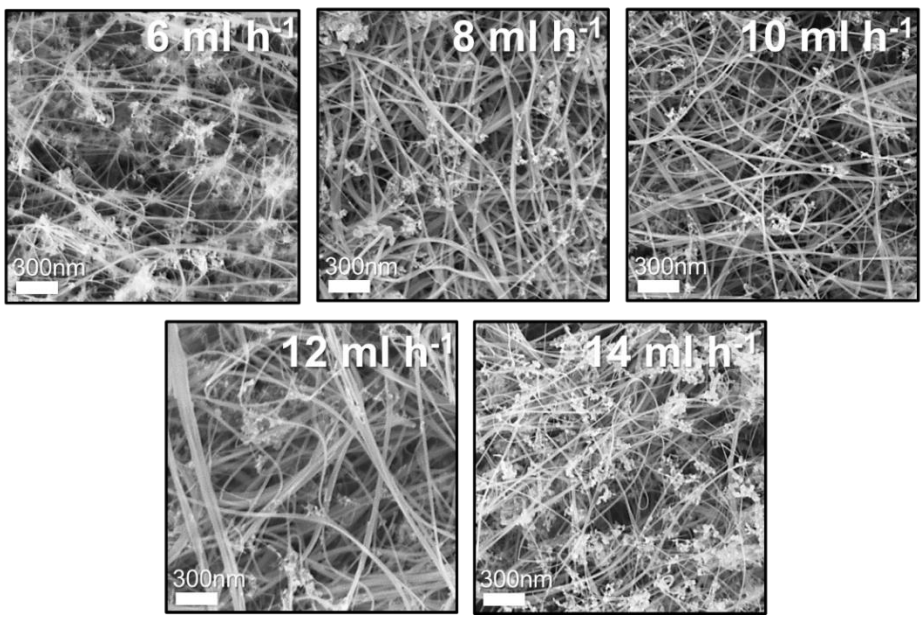


**Figure 4.5.** FE-SEM images of surface morphology of CNTs fabricated under synthesis conditions with different precursor injections (6, 8, 10, 12, and 14 ml $h^{-1}$).

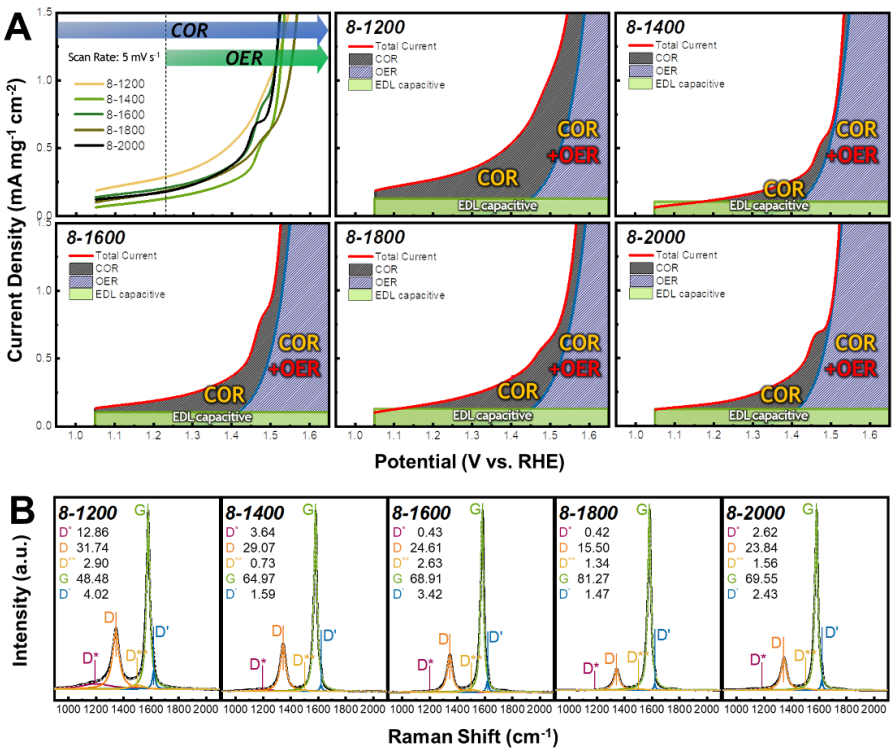


**Figure 4.6.** Analysis of the evolution of COR behavior and surface defect distribution with a precursor injection rate of 8 ml $h^{-1}$ and carrier gas flow rate of 1200-2000 sccm: (A) Polarization curves showing the respective contributions based on theoretical COR, OER, and EDL charge calculations and (B) defect distribution analysis by the sub-peak fitting of Raman spectra.

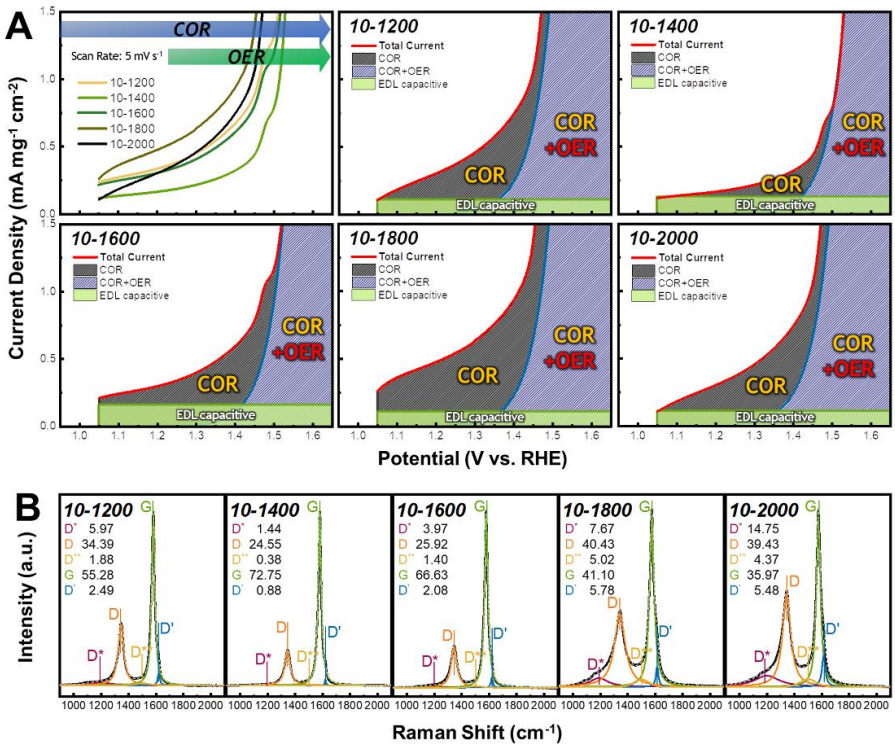


**Figure 4.7.** Analysis of the evolution of COR behavior and surface defect distribution with a precursor injection rate of 10 ml $h^{-1}$ and carrier gas flow rate of 1200 - 2000 sccm: (A) Polarization curves showing the respective contributions based on theoretical COR, OER, and EDL charge calculations and (B) defect distribution analysis by the sub-peak fitting of Raman spectra.

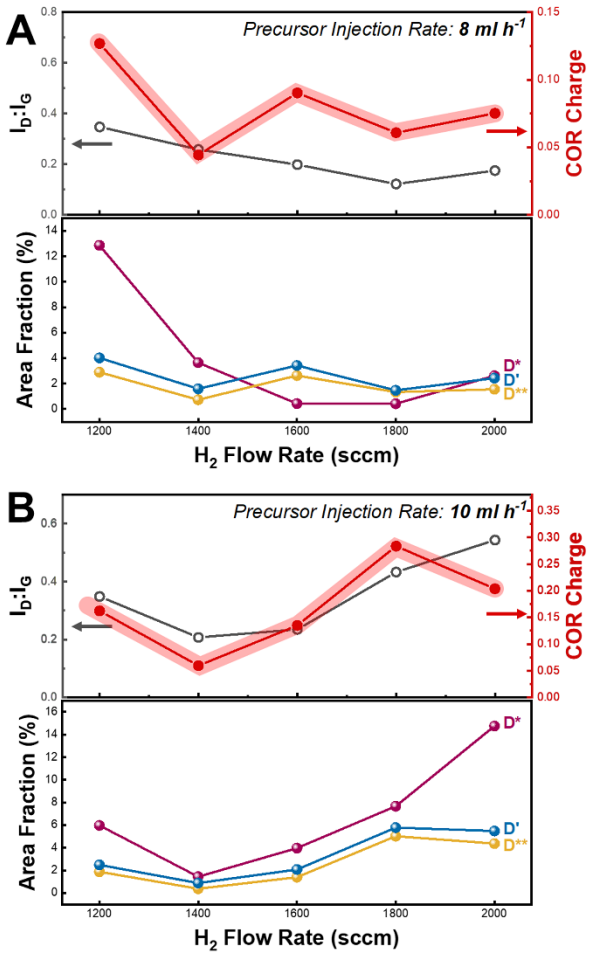


**Figure 4.8.** Correlation between $I_D$:$I_G$ ratio and area fraction of sub-peaks ($D^*$, $D^{**}$, and D') representing specific defect and COR charge by synthesis conditions (precursor injection rate: (A) 8 ml $h^{-1}$ and (B) 10 ml $h^{-1}$).

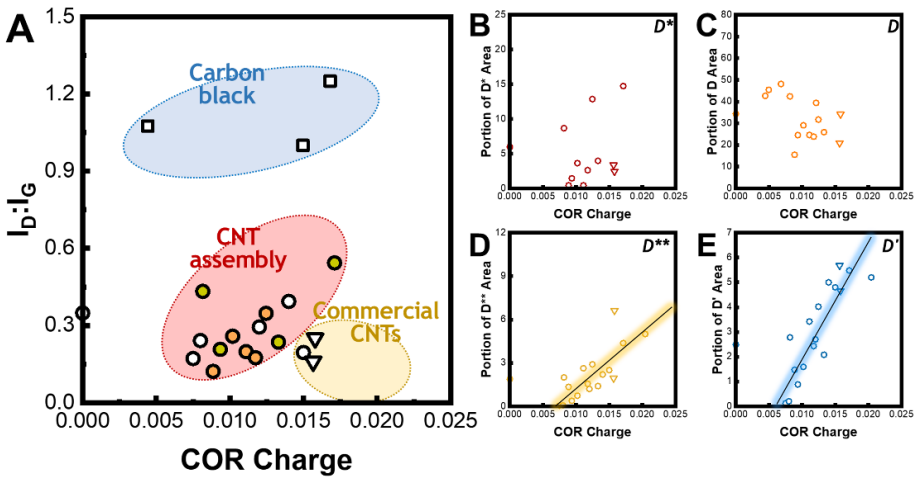


**Figure 4.9.** (A) A plot expressing the relationship between COR charge and Raman crystallinity ($I_D$:$I_G$ ratio) of various carbon materials including commercially available conductive materials. (B) The correlation between the portion of the specific defect and COR charge by obtained investigation of Raman sub-spectra fitting.

## 4.5. Validation of COR Reduction through Defect Mitigation

The hypothesis presented in the previous section, concerning the correlation between the concentration of $D^{**}$ and D' defects and the prevalence of COR, led us to establish an experimental protocol to validate this proposition. The purpose of this protocol is to validate this hypothesis through a defunctionalization process specifically aimed at minimizing surface oxygen functional groups, known as potential sites for corrosive reactions. This defunctionalization is achieved through a thermal treatment process that effectively promotes the desorption of chemisorbed oxygen, thereby eliminating many surface oxygen functional groups.[131, 132]

The effects of thermal defunctionalization were evaluated by surface SEM analysis. In order to clarify the effect of suppression of $D^{**}$ and D', two different synthesized CNTs were selected: one characterized by the fewest defects (10-1400) and the other by the most defects (10-1800). Prior to thermal treatment, extensive amounts of amorphous and unreacted catalyst impurities were visible on the surfaces of both samples, as shown in **Figure 4.10**A and B. Thermal treatment effectively eliminated the majority of these residues (**Figure 4.10**C and D). The influence of thermal defunctionalization was also clearly evident in the TGA performed in an air atmosphere. According to the TGA results obtained (**Figure 4.10**E), after the CNTs were completely burned at about 600 °C, there was a significant decrease in the amount of residual impurities. This reduction in impurities was consistent with the observations from the SEM analysis and supported the conclusion that thermal defunctionalization effectively eliminates amorphous and unreacted catalyst residues. Taken together, these results confirm the efficacy of thermal defunctionalization in refining the quality of synthesized CNTs, further strengthening its potential for improving the performance of CNT-based electrochemical systems.

Subsequently, the changes observed in the Raman spectra and polarization curves after defunctionalization provide a clear indication of the effectiveness of this treatment. **Figure 4.11**A shows sub-peak fitted Raman spectra from 10-1400 (the lower $D^{**}$ region) and 10-1800 (the higher $D^{**}$ region) after defunctionalization to examine the effect of eliminating surface oxygen functional groups and amorphous carbon. In both cases, a significant decrease in the area under the $D^{**}$ peak was observed after defunctionalization, indicating a successful reduction in defect sites. This reduction was further corroborated by changes in the polarization curves, which showed a decreasing current trend, inherently indicating reduced COR activity. Another interesting observation is that a sub-peak related to the carbonate ion ($CO_3^{2-}$) was identified when COR occurred in an alkaline environment. This was attributed to the interaction between $CO_2$ produced by the COR of the carbon material and $OH^-$ ions in the electrolyte. The reaction equations associated with $CO_2$ and $OH^-$ ions are as follows:[133, 134]

$$CO_2(g) + OH^- \rightarrow HCO_3^- \qquad (4.3)$$

$$HCO_3^- + OH^- \rightarrow CO_3^{2-} + H_2O \qquad (4.4)$$

$$CO_2(g) + 2OH^- \rightarrow CO_3^{2-} + H_2O \qquad \text{Overall reaction ((4.3) + (4.4))}$$

Notably, both types of defunctionalized CNTs (10-1400-D and 10-1800-D) showed negligible carbonate-related sub-peak in their Raman spectra after COR (**Figure 4.12**). This result suggests a reduction in $CO_2$ production by COR, and finally, these experimental results provide analytical support for our hypothesis in the previous section. The successful mitigation of COR, particularly through the reduction of $D^{**}$ defects, highlights the importance of understanding and managing

defects in carbon materials for electrochemical applications. This significant finding challenges the conventional focus on general crystallinity and instead advocates an emphasis on specific defects, which has proven to be a more predictive and actionable parameter.

In the final step of this investigation, the practical implementation of defect-minimized CNT assemblies as durable carbon-based supports for OER catalysts is evaluated based on the previously identified correlation between CNT defects and COR. By selectively minimizing certain defects, the occurrence of COR was significantly reduced. The implementation of CNTs as robust carbon-based supports for OER catalysts was evaluated by forming nickel-iron sulfide (NFS), previously used as a hydrogen evolution reaction (HER) catalyst (chapter 3), on four different CNT supports with different defect distributions. The OER polarization curves for electrodes containing NFS on four different CNTs (10-1400, 10-1800, 10-1400-D, and 10-1800-D) with different amounts of COR-inducing defects were studied in an aqueous 1.0 M KOH electrolyte environment, as shown in **Figure 4.13**A-D. After 50 reaction cycles, a decrease in OER activity was observed in all samples, but the magnitude of this decrease varied significantly among the samples. In particular, 10-1800, which was characterized by an excess of COR-inducing defects, showed a dramatic decrease in catalyst activity, whereas 10-1400-D, in which defects were suppressed, showed a negligible decrease in performance. The durability of the electrodes under harsh OER conditions was further evaluated by comparing the potential change behavior of the four electrodes at a constant current density of 100 mA $cm^{-2}$. Even under high current density, 10-1400-D, which is virtually free of COR-inducing defects, not only maintained its potential stability but also retained its initial performance after 100 hours. In contrast, 10-1800 exhibited a steady increase in potential from the start and suffered severe destruction of surface

morphology, as confirmed by comparing SEM images before and after the reaction. These results underscore the importance of controlling defect distribution in carbon supports for OER catalysts and demonstrate that careful management of defect content can significantly improve the durability and long-term operational stability of catalysts der demanding reaction conditions.

In summary, the evidence underscores the critical role of controlling defect contribution in CNT supports in maintaining their stability as OER catalyst supports. The superior stability of 10-1400-D under challenging OER conditions highlights the importance of minimizing defects that induce CORs, and confirms the practical feasibility of implementing defect-controlled CNT assemblies as durable OER catalyst supports. These findings are applicable to the broader field of catalysis, underscoring the need for careful control of catalyst support structures to maximize performance and durability.

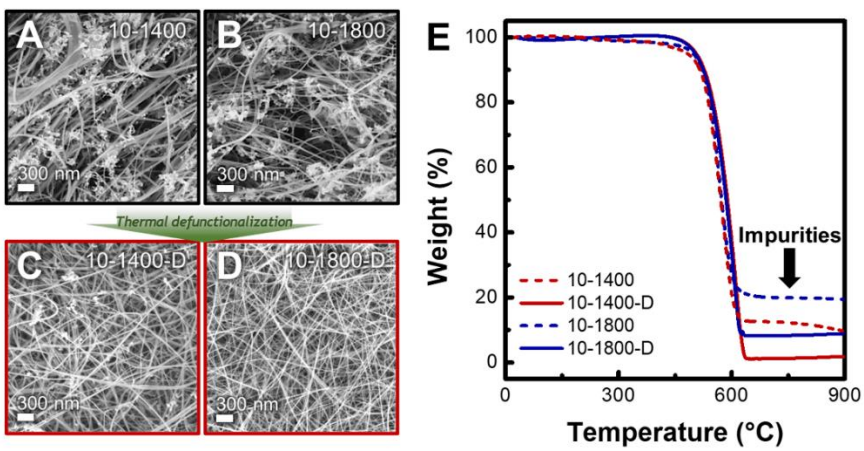


**Figure 4.10.** Validation of the effectiveness of thermal defunctionalization: (A-D) surface morphologies of before (A, B) and after (C, D) treatment of two types of CNT assemblies (10-1400 and 10-1800) and (E) TGA curves.

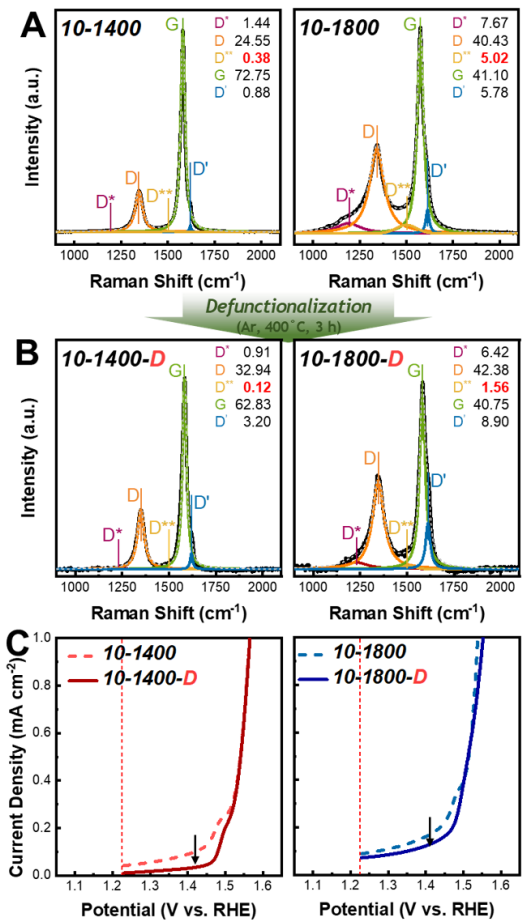


**Figure 4.11.** Changes in Raman spectra and defect distributions of CNT assemblies after defunctionalization: (A) Before and (B) after defunctionalization. (C) Polarization curves

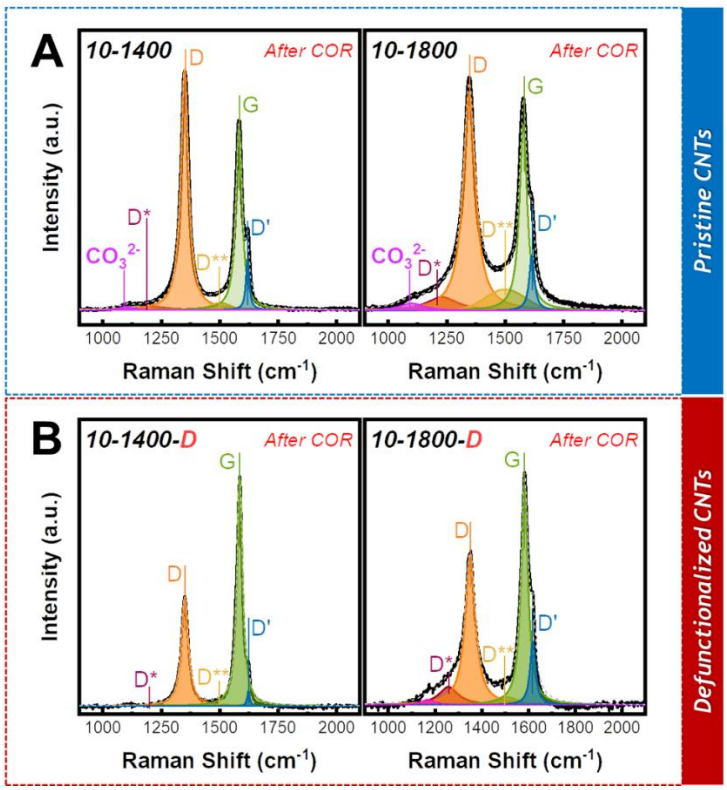


**Figure 4.12.** The defect distribution change after COR by the defunctionalization of CNTs: (A) pristine CNTs (10-1400 and 10-1800), (B) defunctionalized CNTs (10-1400-D and 10-1800-D).

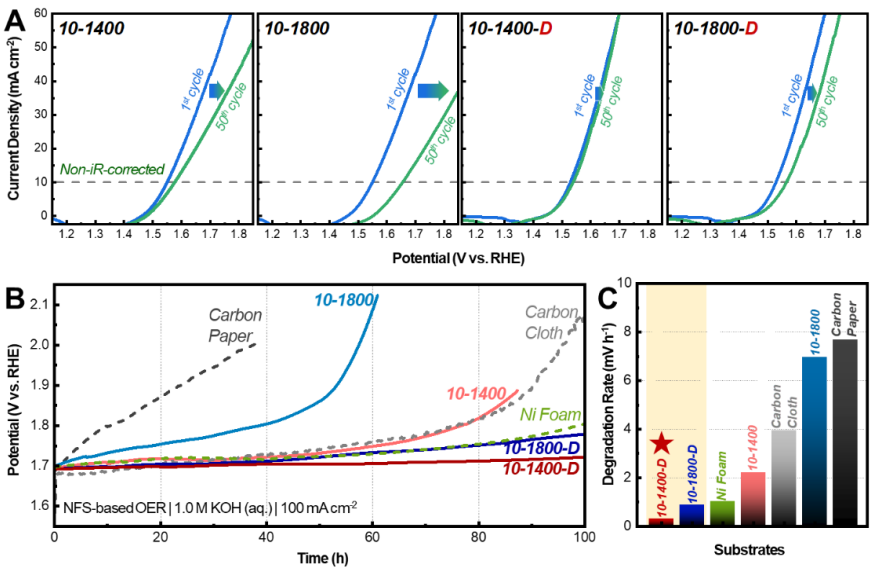


**Figure 4.13.** Comparison of durability change behavior after OER catalyst introduction on four CNT supports (10-1400, 10-1800, 10-1400-D, and 10-1800-D) with different defect amounts and distributions: (A) polarization curve change after 50 OER cycles, (B) durability behavior under constant current of 100 mA $cm^{-2}$, and (C) degradation rate according to substrates.

## 4.6. Summary

This study sought to address an important issue related to the electrochemical oxidation of carbon during OER by identifying the correlation between COR and specific defect characteristics within CNTs. By taking advantage of the versatility of FC-CVD synthesis methods, a wide variety of CNTs were prepared, each with a distinct defect profile and the type and distribution of defects were systematically investigated. As a result, the comprehensive analysis including microstructure and electrochemical behavior revealed a clear relationship between specific defects and the prevalence of COR. Using the knowledge gained from this phase, strategies were developed to minimize these specific defect types, thereby suggesting an approach to creating highly durable OER catalyst supports. The investigation demonstrated a clear relationship between the parameters of the FC-CVD process, the resulting defect characteristics of the CNTs and their resistance to COR. The comprehensive approach taken in this research revealed that specific defects in carbon materials can significantly affect their performance and durability under OER conditions. Furthermore, the results suggest that by managing these defects, significant improvements in the durability of carbon-based catalyst supports can be achieved.

Ultimately, this study not only advances the understanding of the relationship between carbon defects and COR, but also suggests a practical methodology to enhance the performance and durability of carbon-based materials in OER and other potential electrochemical applications. The results highlight the importance of a thorough understanding of carbon defects for the design and optimization of carbon-based electrochemical systems, and provide a solid platform for future research in this area.

# CHAPTER 5
# Conclusion and Outlook

## 5.1. Summary of Thesis Objectives and Achievements

The primary objective of this thesis was to evaluate and highlight the potential of carbon nanotubes (CNTs) synthesized *via* the floating catalyst chemical vapor deposition (FC-CVD) process with a focus on energy storage and conversion applications. Despite the well-recognized superior physicochemical properties of CNTs, their commercial applications have yet to be realized. Therefore, this thesis proposes solutions that fully exploit the unique material, structural, and process advantages of FC-CVD-synthesized CNTs to overcome barriers to commercialization. This effort is intended to promote the practical application of these materials and shed light on the pivotal role of CNTs in energy storage and conversion technologies. The investigations and accomplishments toward these goals are detailed in the following three chapters:

- ***Chapter 2*** focused on investigating the applicability of FC-CVD-synthesized CNT assemblies as an alternative to conventional current collectors in batteries and supercapacitors. Experimental investigations revealed their superior performance and unique advantages over conventional materials such as Cu and Al foils, laying the foundation for the development of more efficient and cost-effective electrochemical devices.

- In ***Chapter 3***, the design of a catalyst-substrate integrated electrode using CNT assemblies for hydrogen evolution reaction (HER) in water electrolysis was developed. The goal was to achieve a real industrial application with improved durability. This approach was successfully implemented in a real cell to verify its long-term durability and to realize a completely non-precious metal catalyst-based cell. Such an achievement is expected to make a significant contribution to the field of sustainable hydrogen production.

- ***Chapter 4*** explored the correlation with carbon oxidation reaction (COR) through defect control of CNTs. This effort was aimed at circumventing the limitations of using carbon-based materials due to COR in the oxygen evolution reaction (OER) environment of water electrolysis. Defects mainly affecting COR were identified, and their minimization led to a remarkable improvement in the durability of carbon-based OER catalytic electrodes, thus making progress toward efficient water electrolysis.

## 5.2. Implications of Thesis

The significance of this thesis extends across multiple dimensions, providing important contributions to energy storage and conversion technologies, social impact, and environmental sustainability.

From a scientific perspective, this study provides invaluable insights into the properties and behaviors of CNTs synthesized by the FC-CVD method. By examining their role as alternative current collectors, the research provides comprehensive understanding of their electrochemical properties. Such knowledge has the potential to revolutionize the design and functionality of energy storage devices such as batteries and supercapacitors. In addition, an examination of the relationships between defects in CNTs and carbon corrosion could guide the development of more efficient synthesis techniques to produce high-quality CNTs with optimal properties for specific energy applications.

From an engineering viewpoint, this study advances the industrial application of CNTs. The development and evaluation of substrate-integrated electrodes narrow the gap between laboratory-scale research and industrial implementation. In addition, the study introduces methods to suppress defects and carbon corrosion during the CNT synthesis process, potentially making the FC-CVD method more scalable, reliable, and suitable for industrial production.

On a societal level, the improvements in energy storage and conversion technologies offered by this study could transform many aspects of everyday life. From electronic devices with extended lifetimes to electric vehicles with extended range and lifespan, the benefits are significant. The focus on scalable, low-cost production aligns with global efforts to democratize access to advanced technologies, contributing to energy equity and inclusion.

From an environmental perspective, the research supports sustainability initiatives by improving the viability and efficiency of renewable energy systems and reducing dependence on fossil fuels. The development of more sustainable synthesis methods for high-quality CNTs could reduce the environmental impact of their production. Furthermore, the optimization of energy storage and conversion could significantly reduce energy waste and promote more sustainable energy management and conservation practices.

In conclusion, this study successfully demonstrates the significant potential and versatility of FC-CVD-synthesized CNT assemblies in energy storage and conversion applications. It has broken new ground by overcoming the technical and material challenges that have hindered the widespread adoption of CNTs. This work not only improves the performance and efficiency of existing technologies, but also lays the groundwork for the development of next-generation energy devices. By exploiting the unique properties of CNTs, this study makes a significant contribution to the field of energy science and positions this study as a catalyst for accelerating the development and commercialization of carbon-based energy storage and conversion technologies. Furthermore, the practical, industrial applications of these nanomaterials catalyzed by this study pave the way for the development of next-generation energy systems that are more efficient, reliable, and sustainable. Thus, the potential benefits of CNTs extend beyond the realms of science and engineering to societal progress and environmental stewardship. This study serves as an important milestone in CNT research and marks a critical step toward a more sustainable, energy-efficient future.

# References


[1] P. Zhu et al., "A review of current collectors for lithium-ion batteries", *J. Power Sources* **2021**, *485*, 229321.

[2] A. Abdisattar et al., "Recent advances and challenges of current collectors for supercapacitors", *Electrochem. Commun.* **2022**, *142*, 107373.

[3] T. Ma et al., "Revisiting the Corrosion of the Aluminum Current Collector in Lithium-Ion Batteries", *J. Phys. Chem. Lett.* **2017**, *8(5)*, 1072-1077.

[4] A. Gabryelczyk et al., "Corrosion of aluminium current collector in lithium-ion batteries: A review", *J. Energy Storage* **2021**, *43*, 103226.

[5] Y. Liu et al., "Research Progress on Copper-Based Current Collector for Lithium Metal Batteries", *Energy Fuels* **2021**, *35(16)*, 12921-12937.

[6] H. Cha et al., "Issues and Challenges Facing Flexible Lithium-Ion Batteries for Practical Application", *Small* **2018**, *14(43)*, 1702989.

[7] L. Chen et al., "Lithiophilic and Anticorrosive Cu Current Collector via Dual-Bonded Porous Polymer Coating for Stable Lithium-Metal Batteries", *ACS Appl. Mater. Interfaces* **2023**, *15(7)*, 10273-10282.

[8] Z. Wen et al., "Anticorrosive Copper Current Collector Passivated by Self-Assembled Porous Membrane for Highly Stable Lithium Metal Batteries", *Adv. Funct. Mater.* **2021**, *31(42)*, 2104930.

[9] J.-P. Chen et al., "Flexible and transparent planar supercapacitor based on embedded metallic mesh current collector", *J. Phys. D: Appl. Phys.* **2020**, *53*, 165501.

[10] Z. Ren et al., "Porous Cu Film Enables Thick Slurry-Cast Anodes with Enhanced Charge Transfer Efficiency for High-Performance Li-Ion Batteries", *ACS Appl. Mater. Interfaces* **2020**, *12(42)*, 47623-47633.

[11] H. Jeong et al., "A review on current collector coating methods for next-generation batteries", *Chem. Eng. J.* **2022**, *446(1)*, 136860.

[12] E. Josef et al., "Electrospun Carbon Fibers Replace Metals as a Current Collector in Supercapacitors", *ACS Appl. Energy Mater.* **2019**, *2(8)*, 5724-5733.

[13] G. Zhang et al., "Radially Aligned Porous Carbon Nanotube Arrays on Carbon Fibers: A Hierarchical 3D Carbon Nanostructure for High-Performance Capacitive Energy Storage", *Adv. Funct. Mater.* **2016**, *26(18)*, 3012-3020.

[14] Y. Li et al., "Artificial Graphite Paper as a Corrosion-Resistant Current Collector for Long-Life Lithium Metal Batteries", *Adv. Funct. Mater.* **2023**, *33(19)*, 2214523.

[15] K. Wang et al., "Super-Aligned Carbon Nanotube Films as Current Collectors for Lightweight and Flexible Lithium Ion Batteries", *Adv. Funct. Mater.* **2013**, *23(7)*, 846-853.

[16] T. Zhang et al., "Design Strategies of 3D Carbon-Based Electrodes for Charge/Ion Transport in Lithium Ion Battery and Sodium Ion Battery", *Adv. Funct. Mater.* **2021**, *31(17)*, 2010041.

[17] Q. Wei et al., "Preparation and mechanical properties of composite diamond-like carbon thin films", *J. Vac. Sci. Technol. A*, **1999**, *17*, 3406-3414.

[18] L. Huang et al., "A porous diamond carbon framework: a new carbon allotrope with extremely high gas adsorption and mechanical properties", *J. Mater. Chem. A*, **2013**, *1(12)*, 3851-3855.

[19] P. G. Klemens et al., "Thermal conductivity of graphite in the basal plane", *Carbon* **1994**, *32(4)*, 735-741.

[20] M. Noel et al., "Electrochemistry of graphite intercalation compounds", *J. Power Sources* **1998**, *72(1)*, 53-65.

[21] M. Pumera, "The electrochemistry of carbon nanotubes: fundamentals and applications", *Chem. Eur. J.* **2009**, *15(20)*, 4970-4978.

[22] I. Dumitrescu et al., "Electrochemistry at carbon nanotubes: perspective and issues", *Chem. Commun.* **2009**, 6886-6901.

[23] G. Sun et al., "Electrochemical capacitive properties of CNT fibers spun from vertically aligned CNT arrays", *J. Solid. State Electrochem.* **2012**, *16*, 1775-1780.

[24] J. H. Kim et al., "Fabrication and electrochemical properties of carbon nanotube film electrodes", *Carbon* **2006**, *44(10)*, 1963-1968.

[25] Y. Wang et al., "Realizing high reversible capacity: 3D intertwined CNTs inherently conductive network for CuS as an anode for lithium ion batteries", *Chem. Eng. J.* **2018**, *332*, 49-56.

[26] J. Zhong et al., "Carbon nanotube sponges as conductive networks for supercapacitor devices", *Nano Energy* **2013**, *2(5)*, 1025-1030.

[27] M. Zhang et al., "Ru-$RuO_2$/CNT hybrids as high-activity pH-universal electrocatalysts for water splitting within 0.73 V in an asymmetric-electrolyte electrolyzer", *Nano Energy* **2019**, *61*, 576-583.

[28] H. B. Jung et al., "ZIF-67 metal-organic frameworks synthesized onto CNT supports for oxygen evolution reaction in alkaline water electrolysis", *Electrochim. Acta* **2023**, *439*, 141593.

[29] X. Zhang et al., "Nanostructured energy materials for electrochemical energy conversion and storage: a review", *J. Energy Chem.* **2016**, *25(6)*, 967-984.

[30] Y. Yang et al., "Hierarchically Designed Three-Dimensional Macro/Mesoporous Carbon Frameworks for Advanced Electrochemical Capacitance Storage", *Chem. Eur. J.* **2015**, *21(16)*, 6157-6164.

[31] S. Iijima, "Helical microtubules of graphitic carbon", *Nature* **1991**, *354*, 56-58.

[32] Y. Ando et al., "Preparation of carbon nanotubes by arc-discharge evaporation", *Jpn. J. Appl. Phys.* **1993**, *32*, 107-109.

[33] T. Guo et al., "Catalytic growth of single-walled manotubes by laser vaporization", *Chem. Phys. Lett.* **1995**, *243*, 49-54.

[34] M. Yudasaka et al., "Single-wall carbon nanotube formation by laser ablation using double-targets of carbon and metal", *Chem. Phys. Lett.* **1997**, *278*, 102-106.

[35] M. L. Terranova et al., "The World of Carbon Nanotubes: An Overview of CVD Growth Methodologies", *Chem. Vap. Deposition* **2006**, *12*, 315-325.

[36] M. P. Siegal et al., "Precise control of multiwall carbon nanotube diameters using thermal chemical vapor deposition", *Appl. Phys. Lett.* **2002**, *80(12)*, 2171-2173.

[37] M. Su et al., "A scalable CVD method for the synthesis of single-walled carbon nanotubes with high catalyst productivity", *Chem. Phys. Lett.* **2000**, *322(5)*, 321-326.

[38] A. Kaniyoor et al., "High throughput production of single-wall carbon nanotube fibres independent of sulfur-source", *Nanoscale* **2019**, *11*, 18483-18495

[39] Y. L. Li et al., "Direct spinning of carbon nanotube fibers from chemical vapor deposition synthesis", *Science* **2004**, *304(5668)*, 276-278.

[40] G. S. B. McKee et al., "Dimensional control of multi-walled carbon nanotubes in floating-catalyst CVD synthesis", *Carbon* **2009**, *47(8)*, 2085-2094.

[41] T. Kinoshita et al., "Two step floating catalyst chemical vapor deposition including in situ fabrication of catalyst nanoparticles and carbon nanotube forest growth with low impurity level", *Carbon* **2019**, *144*, 152-160.

[42] A. Vlandas et al., "Enzyme-free sugar sensing in microfluidic channels with an affinity-based single-wall carbon nanotube sensor", *Anal. Chem.* **2010**, *82(14)*, 6090-6097.

[43] Z. Wu et al., "Carbon-nanomaterial-based flexible batteries for wearable electronics", *Adv. Mater.* **2019**, *31(9)*, 1800716.

[44] C. Lamiel et al., "Properties, functions, and challenges: current collectors", *Mater. Today Chem.* **2022**, *26*, 101152.

[45] S. W. Kim et al., "Current collectors for flexible lithium ion batteries: A review of materials", *J. Electrochem. Sci. Technol.* **2015**, *6(1)*, 1-6.

[46] Y. Wang et al., "Electrical Conductivity of Carbon Nanotube- and Graphene-Based Nanocomposites", *Micromechanics and Nanomechanics of Composite Solids* **2017**, 123-156.

[47] K. Kato et al., "Revealing anion chemistry above 3V in Li-ion capacitors", *Electrochim. Acta* **2019**, *324*, 134871.

[48] R. Shi et al., "Electrospun N-Doped Hierarchical Porous Carbon Nanofiber with Improved Degree of Graphitization for High-Performance Lithium Ion Capacitor", *Chem. - Eur. J.* **2018**, *24(41)*, 10460-10467.

[49] N. Mojoudi et al., "Phenol adsorption on high microporous activated carbons prepared from oily sludge: equilibrium, kinetic and thermodynamic studies", *Sci. Rep.* **2019**, *9(1)*, 19352.

[50] L. K. Shrestha et al., "Nanoporous carbon materials with enhanced supercapacitance performance and non-aromatic chemical sensing with $C_1/C_2$ alcohol discrimination", *Sci. Technol. Adv. Mater.* **2016**, *17(1)*, 483-492.

[51] Y. He et al., "Capacitive mechanism of oxygen functional groups on carbon surface in supercapacitors", *Electrochim. Acta* **2018**, *282*, 618-625.

[52] Y. Liang et al., "The role of mass transport pathway in wormholelike mesoporous carbon for supercapacitors", *Phys. Chem. Chem. Phys.* **2010**, *12(36)*, 10842-10845.

[53] B. Xing et al., "Preparation of synthetic graphite from bituminous coal as anode materials for high performance lithium-ion batteries", *Fuel Process. Technol.* **2018**, *172*, 162-171.

[54] H. Shan et al., "Tailored lithium storage performance of graphene aerogel anodes with controlled surface defects for lithium-ion batteries", *Appl. Surf. Sci.* **2016**, *364*, 651-659.

[55] X.-L. Wu et al., "Carbon-Nanotube-Decorated Nano-$LiFePO_4$@C Cathode Material with Superior High-Rate and Low-Temperature Performances for Lithium-Ion Batteries", *Adv. Energy Mater.* **2013**, *3(9)*, 1155-1160.

[56] Y.-W. Lee et al., "In situ synthesis and characterization of Ge embedded electrospun carbon nanostructures as high performance anode material for lithium-ion batteries", *ACS Appl. Mater. Interfaces* **2016**, *8(11)*, 7022-7029.

[57] M. Liang et al., "Ru- and Cl-Codoped $Li_3V_2(PO_4)_3$ with Enhanced Performance for Lithium-Ion Batteries in a Wide Temperature Range", *Small* **2022**, *18(29)*, 2202151.

[58] H.-J. Peng et al., "3D carbonaceous current collectors: The origin of enhanced cycling stability for high-sulfur-loading lithium–sulfur batteries", *Adv. Funct. Mater.* **2016**, *26(35)*, 6351-6358.

[59] R. Wang et al., "Carbon black/graphene-modified aluminum foil cathode

current collectors for lithium ion batteries with enhanced electrochemical performances", *J. Electroanal. Chem.* **2019**, *833*, 63-69.

[60] Z. Zhou et al., "Ultra-Lightweight 3D Carbon Current Collectors: Constructing All-Carbon Electrodes for Stable and High Energy Density Dual-Ion Batteries", *Adv. Energy Mater.* **2018**, *8*, 1801439.

[61] J. Lu, "Effect of surface modifications on the decoration of multi-walled carbon nanotubes with ruthenium nanoparticles", *Carbon* **2007**, *45(8)*, 1599-1605.

[62] F. Li et al., "Mechanochemically assisted synthesis of a Ru catalyst for hydrogen evolution with performance superior to Pt in both acidic and alkaline media", *Adv. Mater.* **2018**, *30*, 1803676.

[63] H. Ago et al., "Work functions and surface functional groups of multiwall carbon nanotubes", *J. Phys. Chem. B* **1999**, *103(38)*, 8116-8121.

[64] Y.-C. Chiang et al., "The influence of treatment duration on multi-walled carbon nanotubes functionalized by $H_2SO_4/HNO_3$ oxidation", *Appl. Surf. Sci.* **2011**, *257(6)*, 2401-2410.

[65] J. Zhang et al., "Effect of chemical oxidation on the structure of single-walled carbon nanotubes", *J. Phys. Chem. B* **2003**, *107(16)*, 3712-3718.

[66] Q. Zhang et al., "Tunable self-discharge process of carbon nanotube based supercapacitors", *Nano Energy* **2014**, *4*, 14-22.

[67] D. J. Morgan, "Resolving ruthenium: XPS studies of common ruthenium materials", *Surf. Interface Anal.* **2015**, *47(11)*, 1072-1079.

[68] B. Lu et al., "Ruthenium atomically dispersed in carbon outperforms platinum toward hydrogen evolution in alkaline media", *Nat. Commun.* **2019**, *10(1)*, 631.

[69] S. Cattaneo et al., "Ru supported on micro and mesoporous carbons as catalysts for biomass-derived molecules hydrogenation", *Catal. Today* **2020**, *357*, 143-151.

[70] N. Chakroune et al., "Acetate-and thiol-capped monodisperse ruthenium nanoparticles: XPS, XAS, and HRTEM studies", *Langmuir* **2005**, *21(15)*, 6788-6796.

[71] G. Wang et al., "Improving the specific capacitance of carbon nanotubes-based supercapacitors by combining introducing functional groups on carbon nanotubes with using redox-active electrolyte", *Electrochim. Acta* **2014**, *115*, 183-188.

[72] J. Shen et al., "How carboxylic groups improve the performance of single-walled carbon nanotube electrochemical capacitors?", *Energy Environ. Sci.* **2011**, *4(10)*, 4220-4229.

[73] M. Farbod et al., "A three-dimensional Ag nanoparticle/graphene hydrogel composite and its application as an improved supercapacitor's electrode", *J. Solid State Electrochem.* **2019**, *23(11)*, 3009-3017.

[74] J. Zhao et al., "Porous 3D few-layer graphene-like carbon for ultrahigh-power supercapacitors with well-defined structure–performance relationship", *Adv. Mater.* **2017**, *29*, 1604569.

[75] P. Yu et al., "Homogeneous $Fe_2O_3$ coatings on carbon nanotube structures for supercapacitors", *Dalton Trans.* **2020**, *49*, 4136–4145.

[76] S. Iqbal et al., "Ruthenium nanoparticles supported on carbon: an active catalyst for the hydrogenation of lactic acid to 1, 2-propanediol", *ACS Catal.* **2015**, *5(9)*, 5047-5059.

[77] M. K. Cho et al., "Alkaline anion exchange membrane water electrolysis: Effects of electrolyte feed method and electrode binder content", *J. Power Sources* **2018**, *382*, 22-29.

[78] R. Sulaiman et al., "Recent developments on transition metal–based electrocatalysts for application in anion exchange membrane water electrolysis", *Int. J. Energy Res.* **2022**, *46(3)*, 2241-2276.

[79] D. Li et al., "Durability of anion exchange membrane water electrolyzers", *Energy Environ. Sci.* **2021**, *14*, 3393-3419.

[80] J. H. Jang et al., "Emerging carbon shell-encapsulated metal nanocatalysts for fuel cells and water electrolysis", *Nanoscale* **2021**, *13*, 15116-15141.

[81] A. Sivanantham et al., "Hierarchical $NiCo_2S_4$ Nanowire Arrays Supported on Ni Foam: An Efficient and Durable Bifunctional Electrocatalyst for

Oxygen and Hydrogen Evolution Reactions", *Adv. Funct. Mater.* **2016**, *26*, 4661-4672.

[82] W. Yang et al., "Recent progress in electrode fabrication for electrocatalytic hydrogen evolution reaction: A mini review", *Chem. Eng. J.* **2020**, *393*, 124726.

[83] J. Li et al., "$NiCoSe_{2-x}$/N-doped C mushroom-like core/shell nanorods on N-doped carbon fiber for efficiently electrocatalyzed overall water splitting", *Electrochim. Acta* **2018**, *272*, 161-168.

[84] M. Guo et al., "Amine-assisted synthesis of the $Ni_3Fe$ alloy encapsulated in nitrogen-doped carbon for high-performance water splitting", *J. Mater. Chem. A* **2023**, *11(12)*, 6452-6464.

[85] I. A. Poimenidis et al., "Electrodeposited Ni foam electrodes for increased hydrogen production in alkaline electrolysis", *Fuel* **2023**, *342*, 127798.

[86] K. Karthick et al., "Advancing the extended roles of 3D transition metal based heterostructures with copious active sites for electrocatalytic water splitting", *Dalton Trans.* **2021**, *50*, 13176-13200.

[87] W. Wu et al., "Encapsulating Pt Nanoparticles inside a Derived Two-Dimensional Metal–Organic Frameworks for the Enhancement of Catalytic Activity", *ACS Appl. Mater. Interfaces* **2020**, *12(9)*, 10359-10368.

[88] W. He et al., "Modulating the Electronic Structure of Nickel Sulfide Electrocatalysts by Chlorine Doping toward Highly Efficient Alkaline Hydrogen Evolution", *ACS Appl. Mater. Interfaces* **2022**, *14(5)*, 6869-6875.

[89] J. H. Jun et al., "Intertwined CNT Assemblies as an All-Around Current Collector for Volume-Efficient Lithium-Ion Hybrid Capacitor", *ACS Appl. Mater. Interfaces* **2023**, *15(21)*, 25484-25494.

[90] J. Yang et al., "Electrochemical performances investigation of NiS/rGO composite as electrode material for supercapacitors", *Nano Energy* **2014**, *5*, 74-81.

[91] K. S. Dijith et al., "Polyol derived Ni and NiFe alloys for effective shielding of electromagnetic interference", *Mater. Chem. Front.* **2018**, *2*, 1829-1841.

[92] B. Fei et al., "Ultrathinning nickel sulfide with modulated electron density for efficient water splitting", *Adv. Energy Mater.* **2020**, *10(41)*, 2001963.

[93] X. Liu et al., "The synergistic effect of light irradiation and interface engineering of the $Co(OH)_2/MoS_2$ heterostructure to realize the efficient alkaline hydrogen evolution reaction", *Electrochim. Acta* **2019**, *299*, 618-625.

[94] B. Zhang et al., "Interface engineering: the $Ni(OH)_2/MoS_2$ heterostructure for highly efficient alkaline hydrogen evolution", *Nano Energy* **2017**, *37*,

74-80.

[95] L. Hu et al., “p–d hybridization in CoFe LDH nanoflowers for efficient oxygen evolution electrocatalysis”, *Inorg. Chem. Front.* **2022**, *9*, 5296-5304.

[96] A. Wang et al., “Tuning the oxygen evolution reaction on a nickel–iron alloy via active straining”, *Nanoscale*, **2019**, *11*, 426-430.

[97] J. Wang et al., “Manipulating the Water Dissociation Electrocatalytic Sites of Bimetallic Nickel-Based Alloys for Highly Efficient Alkaline Hydrogen Evolution”, *Angew. Chem.* **2022**, *61*, e202202518.

[98] Z. W. Seh et al., “Combining theory and experiment in electrocatalysis: Insights into materials design”, *Science* **2017**, *355*, 146.

[99] Z. Sun et al., “Anion-Exchange Membranes for Alkaline Fuel-Cell Applications: The Effects of Cations”, *ChemSusChem* **2018**, *11(1)*, 58-70.

[100] M. J. Jang et al., “Superior performance and stability of anion exchange membrane water electrolysis: pH-controlled copper cobalt oxide nanoparticles for the oxygen evolution reaction”, *J. Mater. Chem. A* **2020**, *8*, 4290-4299.

[101] S. J. Ashton et al., “A DEMS study on the electrochemical oxidation of a high surface area carbon black”, *Electrochem. Commun.* **2011**, *13(12)*, 1473-1475.

[102] S. Möller et al., “Online Monitoring of Electrochemical Carbon Corrosion in Alkaline Electrolytes by Differential Electrochemical Mass Spectrometry”, *Angew. Chem.* **2020**, *59(4)*, 1585-1589.

[103] S. Maass et al., “Carbon support oxidation in PEM fuel cell cathodes”, *J. Power Sources* **2008**, *176(2)*, 444-451.

[104] P. Kanninen et al., “Carbon corrosion properties and performance of multi-walled carbon nanotube support with and without nitrogen-functionalization in fuel cell electrodes”, *Electrochim. Acta* **2020**, *332*, 135384.

[105] N. Macauley et al., “Carbon Corrosion in PEM Fuel Cells and the Development of Accelerated Stress Tests”, *J. Electrochem. Soc.* **2018**, *165(6)*, F3148.

[106] Y. Chen et al., “Graphitic carbon nitride-based electrocatalysts for energy applications”, *Mater. Today Catal.* **2023**, *1*, 100003.

[107] H. Chen et al., "Rational control on floating catalysts for the growth of carbon nanotube assemblies: From vertically aligned carbon nanotube arrays to carbon nanotube films", *Appl. Surf. Sci.* **2015**, *353*, 651-661.

[108] S. Shukrullah et al., "Study of surface defects and crystallinity of MWCNTs growth in FCCVD", *Sci. Eng. Compos. Mater.* **2017**, *24(6)*, 845-851.

[109] S. Y. Moon et al., "High-crystallinity single-walled carbon nanotube aerogel growth: Understanding the real-time catalytic decomposition reaction through floating catalyst chemical vapor deposition", *Chem. Eng. J. Adv.* **2022**, *10*, 100261.

[110] J. H. Park et al., "Continuous synthesis of high-crystalline carbon nanotubes by controlling the configuration of the injection part in the floating catalyst chemical vapor deposition process", *Carbon Lett.* **2020**, *30*, 613-619.

[111] M. D. Yadav et al., "Kinetic study of multi-walled carbon nanotube synthesis by thermocatalytic decomposition of methane using floating catalyst chemical vapour deposition", *Chem. Eng. J.* **2019**, *377*, 119895.

[112] Y. Shirazi et al., "Effects of different carbon precursors on synthesis of multiwall carbon nanotubes: Purification and Functionalization", *Appl. Surf. Sci.* **2011**, *257(16)*, 7359-7367.

[113] X. Xie et al., "Oxygen Evolution Reaction in Alkaline Environment: Material Challenges and Solutions", *Adv. Funct. Mater.* **2022**, *32(21)*, 2110036.

[114] W. Wang et al., "Carbon oxidation reactions could misguide the evaluation of carbon black-based oxygen-evolution electrocatalysts", *Chem. Commun.* **2017**, *53*, 11556-11559.

[115] F. Y. Chen et al., "Stability challenges of electrocatalytic oxygen evolution

reaction: From mechanistic understanding to reactor design", *Joule* **2021**, *5(7)*, 1704-1731.

[116] Y. Yi et al., "Electrochemical Degradation of Multiwall Carbon Nanotubes at High Anodic Potential for Oxygen Evolution in Acidic Media", *ChemElectroChem* **2015**, *2(12)*, 1929-1937.

[117] F. Forouzandeh et al., "Understanding the Corrosion Resistance of Meso- and Micro-Porous Carbons for Application in PEM Fuel Cells", *J. Electrochem. Soc.* **2018**, *165(6)*, F3230.

[118] Y. Qi et al., "Insight into carbon corrosion of different carbon supports for Pt-based electrocatalysts using accelerated stress tests in polymer electrolyte fuel cells", *J. Power Sources* **2022**, *551*, 232209.

[119] C. Peng et al., "Effect of the carbon on the electrochemical performance of rechargeable Zn-air batteries", *Int. J. Hydrogen Energy* **2023**, *48(13)*, 5313-5322.

[120] K. Li et al., "Classification and carbon structural transformation from anthracite to natural coaly graphite by XRD, Raman spectroscopy, and HRTEM", *Spectrochim. Acta A Mol. Biomol. Spectrosc.* **2021**, *249*, 119286.

[121] X. Liu et al., "Study on the evolution of the char structure during hydrogasification process using Raman spectroscopy", *Fuel* **2015**, *157*, 97-106.

[122] Y. Ma et al., “Control of product nature and morphology by adjusting the hydrogen content in a continuous chemical vapor deposition process for carbon nanotube synthesis”, *Carbon* **2016**, *107*, 171-179.

[123] Y. Jung et al., "Controlling the crystalline quality of carbon nanotubes with processing parameters from chemical vapor deposition synthesis", *Chem. Eng. J.* **2013**, *228*, 1050-1056.

[124] I. N. Izzaiti et al., "Effect of Carbon Source Injection Rate on CNT Film via Floating Catalyst CVD Method", *Solid State Phenom.* **2019**, *290*, 113-121.

[125] J.-H. Lee et al., “Designing thermal and electrochemical oxidation processes for δ-$MnO_2$ nanofibers for high-performance electrochemical capacitors”, *J. Mater. Chem. A* **2014**, *2*, 7197-7204.

[126] S. Dong et al., “A Review of the Application of Heterostructure Catalysts in Hydrogen Evolution Reaction”, *ChemistrySelect* **2022**, *7(14)*, e202104041

[127] Z. E. Brubaker et al., “Quantitative analysis of Raman spectral parameters for carbon fibers: practical considerations and connection to mechanical properties”, *J. Mater. Sci.* **2021**, *56*, 15087-15121.

[128] M. Couzi et al., “A multi wavelength Raman scattering study of defective graphitic carbon materials: The first order Raman spectra revisited”, *Carbon* **2016**, *107*, 388-394.

[129] H. Liu, "Evolution of the Hierarchical Molecular Structures of Tectonically Deformed Coals: Insights from First-Order Raman Spectra", *ACS Omega* **2022**, *7(40)*, 35942-35950.

[130] G. A. Zickler et al., “A reconsideration of the relationship between the crystallite size La of carbons determined by X-ray diffraction and Raman spectroscopy”, *Carbon* **2006**, *44(15)*, 3239-3246.

[131] S. A. Chernyak et al., “Mechanism of Thermal Defunctionalization of Oxidized Carbon Nanotubes”, *J. Phys. Chem.* **2016**, *120(31)*, 17465-17474.

[132] M. Wang et al., "Thermal defect healing of single-walled carbon nanotubes assisted by supplying carbon-containing reactants", *Appl. Phys. Express* **2023**, *16*, 015002.

[133] J. A. Vega et al., “Effect of $CO_2$, $HCO_3^-$ and $CO_3^{2-}$ on oxygen reduction in anion exchange membrane fuel cells”, *Electrochim. Acta* **2010**, *55(5)*, 1638-1644.

[134] H. Haspel et al., “Is Hydroxide Just Hydroxide? Unidentical $CO_2$ Hydration Conditions during Hydrogen Evolution and Carbon Dioxide Reduction in Zero-Gap Gas Diffusion Electrode Reactors”, *ACS Appl. Energy Mater.* **2021**, *4(8)*, 8506-8516.

# 요약(국문초록)

본 학위논문에서는 부유촉매 화학기상증착법(FC-CVD)으로 합성한 탄소나노튜브(CNT) 어셈블리의 특징과 잠재력을 바탕으로 에너지 저장 및 변환 시스템의 기존 소재에서 기인하는 문제점들의 해결 가능성을 제시한다. 이러한 가능성은 CNT의 고유한 소재 특성과 FC-CVD를 통해 얻을 수 있는 구조적 이점, 그리고 공정 측면에서의 효율성이 결합되어 에너지 저장 및 변환 분야의 기술 발전에 중대한 변화를 가져올 수 있을 것이라는 전망에서 출발한다. 이를 위해, 소재, 구조, 공정의 세 가지 주요 관점을 통해 CNT 어셈블리의 활용 가능성을 심층적으로 탐구한다.

첫째로, FC-CVD로 제작한 CNT 어셈블리를 배터리 및 슈퍼커패시터 등 에너지 저장 장치의 집전체에 대한 혁신적인 대안으로의 활용 가능성을 증명한다. 이 새로운 어셈블리는 기존의 금속 기반 집전체와 관련된 일반적인 제한 사항을 극복할 뿐만 아니라 더욱 향상된 전기화학적 성능 구현이 가능함을 실험적으로 확인한다. 이는 에너지 저장 시스템의 성능 관련 측면에서 중요한 발전을 의미하며, 에너지 효율성을 더욱 향상시키는 새로운 전망을 제공한다.

둘째로, FC-CVD를 통해 합성된 CNT 어셈블리를 기반으로 촉매와 기판이 일체화된 전극 구조를 설계하고 구현한다. CNT 어셈블리의 독특한

구조적 특성은 수전해 시스템의 수소 발생 반응(HER) 촉매 전극의 성능 및 내구성 향상에 효과적으로 작용하여 효율적이고 지속 가능한 수소 생산 기반 마련에 기여한다. 또한 촉매와 CNT 어셈블리의 성공적인 통합은 비귀금속 기반 촉매의 현존하는 문제를 해결하여 장차 첨단 전극 재료 설계에 획기적인 영향을 제공할 뿐만 아니라, 청정 에너지 기술의 혁신을 촉진할 것으로 예상한다.

마지막으로, 탄소의 결함과 부식 간의 상관 관계를 체계적으로 조사하여 산소 발생 반응(OER) 촉매에 대한 탄소 기반 지지체의 내구성 향상에 대한 통찰을 제공한다. 일반적으로 탄소 기반 재료를 OER 환경에 적용하는 것은 탄소 산화 반응(COR)으로 인해 어려운 것으로 알려져 있다. 따라서 COR이 진행되는 탄소의 결함을 분류하고, 결함 종류에 따른 COR과의 연관관계를 이해하기 위한 분석적 접근을 시도한다. 이에 FC-CVD의 공정 변수 제어를 통해 다양한 유형과 분포의 결함을 가진 CNT를 합성하여, COR 거동 및 경향을 확인하고 이와 명확한 상관관계를 갖는 결함을 식별한다. 또한 이를 최소화하여 탄소 기반 OER 촉매 지지체의 내구성을 극대화할 수 있는 방법을 제시함으로써, 그동안 도전적이었던 탄소계 소재의 응용 한계를 돌파하고 적용 분야 확장에 기여한다.

결론적으로, 본 학위논문은 FC-CVD에서 파생된 CNT 어셈블리가 에너지 저장 및 변환 응용 분야에서 현존하는 소재, 구조, 공정 측면에서의 문제점들을 효과적으로 완화할 수 있는 대안으로의 가능성을 증명한다.

이러한 과정은 기존의 문제점들을 극복하는 청사진을 제공함으로써, 차세대 전기화학 장치의 설계와 최적화에 중요한 역할을 할 것이다. 더불어, 과학, 공학, 사회, 환경에 긍정적인 영향을 미칠 수 있는 중요한 통찰력을 제공하여 다양한 분야에서의 발전을 촉진하는데 기여할 것으로 사료된다.

---

**표제어:** 부유촉매 화학기상증착법, 탄소나노튜브, 에너지 저장, 배터리, 슈퍼커패시터, 에너지 변환, 수전해, 수소 발생 반응, 산소 발생 반응, 탄소 산화 반응.

**학 번:** 2018-35781

# CURRICULUM VITAE

## Jong Han Jun


Bldg. 30 Rm. 525 E-mail: jhjun46@snu.ac.kr

Department of Materials Science and Engineering Tel: +82-2-880-7357

Seoul National University Mobile: +82-10-3801-3760

1 Gwanak-ro, Gwanak-gu, Seoul 08826, Republic of Korea Fax: +82-2-885-9671


### EDUCATION

2018. 09. ~ 2023. 08. ***Ph.D.***

Department of Materials Science and Engineering

Seoul National University, Seoul, Korea

Advisor: Prof. In-Suk Choi

2015. 03 ~ 2017. 08. ***M.S.***

Department of Information Communication, Materials, and Chemistry Convergence Technology

Soongsil University, Seoul, Korea

Advisor: Prof. Youngjin Jeong

2009. 03 ~ 2015. 02. ***B.S.***

Department of Organic Materials and Fiber Engineering

Soongsil University, Seoul, Korea

## RESEARCH AREAS

- **Synthesis of Carbon Nanotubes (CNTs) by Floating Catalyst Chemical Vapor Deposition (FC-CVD)**
  - Control of synthesis process variables to improve mechanical, electrical and electrochemical properties
  - Development of post-synthesis treatment methods to improve the properties of FC-CVD produced CNTs

- **Carbon-Based Electrochemical Storage and Conversion Applications**
  - Design of deformable carbon-based current collectors
  - High efficiency and performance electrode active materials for next-generation lithium-ion batteries and supercapacitors
  - Development of durable HER/OER electrocatalysts and carbon-based substrates

## PUBLICATIONS

- **Jong Han Jun**, Song Jin, Jaehoon Jeong, Youngjin Jeong, Sung Mook Choi, Min Ho Seo, In-Suk Choi*, and Ji-Hoon Lee*, "Hierarchical CNT Sheets Supported Nickel Iron Sulfide as HER Catalyst-Integrated Electrodes for Anion Exchange Membrane Water Electrolysis", *in preparation.*

- Seohyun Park†, **Jong Han Jun**†, Minjeong Park, Jaehoon Jeong, Jeong-Hyang Jo, So-Hee Jeon, Juchan Yang, Sung Mook Choi, Wook Jo*, and Ji-Hoon Lee*, "Hierarchically Designed $Co_4Fe_3$@N-doped Graphitic Carbon as a Highly-active Oxygen Evolution

Reaction Electrocatalysts for Anion Exchange Membrane Water Electrolysis", *in preparation.*

- Tae-Hwan Huh, **Jong Han Jun**, Sun Woong Mun, Byung Hyo Kim*, and Young-Je Kwark*, "Fabrication of hierarchically porous SiCN/Ni nanocomposite using branch structured polysilazane as hydrogen evolution reaction catalyst", *in preparation.*

- **Jong Han Jun**, Jeongin Paeng, Juhee Kim, Jungho Shin, In-Suk Choi*, and Ji-Hoon Lee*, "Intertwined CNT Assemblies as an All-Around Current Collector for Volume-Efficient Lithium-Ion Hybrid Capacitors", *ACS Applied Materials & Interfaces* **2023**, *15(21)*, 25484-25494. (Selected as supplementary cover)

- **Jong Han Jun**, Yu-Ki Lee, Juhee Kim, Hyeonjun Song, Youngjin Jeong, Changsoon Kim, Ji-Hoon Lee*, and In-Suk Choi*, "Large-Scale, Lightweight, and Robust Nanocomposites Based on Ruthenium-Decorated Carbon Nanosheets for Deformable Electrochemical Capacitors", *ACS Applied Materials & Interfaces* **2022**, *14(10)*, 12193-12203.

- **Jong Han Jun**, Hyeonjun Song, and Youngjin Jeong*, "Ultra-Lightweight and Flexible Current Collector Based on Freestanding Carbon Nanotube Sheets for Lithium-Ion Capacitors", *Advanced Materials Technologies* **2019**, *4(2)*, 1800452.

- **Jong Han Jun**, Hyeonjun Song, Changsoon Kim, In-Suk Choi*, Youngjin Jeong*, and Ji-Hoon Lee*, "Carbon-Nanosheet Based Large-Area Electrochemical Capacitor that is Flexible, Foldable, Twistable, and Stretchable", *Small* **2018**, *14(43)*, 1702145. (Selected as frontispiece)

## PRESENTATIONS AT INTERNATIONAL CONFERENCES

- **Jong Han Jun***, Hyeonjun Song, Changsoon Kim, Youngjin Jeong, Ji-Hoon Lee, and In-Suk Choi, "Hybrid Carbon-Nanosheets with Hierarchical Structure for Shape Deformable Electrochemical Capacitors", NANO KOREA 2019, Goyang, Republic of Korea.

- **Jong Han Jun***, Hyeonjun Song, Changsoon Kim, In-Suk Choi, Youngjin Jeong, and Ji-Hoon Lee, "Hierarchically Structured Large Area Carbon-Nanosheets for Shape Deformable Electrochemical Capacitors", 2018 MRS Fall Meeting & Exhibit, Boston, USA.

## PATENTS

- Ji-Hoon Lee, Sung Mook Choi, Juchan Yang, Jaehoon Jeong, Sohee Jeon, Minjeong Park, Seohyun Park, **Jong Han Jun**, Jeonghyang Jo, "Fabrication method of electrode using photonic sintering and electrode made therefrom", Korea patent 10-2022-0189112

- Sung Mook Choi, Sin Woo Myeong, Juchan Yang, Ji-Hoon Lee, **Jong Han Jun**, Jaehoon Jeong, Chaeyeon Kwon, Jaeyeop Jeong, "Method for manufacturing electrode for water electrolysis and electrode for water electrolysis therefrom", Korea patent 10-2022-0032259

## AWARDS AND HONORS

| | |
|---|---|
| 2021 ~ 2022 | **The 19th Research Scholarship Program**<br>Hyundai Motor Company, Republic of Korea |
| 2018 | **Lecture & Research Scholarship**<br>Seoul National University, Republic of Korea |

## R&D PROJECTS

- "Development of technology for durable electrode with controlled morphology·structure to minimize degradation of C2S performance", National Research Foundation of Korea, 2022. 04. ~ 2023. 02.

- "Development of high-performance catalytic electrodes and parts technology on 2.5kW-class AEM water electrolysis using waste-alkali solution for hydrogen production", Korea Evaluation Institute of Industrial Technology (KEIT), 2022. 04. ~ 2022. 12.

- "Development of supercritical environmental electrochemical water oxidation catalysts and electrodes", National Research Council of Science & Technology (NST), 2022. 03. ~ 2023. 08.

- "Development of 200kW-scale AEM(Anion Exchange Membrane) Electrolyser System for Green Hydrogen Market Deployment", Korea Energy Technology

Evaluation and Planning (KETEP), 2021. 11. ~ 2023. 08.

- “Development of durable electrode and evaluation for anion exchange membrane water electrolysis for production of green hydrogen”, National Research Council of Science & Technology (NST), 2021. 09. ~ 2023. 08.

- “A Research on Green Hydrogen Production Based on Anion Exchange Membrane (AEM) Water Electrolyser Utilizing Waste Nutrient Solution”, Rural Development Administration, 2021. 09. ~ 2023. 08.

- “Development and standardization of novel measurement and analysis for flexible battery materials in multiplex environment”, National Research Foundation of Korea, 2021. 07. ~ 2021. 08.

- “Design and Realization of Morphic Structure by Computational Algorithm”, National Research Foundation of Korea, 2019. 03. ~ 2021. 08.

- “Development of flexible display for monolithic generation of sound and color based on photonic nano-crystal”, National Research Foundation of Korea, 2018. 12. ~ 2021. 08.

- “Towards revamped materials through structural transformation: Design and application of multi-variant structure”, the Creative-Pioneering Researchers Program through Seoul National University, 2018. 09. ~ 2021. 08.

- “Center for SoFT meta-Human”, Engineering Research Center (ERC) Program funded by National Research Foundation of Korea, 2018. 09. ~ 2021. 08.

- “Breathable 4-D skin sensors for long-term monitoring of multimodal bio-signals”, Samsung Electronics, 2018. 09. ~ 2021. 03.

- “Innovative Process Design Center for Strategic Structural Materials”, Engineering Research Center (ERC) Program funded by National Research Foundation of Korea, 2018. 09. ~ 2020. 02.

# 감사의 글

2014년 여름부터 2023년 여름까지 학부연구생과 석사과정, 그리고 박사과정을 거쳐 학위를 취득하기까지 만 9년의 시간이 흘렀습니다. 박사학위 논문이 완성될 수 있었던 건 오직 혼자만의 노력으로 이루어진 결실이 결코 아니기에 그동안 도움을 주셨던 많은 분들께 감사의 말씀을 드리고자 합니다.

우선 오랜 기간 동안 학문적, 인격적으로 깊이 있는 가르침을 주시고 한 사람의 독립된 연구자로서 넓은 시야와 능력을 갖도록 물심양면으로 많은 지도를 해주신 최인석 교수님께 깊은 감사를 드립니다. 제가 연구자의 길을 걸을 수 있도록 해주심은 물론 지금까지도 좋은 연구 성과를 낼 수 있도록 적극 도와주고 계신 정영진 교수님께도 다시 한 번 감사드립니다. 그리고 석사 첫 학기부터 박사 졸업을 앞둔 현재까지도 함께 해주시며 어려웠던 매 순간마다 조언과 위로를 아낌없이 주신 이지훈 박사님께 진심으로 감사드립니다. 여러모로 부족했던 제가 세 분을 만나 이 자리에 오게 된 것이 저에게는 매우 큰 행운이라 생각합니다. 그동안 주신 가르침과 열정, 헌신, 그리고 존경심을 절대 잊지 않고 살아가는 제자가 되겠습니다. 아울러 바쁜 일정 중에도 학위 심사위원으로 참석하셔서 아낌없는 조언을 주신 강기석 교수님과 박종래 교수님께 감사드립니다. 에너지 분야와 탄소재료 분야의 대가를 모셔서 심사를 받고 더욱 탄탄한 박사학위논문을 완성하게 되어 매우 영광스럽게 생각합니다. 앞으로도 제가 전공한 분야의 발전에 기여하는 연구자의 일원으로 성장해 나가겠습니다.

두려움과 걱정으로 가득했던 대학원 생활을 시작하던 무렵 만나 지금은 각자의 분야에서 열심히 살아가고 있는 형남공학관 722호 동료, 친구, 선후배분들 정말 고맙습니다. 직장 생활에 바쁜 와중에도 만날 때면 늘 편안하고 즐거움을 주는 여러분들 덕분에 저도 잘 버틸 수 있었습니다. 긴 시간 동안 언제나 힘이 되고 격려해주던 현준이와 희정이, 박사과정 기간을 함께 보내며 서로 많이 의지할 수 있었던 태환이형과 소연 부부, 그리고 연구실 생활에 잘 적응할 수 있도록 세심하게 챙겨주던 세현누나에게 감사합니다.

2018년 MVSM LAB의 출발을 함께하며 녹록치 않았던 새로운 실험실 셋업과 다방면의 도움을 준 유기, 주희를 비롯해 바쁜 연구실 생활 중에도 귀찮은 부탁 묵묵히 잘 들어준 정인이, 그리고 각자 연구에 임하면서도 방장인 저를 잘 따라준 영채, 은솔, 재영, 가은, 제웅, 혜인, 규호 외 연구실 후배들에게도 고마운 말 전하고 싶습니다. 마지막 2년 동안 함께했던 KIMS 그린수소재료연구실 실원분들께도 감사드립니다. 다소 생소했던 수전해라는 연구분야에 흥미를 느끼고 연구 성과 창출을 위해 다방면으로 많은 지원을 해주신 최승목 박사님, 양주찬 박사님, 정재훈 연구원님께 감사드립니다. 박사학위 심사를 준비하느라 매일 새벽 늦게까지 연구실에 머무를 때 저와 함께하며 의지가 되어주신 김치호 박사님, 박민정 박사님, 윤기용 박사님 감사합니다. 아울러 선배로써 신경을 많이 써줬어야 함에도 불구하고 바쁘다는 이유로 오히려 저에게 많은 도움을 주었던 실 학생들 모두에게도 진심으로 고맙습니다.

마지막으로, 제가 하는 선택에 대해 항상 조건 없이 지원해주시고 누구보다도 적극적으로 응원해주시는 아버지와 어머니가 계셨기에 모든

것들이 가능했고 이 자리에 올 수 있었습니다. 저를 자랑스럽게 생각하시는 부모님께 받은 귀중한 사랑과 감사함을 절대 잊지 않고 평생 보답하고 효도하며 누구에게나 부끄럽지 않은 아들이 되겠습니다. 그리고 오빠로서 챙겨 주는 것이 늘 부족하다고 느낌에도 어디에서나 걱정 없이 야무지게 제 역할 잘하는 동생 지원이게도 정말 고맙습니다.

박사학위를 받는다는 것은 어느 여정의 마지막이 아닌 새로운 시작의 순간에 왔음을 의미하는 것 같습니다. 여정을 함께하며 수많은 도움을 주신 여러분들께 다시 한 번 진심으로 감사드리며, 앞으로도 제가 가는 어디에서나 발전과 노력을 게을리 하지 않는 한 사람의 연구자, 사회인, 그리고 아들과 오빠의 역할을 다할 수 있도록 노력하겠습니다.

2023년 8월

전 종 한 드림